Modelling the behavior of dapped-end connections with fiber-reinforced concrete

Auteur : Berger, Paul-Hadrien
Promoteur(s) : Mihaylov, Boyan
Faculté : Faculté des Sciences appliquées
Diplôme : Master en ingénieur civil des constructions, à finalité spécialisée en "civil engineering"
Année académique : 2020-2021
URI/URL : http://hdl.handle.net/2268.2/11387

UNIVERSITÉ DE LIÈGE

Modelling the behavior of dapped-end connections with fiber-reinforced concrete

Master's thesis submitted in fulfillment of the requirements for the Master Degree in Civil Engineering by Paul-Hadrien Berger

Jury members :
Boyan Mihaylov
Jean-François Demonceau
Luc Courard
Renaud Franssen

Promotor :
Boyan Mihaylov

ULiège : 2020-2021

Acknowledgements

First of all, I would like to fully thank my promotor Professor Mihaylov and his PhD student Chathura Rajapakse for mentoring me throughout this thesis. I had the chance to meet them regularly and discuss the progress of my work. It was a pleasure to discover the field of research and to share my discoveries and research with them.

I would also like to thank the members of the Jury that I had the opportunity to meet during my work to share with them my discoveries and the structure of my work. I thank them for their interest in the subject of my Master's Thesis and for taking time to read this study.

I thank my classmate Louis Groulard who did a Master's Thesis on fiber-reinforced polymer dapped-end connections. After spending five years together, we had the pleasure to share our last academic work, both supervised by Professor Mihaylov. We worked together several times and compared the two methods of dapped-end connections reinforcement (FRC and FRP).

A huge thank you also goes to all those who participated in the implementation of this work, especially to all the authors of the bibliographic sources without whom the results could not have been so promising.

Abstract

This Master's Thesis is aimed at modelling the behavior of fiber-reinforced concrete (FRC) dapped-end connections. These connections are subjected to high stress concentrations due to their abrupt change of cross-section and it usually leads to sudden collapse. The use of FRC increases the ductility of the material and allows to prevent the rupture. The kinematic model takes into account the serviceability of the dapped-end and is not only a tool for design at ultimate limit state. In reality, this method assesses the structural state of the dapped-end by collecting data in situ.

The studied model applies to one failure mode, a flexural failure governed by an inclined crack starting from the re-entrant corner. This mode of failure is the most frequent for experimental structures and more frequent when the amount of fibers added in the concrete is high. The model compares its predictions to experimental data collecting from different scientific papers. These data have been analyzed on the most accurate way as possible to confirm the validity of the results.

At first, the kinematic model is developed by a simplified approach to predict the peak capacity of a dapped-end. Globally, this approach is quite similar to the one developed by Rajapakse et al. applied to reinforced-concrete structures. The predicted results with FRC compared to the experimental results are promising.

Then, the complete behavior of the dapped-end connections is modelled. This approach aims at not only reaching the real peak capacity but also at modelling the main inclined crack for any loading condition. Some parameters have been calibrated for modelling the experimental results.

Kinematic effects taken into account in the model allows to the model to tend to what occurs in reality. Indeed, the predicted results obtained with the model agree quite well with the experimental results for any loading condition.

The model works well with the experimental data and the kinematics of dapped-end connection is taken into account. For all these reasons, this model gets a good perspective to be more developed in the future by including factors or agents that contribute to the serviceability of the dapped-end such as water or salt that are the first causes of damage of these structures.

Résumé

Ce travail de fin d'étude a pour but de modéliser le comportement de l'extrémité de poutres en béton fibré subissant une réduction de section (FRC dapped-end connections). Ces connections sont soumises à une concentration de contraintes dûe à leur réduction brusque de section et cela entraine généralement une rupture soudaine. L'utilisation du béton fibré augmente la ductilité du matériau et permet de prévenir une éventuelle rupture de l'élement. Le modèle cinématique prend en compte les conditions de service du dapped-end et ne se limite pas à un dimensionnment aux états limites ultimes. En réalité, cette méthode permet d'évaluer l'état structurel en mesurant des données in situ.

Le modèle étudié ne s'applique qu'à un seul type de rupture de l'élément, une rupture par flexion régie par une fissure diagonale partant du coin rentrant de la connection. Ce mode de rupture est le mode le plus fréquent pour les structures testées en laboratoire et d'autant plus fréquent que la quantité de fibres ajoutées dans le béton est grande. Les résultats théoriques obtenus sont comparés aux données expérimentales récoltées dans différents documents scientifiques. Ces données ont été analysées de la manière la plus précise possible pour permettre la validité des résultats.

Dans un premier temps, le modèle cinématique est dévelopé via une approche simplifiée qui permet de prédire la capacité maximale d'un dapped-end. Globalement, cette approche est très similaire de l'approche développée par Rajapakse et al. appliquée à des structures en béton armé. Les résultats obtenus pour les connections renforcées de fibres métalliques sont conlcuants.

Une seconde approche consiste à étudier le comportement complet d'un élément. Cette approche ne se limite pas à atteindre la capacité maximale réelle mais aussi à modéliser l'évolution de la fissure principale. Certains paramètres ont été modifiés afin de calibrer le modèle avec les résultats expérimentaux.

Les effets cinématiques pris en compte dans le modèle lui permettent de simuler la réalité. En effet, les résultats théoriques obtenus via le modèle correspondent de manière semblable aux données expérimentales récoltées et ce pour tout état de chargement.

Le fait que le modèle imite bien la réalité et qu'il tienne compte des effets cinématiques du dapped-end, il est possible de développer davantage le modèle en incluant d'autres facteurs qui pourraient influencer certains paramètres comme l'infiltration de l'eau ou de sels dans les fissures qui est la première cause d'endommagement de ces structures.

Contents

List of Figures

List of Tables

1 Introduction

1.1 General

Dapped-end beams (DEB), also known as Gerber beams, are a widely used support in existing structures due to their ease of assembly. However, DEB's can undergo an abrupt changes in the cross-section, which causes a very localized stress concentration, see FIGURE 1.1. Cracks appear and become a potential source of infiltration of water, salts or other external agents that compromise the durability of the structure.
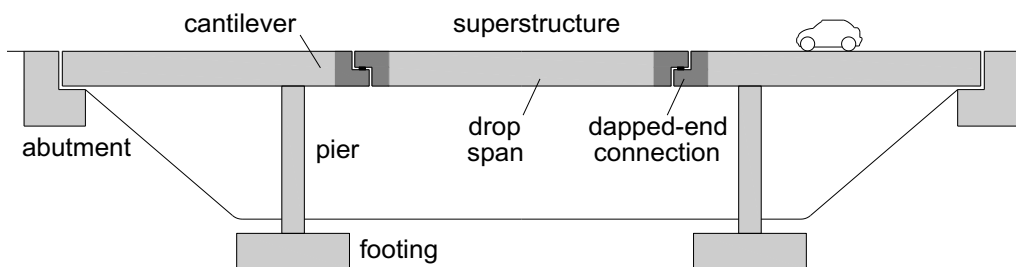
Figure 1.1: Typical bridge with dapped-end connections [29]

These DEB's are considered to be a D-region of the beam. In general, a strut-and-tie model is used in D-regions. In contrast, this model only designs dapped-end connections at ultimate limit state without taking into account the behavior of the dapped-end under service loads. Dapped-end connections are located at bridge supports, where water can stagnate and infiltrate more easily, which in turn reduces the durability of the dapped-end, see FIGURE 1.2. Water goes inside the crack where corrosion can be seen along the cracks. The more the structure is damaged, the more it will have to be monitored and the sooner it will have to be replaced, which results in high maintenance and repair costs. Research is always oriented to innovate and improve the materials. The present study will focus on the behavior of fiber-reinforced concrete (FRC) dapped-end connections. Currently little used in existing structures, FRC would improve the tensile behavior of concrete and provide a more ductile behavior.

Figure 1.2: Example of a dapped-end connection with durability problems [17]

To conduct an analysis of these structural elements under service loads, a kinematic model was developed by Rajapakse et al, see REFERENCE [29]. This model simulates the structure responses to the stresses that it will undergo. It allows to evaluate the state of the element during its lifespan based on data collected in situ and thus to make predictions. The models generally used for design, such as a strut-and-tie model, do not have the capacity to analyze the evolution of the dapped-end during its lifespan. Furthermore, a strut-and-tie model neglects the tensile strength of the concrete while fibers make a tensile contribution to the concrete that can be included through the kinematic model.

The model developed by Rajapakse et al. will form the basis of the model developed in this study by including the FRC effects. The kinematic model applied to FRC will later be compared to a set of collected experimental data. These consistent data are based on tested specimens whose peak capacity is compared to those predicted by the kinematic model. It is important to note that dapped-end connections can be subjected to different failure modes. This kinematic model applies only to one failure mode, the most frequently encountered, and will therefore be representative of reality. Due to their abrupt change of section, dapped-end connections are subjected to high stress concentrations and a diagonal crack appears starting from the re-entrant corner. This diagonal crack opens as the load increases and a flexural failure occurs. The kinematic model is applied especially to this failure mode which occurs in most cases.

1.2   Purpose of the thesis

The purpose of this research is to extend the kinematic model developed for reinforced-concrete dapped-end connections by incorporating steel fibers in the concrete. By using a material with more ductile properties, this would reduce sudden failures. The kinematic model takes into account the kinematics of dapped-end connections and would allow the structural conditions of a dapped-end to be assessed by measuring data on existing structures. Moreover, the complete behavior of a dapped-end is studied to simulate the whole evolution of the dapped-end until its failure and to model the main diagonal crack.

1.3   Contents of the thesis

The following study is structured in six chapters, the appendix (containing detailed experimental data) and the bibliographic references.

Chapter 2 explains what fiber-reinforced concrete is and its interest in being used in a dapped-end connection. Then, each paper that contributed to the database is discussed.

Chapter 3 details the principle of the basic kinematic model applied to reinforced concrete structures, defines the geometrical and kinematic parameters of the model that are used to evaluate the flexural capacity of the dapped-end connection.

Chapter 4 extends the basic kinematic model to the dapped-end made of fiber-reinforced concrete. First, a simplified approach is developed to predict the peak capacity of a dapped-end. Then, the model studies the complete behavior of a dapped-end, observing its state during loading, as well as the evolution of the main crack.

Chapter 5 compares the predictions obtained via the model with the experimental data collected and studies the impact of some parameters on the behavior of a dapped-end connection.

Chapter 6 consists of a brief conclusion of the model and proposes a way to investigate the results based on the kinematic model.

2 Behavior of FRC dapped-end connections

2.1 Fiber-Reinforced Concrete (FRC)

FRC is a material composed of conventional concrete to which fibers are added. There is a wide variety of fibers: glass, steel, synthetic or natural fibers. This document considers only the behavior of steel fiber-reinforced concrete. Once the material is chosen, the choice of the shape comes. FIGURE 2.1 shows the different possible shapes and cross-sections of fibers, whether they are straight, end-hooked, rectangular, circular or adopt other particular shapes and sections.
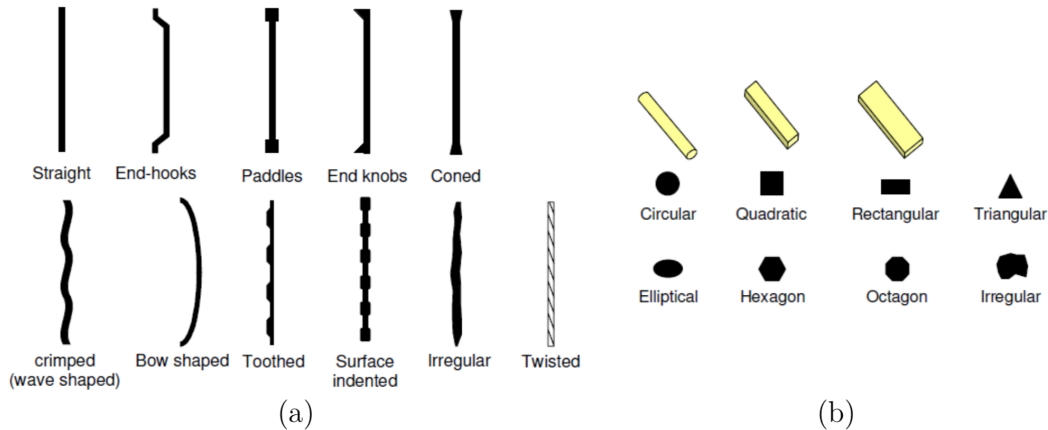
Figure 2.1: (a) Typical fiber geometries; (b) Typical cross-sections [22]

Concrete is a material that works very well in compression but has almost no tensile strength. For this reason, a steel reinforcement usually strengthens the concrete and supports the tensile forces. However, research is evolving very quickly, materials are always innovating to make them more resistant, reach greater spans and greater heights. The idea is therefore to reinforce conventional concrete with steel fibers. On the one hand, FRC homogenizes the reinforcement within the concrete and allows a better control of cracks. On the other hand, it increases considerably the tensile strength of the concrete. In terms of compressive strength, FIGURE 2.2 represents the effect of steel fibers on the concrete under compression. The addition of fibers in concrete slightly increases the strength in the post-peak phase as demonstrated by analyzing the FRC stress-strain relationship.
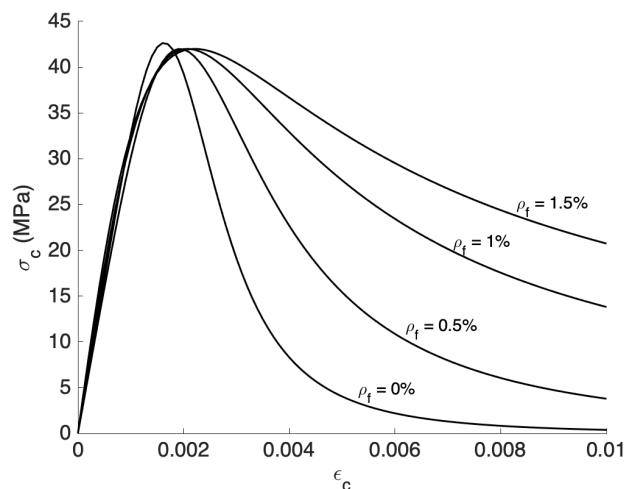
Figure 2.2: Effect of steel fibers on the concrete under compression for $f'_c = 42$ MPa

According to the diagram above, FRC is aimed at providing more ductility to FRC members in the post-peak behavior under compression. Indeed, the curve decreases significantly slower, which translates into a lower brittleness of the material, the material becomes more ductile.
The addition of fibers into concrete not only increases the tensile strength of the concrete but also reduces the crack width, crack spacing and increases the post-cracking ductility.

Because of its mechanical properties (increased tensile strength, increased ductility in compression,...), fiber-reinforced concrete reduces the amount of reinforcement needed to reinforce conventional concrete. Moreover, it facilitates the implementation of the work. By reducing the steel reinforcement and allowing a better control of cracks, FRC increases the concrete's durability. FRC reduces air voids and water voids in the concrete, which reduces the porosity of gel of the concrete. FRC is very effective in repairing structures due to the homogeneity of its reinforcement. Its ductile behavior allows to prevent sudden ruptures leading to disasters (bridge collapse, victims,...).

Although this material has been used for 50 years, it remains young in its field. Research is constantly advancing and the FRC is becoming more and more part of the design standards. Its use in existing structures is limited nowadays but the results obtained, especially in this study, are conclusive for a more frequent use of this material in construction in the future.

2.2 FRC applied to dapped-end connections

Due to their statical determinacy simplicity of construction, dapped-end connections are often used in common Gerber-beam to build reinforced concrete bridges as shown in FIGURE 1.1. Dapped-end connections transfer high shear forces in reduced sections which lead to susceptible brittle failures, see REFERENCES [2] & [18]. The change of geometry within the dapped-end induces a concentration of forces. The dapped-end connections are located at the junction of 2 bridge members, meaning at a discontinuity, which makes them sensitive to external agents (water, salts,...) and affects them to corrosion. As a result of a sudden and unexpected failure in the dapped-end connection, there are not any warnings to the users of the bridge. Consequently, it increases the danger for car drivers or pedestrians and when it happens, this has implications for traffic and the well-functioning of the road system, see FIGURE 2.3.

Figure 2.3: Collapse of the Concorde bridge in Quebec, Canada in 2006 [18]

Even before designing a dapped-end connection, it is important to know what kind of failure can occur during the collapse of the structure. The most common and recurring failure is the formation of a diagonal crack starting from the re-entrant corner, see FIGURE 2.4. Out of 212 tests of reinforced concrete dapped-end connections (without fibers), 99 of them presented a flexural failure along a crack from the re-entrant corner. This study will only address the case of flexural failure. Out of 20 tests with pictures of the specimens with FRC, 17 of them present a flexural failure. This failure mode occurs more often with FRC and is even more recurring when the amount of fibers increases. The other common failure mode is a shear failure due to an inclined crack starting from the support reaction, see REFERENCES [4] & [5].
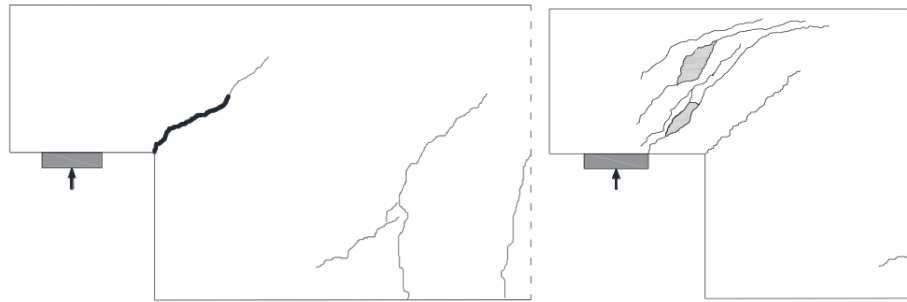
Figure 2.4: Common failure modes in dapped-end connections: flexural failure and shear failure [29]

FIGURE 2.5 shows the crack patterns of a dapped-end subjected to the peak load (on the left) and compared to the same specimen subjected to the ultimate load (on the right). The peak strength is obtained according to a flexural failure. However, the picture on the right illustrates a large inclined crack from the support reaction. Although this could induce errors, the peak capacity is reached for a flexural failure which takes precedence over the other failure mode. In reality, once the capacity of the structure is reached, other elements of the dapped-end take up the load and in turn reach their strength. This is marked by an improvement in ductility when fibers are added within concrete.

Figure 2.5: Crack patterns on specimen DEB-3.8 (T1) at peak load and ultimate load [15]

This means that it is important to analyze the dapped-end when it reaches its maximum load to ensure that the failure is a flexural failure mode. FIGURE 2.6 below represents a specimen whose picture was taken after the whole test was performed (after the ultimate load). A set of cracks starting from the re-entrant corner and others starting from the support are observed. This picture on FIGURE 2.6 does not allow to determine the failure mode corresponding to the peak resistance of the dapped-end. Although the results obtained via the kinematic model predict the shear failure mode, this is not consistent with what is studied and this type of specimen is not included in the database.
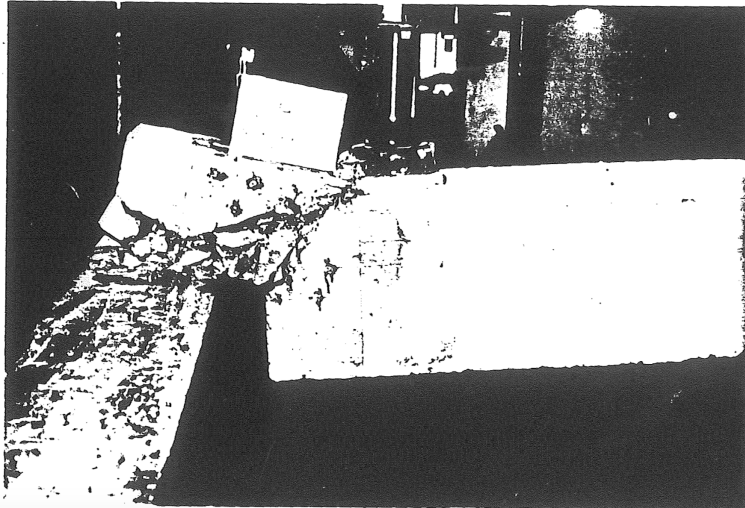
Figure 2.6: Failure mode of specimen B9 with 0.8% of fibers [1]

The application of FRC to dapped-end connections is aimed at reducing the cracks, particularly the diagonal crack starting from the re-entrant corner. Since dapped-ends are susceptible to brittle failures and are highly stressed, the use of FRC in this zone of the beam (see grey part of FIGURE 1.1) increases the ductility of the dapped-end and reduces the opening of the diagonal crack. Because fiber-reinforced concrete has a better post-peak behavior under compression and becomes more ductile, experimental tests show less and less concrete crushing failure at the top surface of the compression zone (located in the compression damage zone). Indeed, concrete works very well in compression but as soon as it starts to be damaged, its strength drops rapidly. In contrast, FRC has a better concrete damaged plasticity behavior. FIGURE 2.7 compares two experimental tests, one of which shows concrete crushing at the top surface of the dapped-end, while the other proves that the behavior of FRC is more ductile and that this type of failure mode occurs less often.
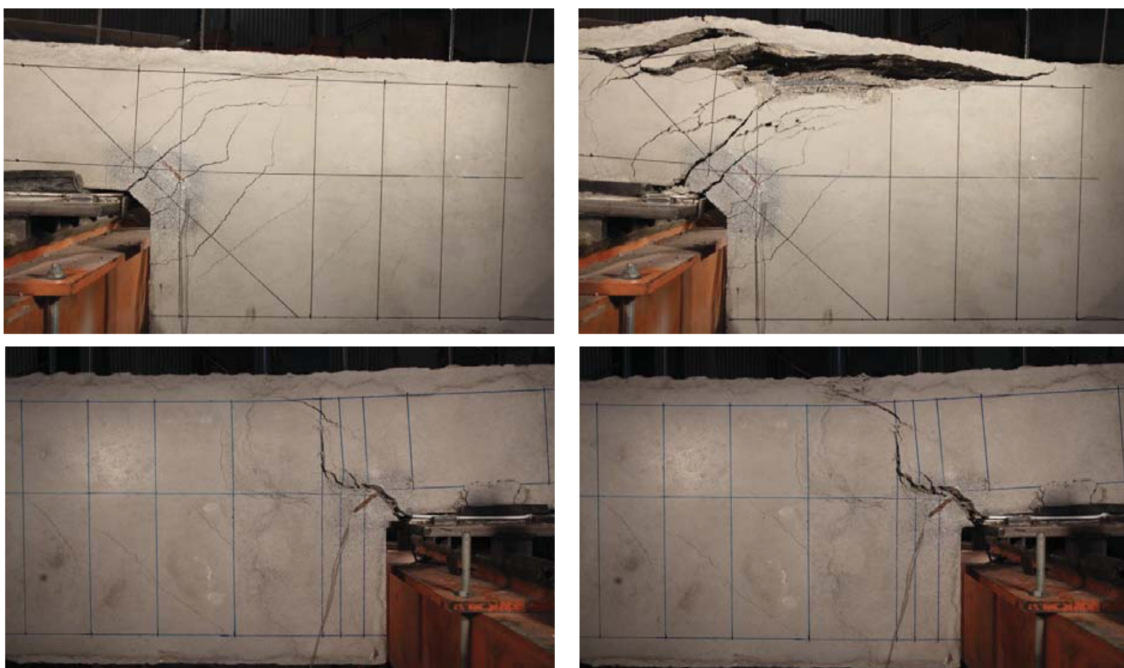
Figure 2.7: Concrete crushing without or with FRC (on the left dapped-end at peak load, on the right at ultimate load) for specimens DEB-3.5 (T2) & DEB-3.9 (T1)[15]

In addition to increasing the ductility of the concrete, the fibers will reduce the opening of cracks by their contribution to the tensile forces. The smaller the crack, the more difficult it will be for water and salt to enter into the concrete. Not only will the crack width grow more slowly but also the dapped-end will be able to support more shear forces for a given geometric design. All these reasons have an advantage not only in increasing the resistance of the dapped-end connection but also in the maintenance and restoration work. Consequently to FRC considerably reduces the crack width, the need for maintenance and monitoring of the dapped-end will reduce. Moreover, the ductile behavior of the FRC dapped-end connection also prevents from danger and allows to perform the necessary actions before an unexpected collapse.

2.3   Experimental data set

To model the behavior of dapped-end connections with FRC, experimental data have to be compared to predicted values. The data used must be of high precision, each measurement must be exact, without any assumption, the validity of the papers and results must be perfect and the data should ideally come from literature. However, the papers used to model the behavior of the experimental specimen do not provide all the information necessary to the model. Further, the details of each paper and each specimen are analyzed (with their data and different assumptions) to study the validity of the papers and determine data that should be used to model the behavior.

Globally, six papers containing FRC dapped-end experimental tests were found. Three of them are known in the scientific literature and three other papers were found but are not recognized as part of the scientific literature. The appendix includes all the information required for the model of the behavior of the dapped-end connections, from the details of each data to the different assumptions. The large database in the appendix also contains the predicted flexural capacity for each specimen and their comparison to the model.

2.3.1   Scientific literature

The first paper from the literature `"Effect of steel fibers on precast dapped-end beam connections"` made by *Ajina* in 1986 consists of 18 dapped-end experimental tests, although only 15 of them are usable because one configuration is designed without any reinforcement, see REFERENCE [1]. Within them two kind of dapped-end design according to their height were tested with different fiber volume ratios for each specimen (from 0 to 1.2%). The information and details of each test from the paper are relatively complete despite the unit of measurement based on the American convention (weight is expressed in pounds and stress in psi for example). Moreover, the tested samples have a very low height (107-120 mm), which amplifies the error very quickly for a lack of accuracy of the data.

The second paper from literature has been made by *Mata Falcón* in 2015 and named `"Estudio del comportamiento en servicio y rotura de los apoyos a media madera"`, see REFERENCE [15]. This paper gathers a set of data obtained by the experimentation of 60 tests realized corresponding to 30 different configurations. The study is focused on the influence of the variables of these configurations. Among others, the variables taken into account are: the quantity of reinforcement, the design of the reinforcement or the use of FRC. In order to study the behavior of dapped-end connections with FRC, 8 tests (from 4 different configurations) were included in the database. Each configuration differs simply by the fiber volume ratio added to the concrete (0-1.24%) and the concrete compressive strength. This paper provides a large amount of precise information including the

measurement of the crack width at the re-entrant corner. This type of information will allow the comparison of the experimental-to-predicted complete behavior. Additional information such as the type of failure or the angle of inclination of the crack from the re-entrant corner can be obtained from pictures taken at different stages of the loading of the specimen. Moreover, due to its dimensions (with a total height of 600 mm), the design of the dapped-end allows to obtain very representative results by minimizing the errors made.

A third paper written by *Özkılıç et al.* about `"Experimental and numerical investigations of steel fiber reinforced concrete dapped-end purlins"` aims at increasing shear capacities and energy dissipation according to the use of steel fiber-reinforced concrete, see REFERENCE [27]. The transition from the nib to the full beam is not instantaneous but progressive due to the inclination of the concrete. In addition, the width of the beam cross-section varies according to the height. Since the model developed later only includes sections of constant width, the tests from this paper cannot be applied to the model but some data from this paper lead to other scientific papers which give constitutive laws applied to the kinematic model.

2.3.2 Other scientific papers

The first paper is from the 33rd conference on `Our world in concrete & structures` given by *R.N. Mohamed & K.S. Elliott* (University of Nottingham, United Kingdom) in 2008, see REFERENCE [13]. Due to the abrupt change in the cross-sectional dimensions of dapped-ends, the dapped-ends undergo a concentrated applied load. Twenty experimental tests were investigated to study the dapped-end behavior with self-compacting steel fiber (hooked-end) reinforced concrete (SFSCC). In addition, a strut-and-tie model has been proposed in this paper and compares predicted to experimental results. Although a lot of information had to be assumed, the advantage of the studied specimens is their dimensions (a total height of 600 mm including 400 mm for the nib).

Another paper has been written by *Håvard Nedrelid* (Norwegian University of Science and Technology) in 2015, see REFERENCE [24]. Nedrelid has proposed a `COIN design` approach to assess the crack widths. This approach is compared to experimental results applied to members (with or without fibers) in bending, and then FRC beams with dapped-ends. Two types of fibers are used, namely 100% steel fibers or a mix with steel fibers and synthetic fibers. These experimental results were compared to the COIN design rules and a strut-and-tie model was suggested. Among the experimental tests performed on dapped-ends, only those made of steel fiber-reinforced concrete will be included in the database. The geometrical dimensions of the cross-section are relatively small (400 mm total height, 200 mm for the nib) and a large number of data are assumed (reinforcement and fiber strength, position of the reinforcement,...).

A second paper from the Norwegian University of Science and Technology conducted by *Hanna Haugen Nordbrøden & Siri Hansen Weydahl* as a Master's thesis is aimed at understanding the use of steel fibers as a substitute to conventional reinforcement, especially applied to corbel-end beams (also called dapped-end beams), see REFERENCE [26]. The first part of the paper is devoted to the theoretical study of dapped-ends according to different models (Norwegian preliminary design guidelines, fib's model code, strut-and-tie model,...). Furthermore, 10 experimental tests are performed with 5 different dapped-end configurations and different amount of fibers (0-1% volume). Among the 5 configurations, only 4 of them will serve the database because of the lack of vertical reinforcement, which will later make the model inapplicable, for a total of 8 tests. Subsequently, the established models are compared to the experimental results. Although the height of the samples is relatively small (150 mm

for the nib and 300 mm total height), the details of each configuration given in the appendix are very accurate and claim to present results minimizing errors.

2.3.3 Database

The following TABLE consists in a short resume of the database and gives an overview of the data. It contains the principle characteristics of the specimens from different papers. The total database can be found in the appendix.

Ref.	a/d	a (mm)	d (mm)	h (mm)	b (mm)	f'_c (MPa)	θ (deg)	ρ_f (%)	l_f/d_f	d_f (mm)	Type of fibers
[1]	1.04 - 1.36	114.3	84.1 - 109.5	101.6 - 127	127	29 - 31.3	45	0 - 1.2	100	0.508	hooked-end
[15]	0.8	200	250	300	250	31.1 - 48.8	31-58	0 - 1.24	65	0.55	hooked-end
[13]	0.27 - 0.471	100	365-369	400	300	42 - 49	53-59	0 - 1	65	0.55	hooked-end
[24]	0.6	100	167	200	200	43.2 - 63.6	45	0 - 1	65	0.9	hooked-end
[26]	0.83 - 0.85	100	117 - 120	150	200	40.5 - 52.3	31-62	0 - 1	65	0.9	hooked-end

Table 2.1: Overview of the database and gives an overview of the data. It contains the principle characteristics of the specimens from different papers. The total database can be found in the appendix.

Table 2.1: Overview of the database: a = distance from the support reaction to the face of the full-depth section; d = effective depth of the dapped-end; h = total depth of the dapped-end nib; b = width of the section; f'_c = concrete cylinder strength; θ = measured angle of inclination of the crack at the re-entrant corner; ρ_f = fiber volume ratio; l_f/d_f = fiber aspect ratio; d_f = fiber diameter

3 Kinematic model for assessment of failure along re-entrant corner cracks in existing RC dapped-end connections

Dapped-end connections are generally designed on the basis of a strut-and-tie model, most of the methods for predicting the flexural capacity of a structure are also based on this approach, see REFERENCES [30], [31] & [33]. The strut-and-tie model consists in representing the compressive forces in the concrete by the struts and the tensile reinforcement by the ties. Although the strut-and-tie model is very effective for design, it does not consider the effects of the kinematics of the inclined crack on the flexural capacity, see REFERENCE [23]. Therefore, it is difficult to use the strut-and-tie model to monitor and evaluate existing dapped-end connections. Indeed, it will only be possible to use this model to assess deformations and not forces. The kinematic model presented in this study is aimed at assessing forces based on the angle of the inclined crack from the re-entrant corner.

The kinematic model is based on the equilibrium of the forces, the kinematics of the inclined crack and constitutive relationships. This approach aims at putting the inclination of the crack according to the horizontal axis passing through the re-entrant corner and with the properties of each material used into dapped-end connection to assess the behavior of the dapped-end and its flexural capacity. Assuming a flexural failure, this model takes into account the crack width located at the dapped-end reinforcement, the length of the crack and the rotation that occurs around the tip of the crack.

3.1 Kinematics of the model

This approach applies to dapped-end connections whose behavior is governed by the opening of the inclined crack at the re-entrant corner. The behavior of dapped-end connections is characterized by tensile deformation of the reinforcement through the crack as well as large deformations in the concrete in compression above the tip of the crack. The kinematic model assumes that the crack is straight and inclined at an angle θ to the horizontal axis, where θ is a measurable angle on existing structure whose crack formation has already been initiated. Dapped-end connection consider two blocks located on either side of the crack and rotating relative to each other. The relative rotation of one block with respect to the other one causes compressive deformations in the part above the tip of the crack. Once the maximum compressive strain of the concrete ε_{c0} is reached, a compression damage zone (CDZ) is formed, see FIGURE 3.1.

The form of the CDZ is assumed to be a V-shaped as the geometry of damage zones for reinforced-concrete beams governed by flexural failure, see REFERENCES [35] & [36]. The CDZ is bounded by the surface at the top of the dapped-end and two planes inclined at an angle α to the horizontal axis. The value of this angle not being covered in the literature, is calibrated by optimization of the model in comparison with 47 experimental tests. The value retained is the one that gives the best average experimental-to-predicted ratios and a coefficient of variation as low as possible. After studying these two factors, the value retained is $\alpha = 50°$.

In terms of strain in the CDZ, the flexural capacity is reached by concrete crushing and therefore the strain, assumed constant along the depth of the CDZ d_{CDZ}, is estimated at $\varepsilon_{CDZ} = -0.0035$, see REFERENCES [3] & [19]. The strain along the compression undamage zone varies linearly from ε_{c0} at the bottom of the CDZ to zero at the tip of the crack. With this strain profile, the depth of the CDZ
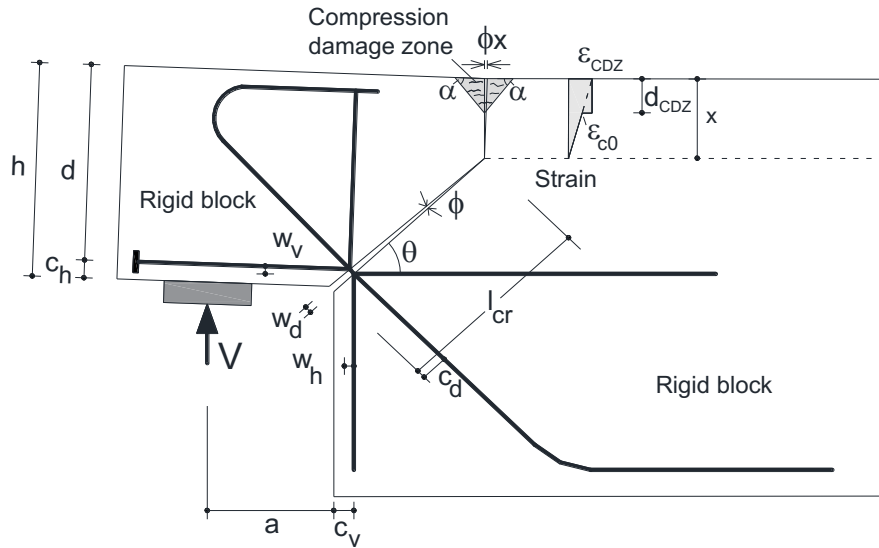
Figure 3.1: Kinematics of dapped-end connections governed by the widening of an inclined crack (only the main reinforcement of the connection is shown for the sake of clarity) [29]

can be expressed as:

$$d_{CDZ} = \left(1 - \frac{\varepsilon_{c0}}{\varepsilon_{CDZ}}\right) x \tag{1}$$

where x is the depth of the compression zone. This variable is the unknown of the model and will be obtained by horizontal equilibrium of forces.

The compression in the CDZ causes a shortening of the concrete at its top by the relative rotation of the two rigid blocks. This shortening is expressed as ϕx and is easily obtained with the strain ε_{CDZ}. It comes the following expression:

$$\phi = \frac{(2d_{CDZ}\cot\alpha)\,\varepsilon_{CDZ}}{x} \tag{2}$$

By using θ as the inclination of the crack, the length of the crack is expressed as:

$$l_{cr} = \frac{(h-x)}{\sin\theta} \tag{3}$$

where h and x are respectively the depth of the dapped-end and the depth of the compression zone.

3.2 Evaluation of the Flexural Strength

In order to determine the peak resistance of the dapped-end subjected to flexural failure, it is necessary to calculate the depth of the compression zone x. According to the rules of flexural calculations of a member, the depth x is evaluated by solving a horizontal equilibrium of the forces acting on a free body diagram of the dapped-end, see FIGURE 3.2. The horizontal forces taken into account are the external force H, the forces due to the concrete in compression in the CDZ F_{CDZ} and in the compression undamage zone F_{c0} as well as the forces in the reinforcements. This equilibrium is solved by an iterative procedure in which the value of x is changed at each iteration by using the bisection
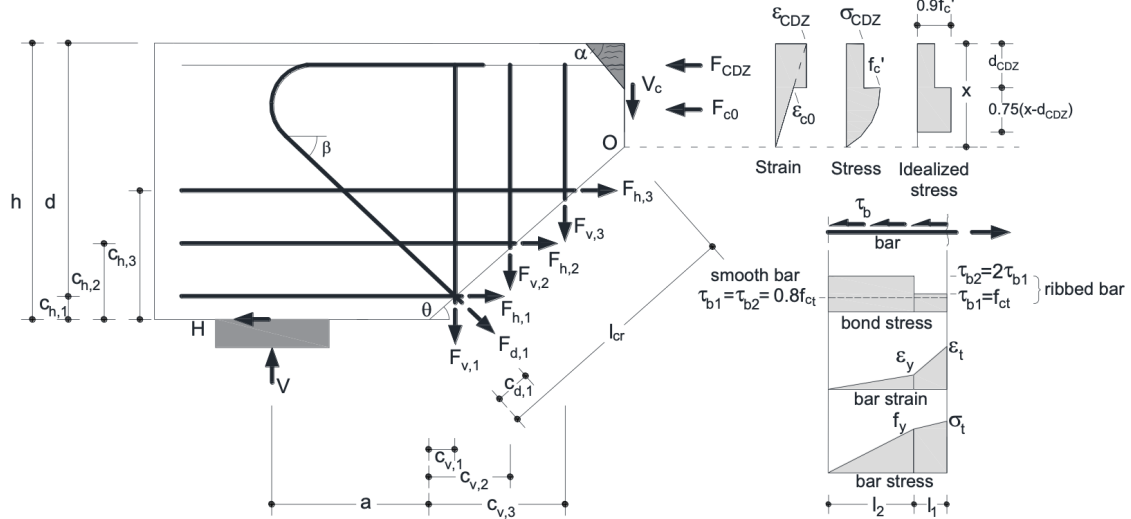
Figure 3.2: Forces acting on the free body diagram of the dapped-end connection governed by a failure due to the inclination crack from the re-entrant corner [29]

method until the horizontal equilibrium is satisfied.

For a given value of x and an angle of inclination of the crack θ, it is possible to determine the geometrical and kinematic parameters of the model. The depth of the CDZ d_{CDZ} is obtained from equation (1) and the relative rotation angle ϕ by using equation (2).

The crack widths at the reinforcements are obtained from the three equations (4)-(6). Three types of reinforcement are mainly used and are differentiated by their position in the dapped-end connection (horizontal, vertical or diagonal). Horizontal and vertical reinforcement apply respectively horizontal and vertical resulting forces. However, a diagonal reinforcement has two components that are considered as two forces (one horizontal and another one vertical). To assess the stress into a reinforcement located in the crack, the crack width at a reinforcement has to be evaluated. The following expressions assess the crack width at a reinforcement i and consider the 3 cases (horizontal, vertical and diagonal reinforcement respectively).

$$w_{h,i} = \phi \times \left(l_{cr} \sin\theta - c_{h,i} \right) \tag{4}$$
$$w_{v,i} = \phi \times \left(l_{cr} \cos\theta - c_{v,i} \right) \tag{5}$$
$$w_{d,i} \approx \phi \times \left(l_{cr} - c_{d,i} \right) \tag{6}$$

where $c_{h,i}$, $c_{v,i}$ and $c_{d,i}$ are the distances from the re-entrant corner to the reinforcement i horizontal, vertical or diagonal respectively.

Once the previous parameters are obtained, it is possible to calculate the resulting forces in the compression zone. Those calculations are performed by assuming a certain strain at the top surface of the concrete ($\varepsilon_{CDZ} = 0.0035$). The stress-strain relationship used for RC dapped-ends is based on the Popovics model as extended by Collins et al., see REFERENCES [28] & [11]. The compression force in the CDZ is assessed by using equation (1) and expressed as following:

$$F_{CDZ} = \sigma_{CDZ} d_{CDZ} b \tag{7}$$

where σ_{CDZ} is the stress in the CDZ and b is the width of the dapped-end connection.

The stress located in the compression undamage zone is assumed as a rectangular block under flexural stress as shown in FIGURE 3.2. In this zone the resulting force is assessed as following:

$$F_{c0} = \left(0.9 f_c'\right) 0.75 \left(x - d_{CDZ}\right) b \tag{8}$$

where f_c' is the concrete cylinder strength. The factors 0.9 and 0.75 are used based on the maximum strain of ε_{c0} by assuming a parabolic strain-stress relationship as shown in FIGURE 3.2, see REFERENCE [28]. The total horizontal force applied in the compression zone is the sum of the three forces F_{CDZ}, F_{c0} and the reinforcement included in the compression zone. These forces have to be in equilibrium with the sum of the horizontal forces applied by the horizontal components of each reinforcement through the crack as well as the external force H, see equation (14).

To assess the tensile forces in the dapped-end reinforcements crossing the crack, it is necessary to evaluate the crack at each reinforcement and to link crack width w and tensile stress σ_t. This relationship has already been established by Sigrist, see REFERENCE [32]. The Sigrist model is a mechanical model assuming that the reinforcement is anchored in the concrete by bound. In this model, two parts of the anchorage of the reinforcement are considered, l_1 and l_2 : l_1 is located at the crack face where the yield of the reinforcement is reached and l_2 further into concrete where the yield of the reinforcement is not reached and the reinforcement still follows an elastic behavior as shown in FIGURE 3.2 on the right of the diagram. However, a difference between smooth bars and ribbed bars are made. In the past, during the discovery and for the first reinforced concrete structures to build bridges (at the end of the 19th century), smooth bars were used but then, for a better steel-concrete adhesion and to reduce cracks, the smooth bars have been replaced by ribbed bars. Nowadays, ribbed bars are used in most applications and generally in bridges so that all the experimental data collected only include ribbed bars.

Considering only ribbed bars, the bond stress between the rebar and the concrete is assumed as a constant value τ_{b1} and $\tau_{b2} = 2\,\tau_{b1}$ along the lengths l_1 and l_2 respectively and where $\tau_{b1} = f_{ct} = 0.3 \left(f_c'\right)^{2/3}$, see REFERENCE [16]. The following expressions assess the crack displacement based on the equilibrium of the bar:

$$w = \frac{1}{2}\left(\varepsilon_t + \frac{f_y}{E_s}\right) l_1 + \frac{1}{2}\min\left(\varepsilon_t, \frac{f_y}{E_s}\right) l_2 \tag{9}$$

$$l_1 = \max\left(\sigma_t - f_y, 0\right) \frac{d_b}{4\tau_{b1}} \tag{10}$$

$$l_2 = \min\left(\sigma_t, f_y\right) \frac{d_b}{4\tau_{b2}} \tag{11}$$

where f_y is the yield strength of the reinforcement, d_b is the diameter of the bar, E_s is the modulus of elasticity of the steel (usually equals to 200 000 MPa) and ε_t is the strain in the reinforcement in the crack. Once the crack width is calculated with the equations (4) to (6) and by using the equations (9)-(11), the value of the strain in the reinforcement ε_t is easily deduced and then the tensile stress in the reinforcement σ_t from the following relationship:

$$\sigma_t = \varepsilon_t E_s \tag{12}$$

It easily comes the value of the force F_t applied to each reinforcement (as well vertical as horizontal and diagonal) by using the following expression:

$$F_t = A_b \sigma_t \tag{13}$$

where A_b is the area of the section of the bar.

Although the forces F_{CDZ} and F_{c0} due to the concrete in the compression zone, a force related to the reinforcement in the compression zone also contribute to the horizontal equilibrium. The strain at the reinforcement is the same as that of the concrete in compression and depends on the position of the reinforcement in the CDZ. The stress and the tensile force $F_{rf,CZ}$ in the reinforcement are calculated from relationships (12) and (13) respectively.

Once the reinforcement stresses and the corresponding forces are solved, the following horizontal equilibrium is solved to determine the depth of the compression zone x:

$$\sum_i F_{h,i} + \sum_i F_{d,i} \cos\beta - H = F_{CDZ} + F_{c0} + F_{rf,CZ} \tag{14}$$

where index i corresponds to the number of reinforcement and β is the inclined angle of the diagonal reinforcement.

By considering a moment equilibrium around the point O located at the tip of the crack, the shear support at failure for a strain value at the top fiber of the compression zone assumed at 0.0035 is assessed by solving the following equation:

$$
\begin{aligned}
V_{\text{pred}} = \frac{1}{(a + l_{cr} \cos\theta)} \Big\{ & \sum F_{h,i} \left(h - x - c_{h,i} \right) \\
& + \sum F_{v,i} \left(l_{cr} \cos\theta - c_{v,i} \right) + \sum F_{d,i} \cos\beta \sin\theta \left(l_{cr} - c_{d,i} \right) \\
& + \sum F_{d,i} \sin\beta \cos\theta \left(l_{cr} - c_{d,i} \right) + 0.625 F_{c0} \left(x - d_{CDZ} \right) \\
& + F_{CDZ} \left(x - 0.5 d_{CDZ} \right) - H \left(l_{cr} \sin\theta \right) \\
& + F_{rf,CZ} \left(x - c_{rf,CZ} \right) \Big\}
\end{aligned}
\tag{15}
$$

where a is the span of the dapped-end, $c_{h,i}$, $c_{v,i}$ and $c_{d,i}$ the distances from the re-entrant corner respectively to an horizontal, vertical and diagonal reinforcement i, $c_{rf,CZ}$ is the concrete cover of the reinforcement in the compression zone and β is the angle of inclination of the diagonal reinforcement with the horizontal axis.

3.3 Flowchart of the solution procedure

The kinematic model is solved by using an iterative procedure as described in the flowchart shown in FIGURE 3.3. Once the depth of the compression damage zone is fixed, all the geometrical and kinematic parameters are computed. If the horizontal equilibrium is satisfied, the flexural capacity can be calculated, otherwise the depth of the CDZ is modified and the solution procedure is repeated.
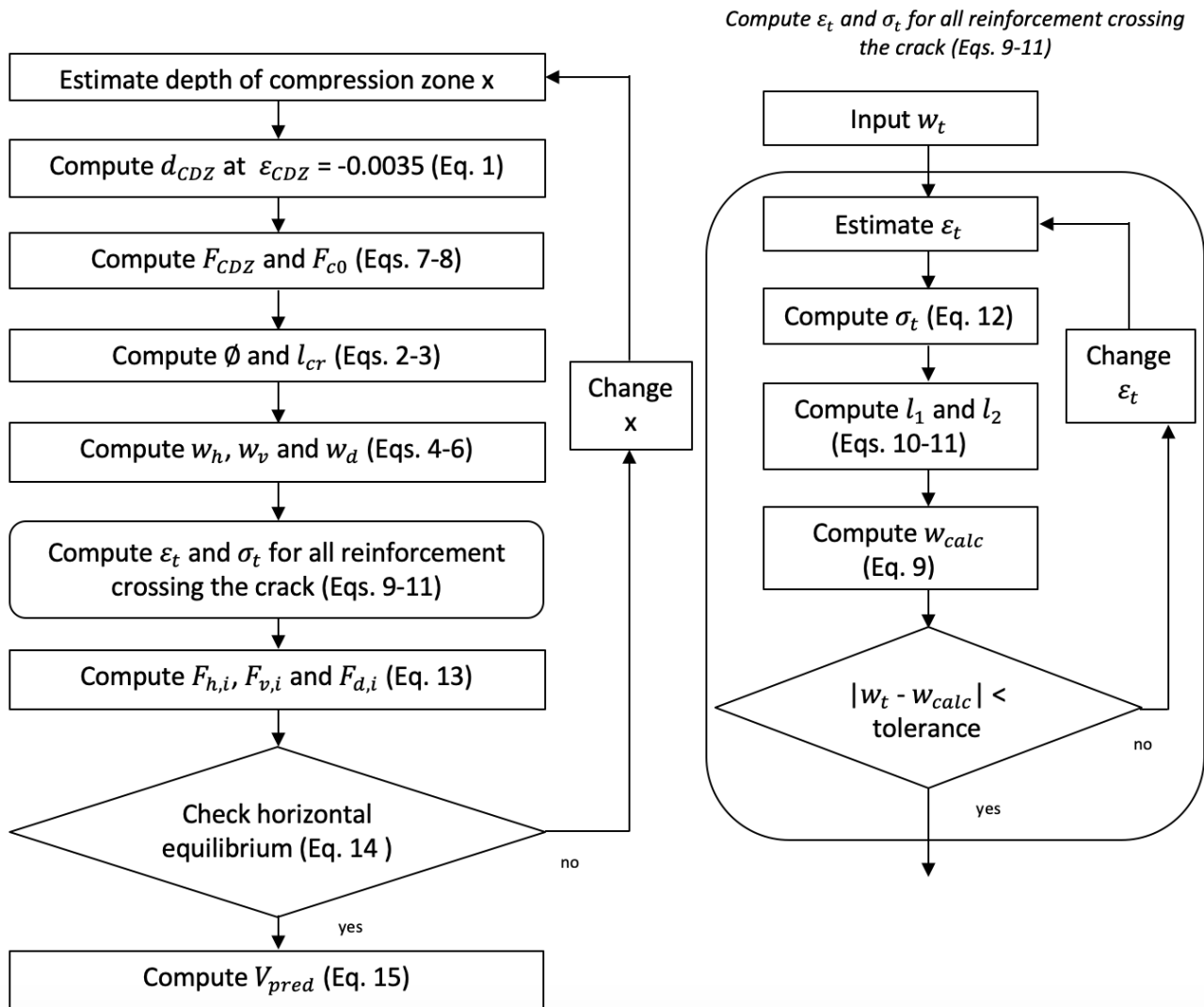
Figure 3.3: Simplified approach - Procedure of the kinematic model applied to RC dapped-end connections

4 Extended kinematic model to FRC dapped-end connections

Dapped-end connections are governed by a flexural failure due to the opening of a crack from the re-entrant corner. These connections transfer high shear forces in a reduced section, which lead to a potential sudden failure. Using FRC in dapped-end connections is aimed at enhancing their tensile strength, controlling the cracks and improving the ductility of the structures.

This study proposes to model the behavior of dapped-end connections with FRC. The model is basically based on the kinematic model explained previously and modified including the contribution of the fibers within the concrete. The fibers have the impact to increase significantly the tensile strength of the concrete and to modify a bit the stress-strain relationship under compression. A resulting tensile force has to be added from the crack and the post-peak behavior of the stress-strain curve is different. The curve stays high after the peak and does not decrease rapidly as the conventional concrete without any fibers so that the dapped-end leads to a ductile behavior.

The first approach has been developed as a simplified approach considering a peak resistance for a certain strain at the top of the concrete surface assumed at 0.0035.

However, a dapped-end does not especially reach its peak resistance for ε_{top} = -0.0035. It is therefore interesting to study the complete behavior of the dapped-end, by initiating the strain at the top at 0 and to increase it until reaching the peak resistance of the member. The complete behavior will also model the evolution of the opening of the crack (and therefore the crack width) according to the strain in the concrete.

4.1 Simplified approach for peak response

The first simplified approach is aimed at capturing the peak resistance of a dapped-end connection with steel fiber-reinforced concrete by using the inclined angle of the crack θ as an input as well as the model developed previously. The concrete from each side of the crack is still idealized as two rigid blocks rotating around the tip of the crack. This relative rotation ϕ leads to deformations in the compression zone located above the tip of the crack. The deformation at the top fiber of the compression zone leads to a compression damage zone (CDZ) bounded by the top surface of the concrete and two inclined planes at an angle α with the horizontal axis, see FIGURE 3.1. Without any recommendation in the literature, α is assessed by comparisons with the tests from the experimental data to the predicted values from the model. The value of α has been assessed at 50° to get the best average experimental-to-predicted ratio and the least coefficient of variation in the simplified kinematic model applied to reinforced concrete dapped-end connections. By using the same α, the simplified approach for FRC also results in good predictions.

The strain state of the compression zone is linear along the depth of the compression zone starting at zero from the bottom of the compression zone (at the tip of the crack) to ε_{top}. In this approach, a strain $\varepsilon_{top} = \varepsilon_{CDZ}$ = -0.0035 is assumed at the top surface of the concrete in the compression zone to predict the peak response. This value is consistent with a flexural capacity governed by concrete crushing. In the compression damage zone, the strain is assumed as a constant value equals to ε_{top}. The other geometrical and kinematic parameters, like relative rotation ϕ, length of the crack l_{cr}, crack displacements w, are also determined from equations (2) to (6).

4.1.1 Effect of the steel fibers on the flexural behavior of dapped-end connections

To assess the peak resistance of the dapped-end, it is necessary at first to evaluate the depth of the compression zone x identically to what has been done previously. This value is obtained from a horizontal equilibrium of the forces acting on the dapped-end. These forces are basically the same as the ones used in the basic kinematic model although some forces due to the concrete are assessed differently and the contribution of the fibers crossing the crack results to a tensile force, see FIGURE 4.1.
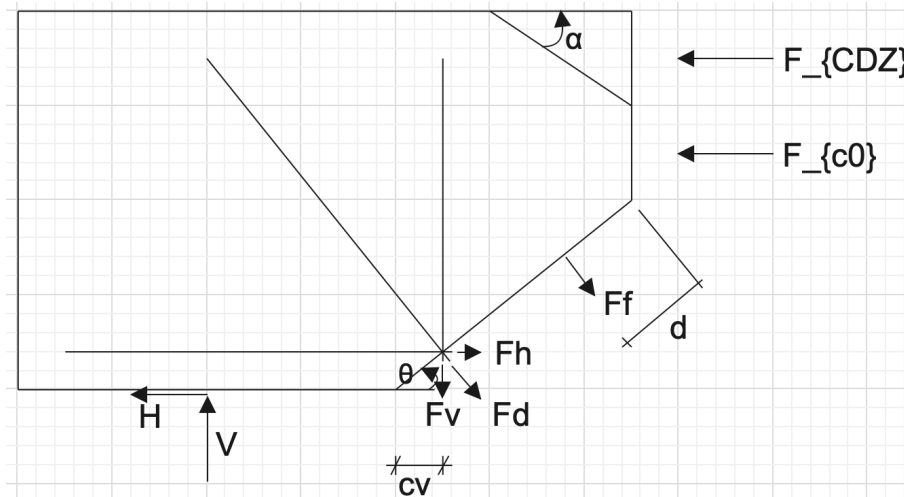
Figure 4.1: Forces acting on the free body diagram FRC dapped-end

The strain state in the compression zone is similar to the model without FRC (see CHAPTER 3), the strain starts from 0 at the bottom of the compression zone and increases linearly along the depth of the compression zone up to the top surface of the zone. The stress for fiber-reinforced concrete is assessed by using a different constitutive law as the one proposed for conventional concrete. The behavior of FRC is illustrated in the FIGURE 4.2 and compared to conventional concrete according to the stress-strain relationship. For the sake of simplicity, the pre-peak compressive behavior of FRC is modelled similar to that of conventional concrete. The model used in the kinematic approach to assess the stress in the compression zone of reinforced concrete dapped-ends is based on the constitutive law proposed by Popovics as extended by Collins et al. (represented by the blue curve in the FIGURE). However, the behavior of FRC is pretty similar to Popovics but increases in the post-peak phase. Different models are proposed in the literature to model the FRC behavior under compression. In the paper written by Mihaylov et al. the model used is the one proposed by Lee et al. and the results obtained for deep beams were promising, see REFERENCES [23] & [21]. Different models are illustrated in FIGURE 4.2. It can be seen that Popovics illustrates the stress-strain relationship for conventional reinforced concrete and the two other ones for FRC (1.5% of fiber volume ratio). The curve based on stress-strain relationship proposed by Ezeldin et al. presents a pre-peak behavior quite similar to Popovics which makes sense because the fibers do not impact the pre-peak behavior of concrete under compression, see REFERENCE [14]. After the peak, the fibers enhance the behavior of the concrete and the ductility of the material. A difference appears with the model proposed by Lee et al. and for this reason the model will not be taken into account. This study will use the model proposed by Ezeldin based on the Popovics parameters to assess the contribution of the compressive concrete in the flexural capacity, see equation (16).

$$\sigma_{cf} = f'_c \frac{\beta \left(\frac{\varepsilon}{\varepsilon_{c1}} \right)}{\beta - 1 + \left(\frac{\varepsilon}{\varepsilon_{c1}} \right)^{\beta}} \tag{16}$$

$$\beta = 1.093 + 0.7132 (RI)^{-0.926}$$

$$\varepsilon_{c1} = \varepsilon_{c0} + 446 \cdot 10^{-6} \cdot (RI)$$

$$RI = \rho_f \frac{l_f}{d_f}$$

$$\varepsilon_{c0} = \frac{f'_c \cdot n}{E_c \cdot (n-1)} \text{(corresponding strain to maximum stress by using Popovics)}$$

$$E_c = 2200 \left(\frac{f'_c}{10} \right)^{0.3}$$

$$n = 0.8 + \frac{f'_c}{17}$$

where f'_c is the cylinder compressive strength, ε_{c1} is the strain corresponding to the peak (equivalent to ε_{c0} for conventional concrete), E_c is the modulus of elasticity of concrete, ρ_f is the fiber volume ratio and $\frac{l_f}{d_f}$ is the fiber aspect ratio with l_f the length and d_f the diameter of the fiber.
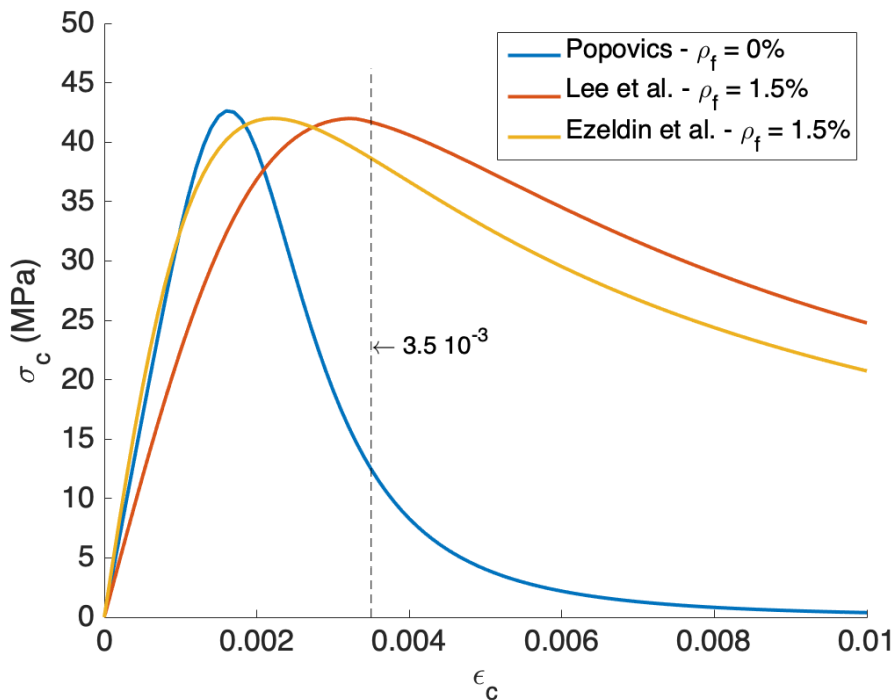
Figure 4.2: Comparison of different models on FRC under compression

By enhancing its behavior and ductility after the peak (the yellow curve in FIGURE 4.2 decreases slowly and not suddenly like the blue one), FRC contributes better to compressive forces for damaged concrete. To evaluate the stress σ_{CDZ} in the compression damage zone, the variable ε just has to be replaced by $\varepsilon_{CDZ} = 0.0035$ in equation (16). By assuming a constant strain in the CDZ, the resulting force in the CDZ is calculated from:

$$F_{CDZ} = \sigma_{CDZ} d_{CDZ} b \tag{17}$$

The stress in the compression undamage zone is assessed by using the evolution of the stress-strain curve according to the strain (from 0 to ε_{c1}). The average stress within this zone is obtained by dividing the area under the curve (between 0 and ε_{c1}) by the maximum strain ε_{c1}:

$$\sigma_{cf,avg} = \frac{A}{\varepsilon_{c1}} \tag{18}$$

The resulting force in the compression undamage zone comes as follows:

$$F_{c0} = \sigma_{cf,avg} d_{undmg} b \tag{19}$$

where d_{undmg} is the depth of the compression undamage zone also assessed from $d_{undmg} = x - d_{CDZ}$.

In addition to the forces in the compression zone, there is also another tensile stress across the main inclined crack from the re-entrant corner. In order to evaluate the stress along the crack, it is necessary first to assess the crack width along the crack. In this study, the crack is assumed as a straight crack from the re-entrant corner up to its tip. The relative rotation ϕ (expressed in radians) can also be seen as the opening angle of the crack. From equations (2) and (3), the crack width at the re-entrant corner is calculated from:

$$w_{max} = \phi l_{cr} \tag{20}$$

By analyzing this relationship, it easily comes that the crack width increases linearly along the crack starting at zero from the tip of the crack to w_{max} at the re-entrant corner.

Once the evolution of the crack width along the crack is determined, a relationship to model the tensile stress from the crack width has to be established. A model has been proposed by Lee et al, see REFERENCE [20]. This model considers hooked-end fibers and the tensile stress in the fibers is the contributions of the tensile stress composed of frictional bond in the straight part of the steel fibers (σ_{st}) and mechanical anchorage in the hooked-end part of the steel fibers (σ_{eh}).

$$\sigma_f = \sigma_{st} + \sigma_{eh} \tag{21}$$

Each contribution is defined in equations (22) and (23):

$$\sigma_{st} = \alpha_f \rho_f K_{st} \tau_{f,max} \frac{l_f}{d_f} \left(1 - \frac{2w}{l_f} \right)^2 , \text{MPa} \tag{22}$$

where,

- $\alpha_f = 0.5$ is the fiber orientation factor

- ρ_f is the fiber volume ratio

- $K_{st} = \begin{cases} \dfrac{\beta_f}{3}\dfrac{w}{s_f} & \text{for } w < s_f \\[2mm] 1 - \sqrt{\dfrac{s_f}{w}} + \dfrac{\beta_f}{3}\sqrt{\dfrac{s_f}{w}} & \text{for } w \geq s_f \end{cases}$

- l_f is the fiber length (expressed in mm)

- d_f is the fiber diameter (expressed in mm)

- $\tau_{f,max} = 0.369\sqrt{f_c'}$ is the bond stress between fibers and concrete

- f_c' is the FRC cylinder compression strength (expressed in MPa)

- w is the crack width

- $\beta_f = 0.67$

- $s_f = 0.01$ (expressed in mm)

And,

$$\sigma_{eh} = \alpha_f \rho_f K_{eh} \tau_{eh,\max} 2\left(\frac{l_i - 2w}{d_f}\right), \text{MPa} \tag{23}$$

where,

- $K_{eh} = \begin{cases} \beta_{eh}\left[\dfrac{2}{3}\dfrac{w}{s_{eh}} - \dfrac{1}{5}\left(\dfrac{w}{s_{eh}}\right)^2\right] & \text{for } w < s_{eh} \\[3mm] 1 + \left(\dfrac{7\beta_{eh}}{15} - 1\right)\sqrt{\dfrac{s_{eh}}{w}} - \dfrac{2\left(\sqrt{w} - \sqrt{s_{eh}}\right)^2}{l_f - l_i} & \text{for } s_{eh} \leq w < \dfrac{l_f - l_i}{2} \\[3mm] \left(\dfrac{l_i - 2w}{2l_i - l_f}\right)^2 K_{eh,i} & \text{for } \dfrac{l_f - l_i}{2} \leq w \leq \dfrac{l_i}{2} \end{cases}$

- $\tau_{eh,max} = 0.429\sqrt{f_c'}$ is the pull-out strength of a single hooked-end fiber

- $\beta_{eh} = 0.76$

- $s_{eh} = 0.1$ (expressed in mm)

- $K_{eh,i} = 1 + \left(\dfrac{7\beta_{ch}}{15} - 1\right)\sqrt{\dfrac{s_{ch}}{w_i}} - \dfrac{2\left(\sqrt{w_i} - \sqrt{s_{ch}}\right)^2}{l_f - l_i}$ with $w_i = \dfrac{l_f - l_i}{2}$

- l_i is the length of the straight part of the fiber

The relationship (21) considers steel hooked-end fibers. In this study, all the experimental tests collected in the database were performed with hooked-end fibers, which makes them completely consistent with the model proposed by Lee et al. In the case of straight fibers, it would be sufficient to set the contribution of the hooked end part (σ_{eh}) to zero and equation (21) would simply become $\sigma_f = \sigma_{st}$. Nowadays, the most commonly used steel fibers in concrete are *Dramix* fibers from BEKAERT company. Although the technical data sheets of these fibers refer to a large number of characteristics, the length of the straight part of a fiber is measured with a batten, see the photos in FIGURE 4.3. The hooked-end part measures 5 mm whatever the total length of the fiber, the length of the straight part is calculated from $l_i = l_f$-10 mm, also according to REFERENCE [34].
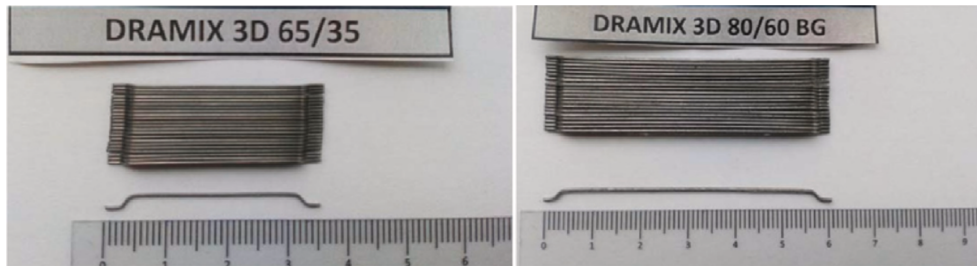
Figure 4.3: Fiber geometries used in this study (BEKAERT-Dramix) [27]

The relationship between crack width and stress σ_f in the fibers across the crack from equation (21) and its contributions σ_{st} and σ_{eh} established in equations (22) and (23) are illustrated in FIGURE 4.4. By using equation (20), the average stress in the fibers is assessed from:

$$\sigma_{f,avg} = \frac{A}{w_{max}} \tag{24}$$

where A is the area bounded by the curve of the stress in the fibers and the crack width at the re-entrant corner w_{max}.

In FIGURE 4.5, the evolution of the average tensile stress in the fibers according to the crack width at the re-entrant corner is studied. As long as the crack width at the re-entrant corner increases, the contribution of both straight and hooked-end parts of the fiber increases strongly. The stress in the fibers is proportional to the crack width up to a certain width and then it becomes inversely proportional and thus decreases despite the increasing crack width, see equations (22) and (23). The average stress keeps increasing until the crack width at the corner re-entrant reaches a value at which the fibers yield. As the crack opens, the effective crack length contributing to the tensile force decreases. The average stress then decreases as the opening of the crack increases, the fibers rupturing one after the other from the re-entrant corner to the tip of the crack.
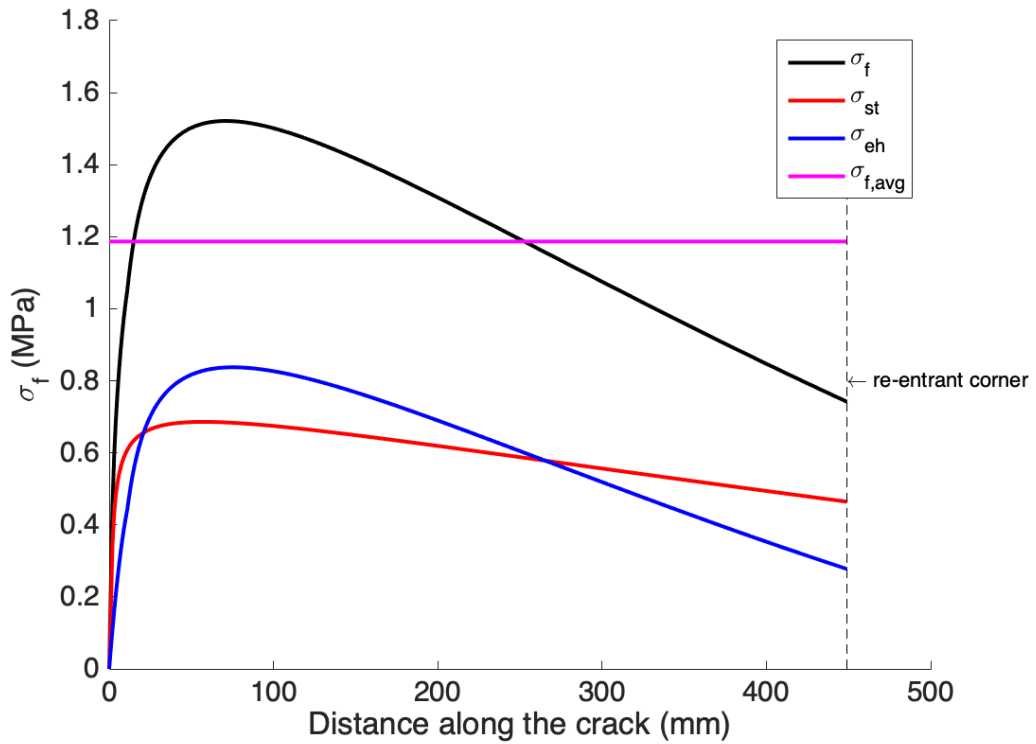
Figure 4.4: Evolution of the tensile stress in the steel fibers according to the crack width across the crack (from the tip of the crack to the re-entrant corner)
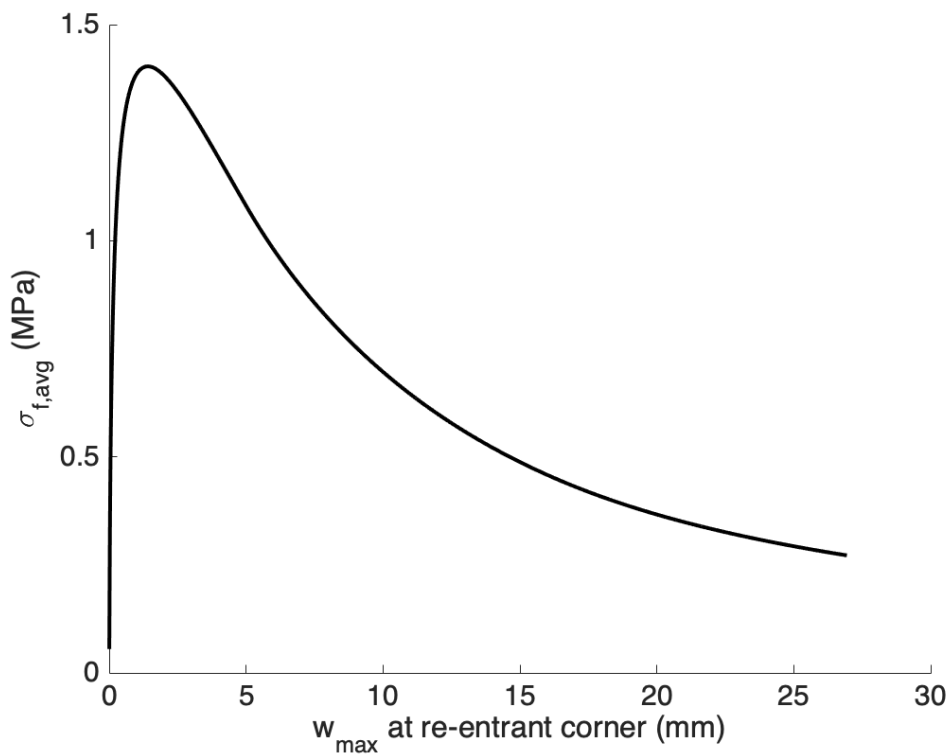
Figure 4.5: Evolution of the average tensile stress in the fibers according to the crack width at the re-entrant corner

The resulting tensile force in the fibers perpendicular to the crack is evaluated by multiplying the average stress to the area bounded by the length of the crack l_{cr} and the width of the dapped-end b:

$$F_f = \sigma_{f,avg} l_{cr} b \tag{25}$$

The tensile force in the fibers is added to the horizontal equilibrium with its horizontal component and it is now necessary to evaluate the level arm of this force applied to the moment equilibrium around the tip of the crack. To do it, the length of the crack is discretized in little steps, see FIGURE 4.6. For each step, a force F_i is assessed by multiplying the average of the two stresses σ_i and σ_{i+1} from the bounds i and i+1 by the length of the step i Δx and the width of the dapped-end b as following

$$F_i = \frac{\sigma_i + \sigma_{i+1}}{2} \Delta x b \tag{26}$$

And it comes the moment around the tip of the crack for an index i:

$$M_i = F_i \frac{x_i + x_{i+1}}{2} \tag{27}$$

This procedure is repeated for each step i, i+1, i+2,... and the moment around the tip of the crack is defined as:

$$\sum_i M_i = F_f \times d \tag{28}$$

$$\Longleftrightarrow d = \frac{\sum_i M_i}{F_f} \tag{29}$$

where d is the level arm of the tensile force in the fibers obtained by moment equilibrium around the tip of the crack.
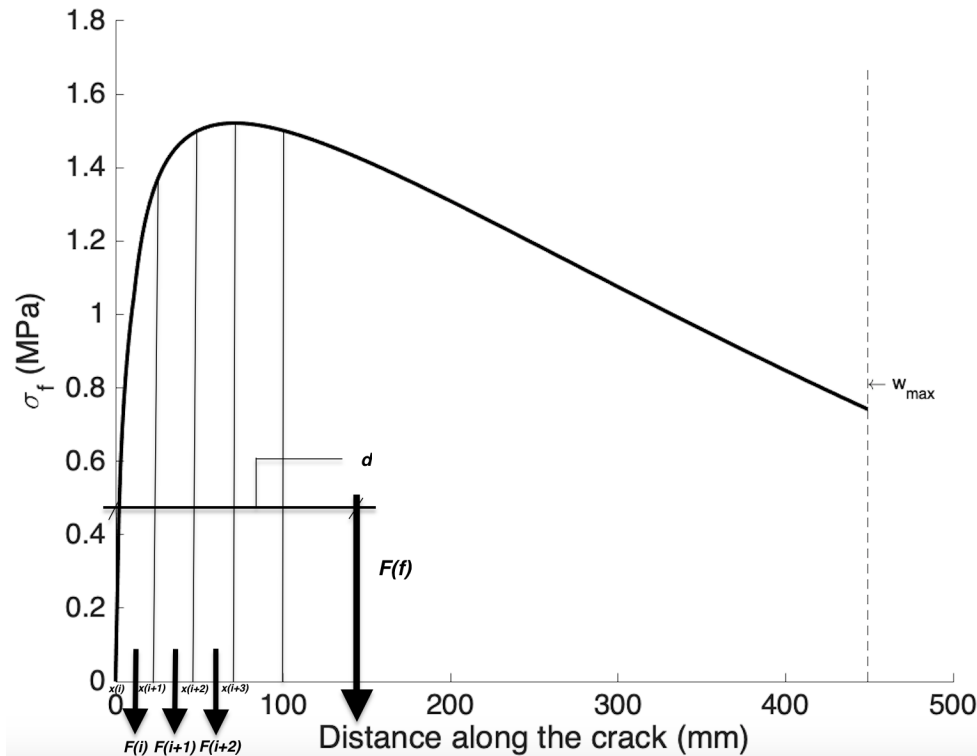
Figure 4.6: Diagram to determine the level arm of the resulting tensile force due to the fibers F_f

The level arm of the resulting force in the fibers around the tip of the crack gets smaller and approaches the rotation point of the moment equilibrium as the crack width at the re-entrant corner increases. Fibers at the re-entrant corner start with high stress but once the crack width reaches a value they rupture. Consequently, the tensile resulting force is displaced to the tip of the crack. In FIGURE 4.7 the evolution of the level arm of the tensile force (measured from the re-entrant corner to the position of the resulting force l_{cr} - d) is studied while the crack width at the re-entrant corner w_{max} increases. An asymptotic curve is illustrated which makes sense because as the crack opens the resulting tensile force approaches the tip of the crack and the curve converges to the length of the crack (l_{cr} = 449 mm).
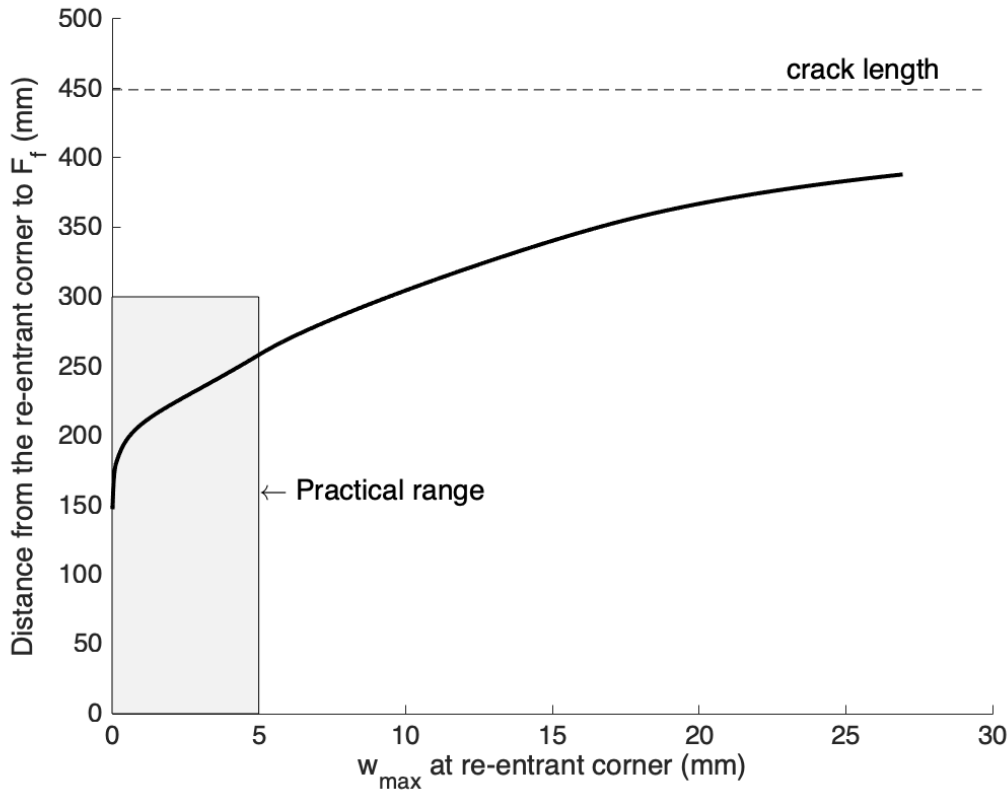
Figure 4.7: Evolution of the distance between the re-entrant corner to the position of the resulting tensile force due to the fibers according to the crack width at the re-entrant corner

In addition to the forces due to the concrete in compression and the fibers across the crack, the forces in each reinforcement are assessed exactly in the same way as in the previous chapter by using a mechanical model between the crack width w and the tensile stress σ_t in the rebars proposed by Sigrist, see equations (9) to (11). Once all the forces acting on the free body diagram of the dapped-end are assessed, a horizontal equilibrium is solved to define the depth of the compression zone x:

$$\sum_i F_{h,i} + \sum_i F_{d,i} \cos \beta + F_f \sin \theta - H = F_{CDZ} + F_{c0} + F_{rf,CZ} \tag{30}$$

By using the value of the depth of the compression zone, the support shear at failure V_{pred} can be predicted by solving the moment equilibrium around the tip of the crack and considering that the peak

resistance appears for a strain at the top surface of the concrete compression zone equals to 0.0035 :

$$
\begin{aligned}
V_{\text{pred}} = \frac{1}{(a + l_{cr}\cos\theta)} \Big\{ &\sum F_{h,i}\left(h - x - c_{h,i}\right) \\
&+ \sum F_{v,i}\left(l_{cr}\cos\theta - c_{v,i}\right) + \sum F_{d,i}\cos\beta\sin\theta\left(l_{cr} - c_{d,i}\right) \\
&+ \sum F_{d,i}\sin\beta\cos\theta\left(l_{cr} - c_{d,i}\right) + F_{c0}\frac{2}{3}\left(x - d_{CDZ}\right) \\
&+ F_{CDZ}\left(x - 0.5d_{CDZ}\right) - H\left(l_{cr}\sin\theta\right) \\
&+ F_{rf,CZ}\left(x - c_{rf,CZ}\right) + F_f \times d \Big\}
\end{aligned}
\tag{31}
$$

where a is the span of the dapped-end, $c_{h,i}$, $c_{v,i}$ and $c_{d,i}$ the distances from the re-entrant corner respectively to an horizontal, vertical and diagonal reinforcement i, $c_{rf,CZ}$ is the concrete cover of the reinforcement in the compression zone, β is the angle of inclination of the diagonal reinforcement with the horizontal axis, d is the distance between the tip of the crack and the resulting tensile force due to the fibers across the crack.

4.1.2 Flowchart of the solution procedure

The flowchart of FIGURE 3.3 is extended to FIGURE 4.8 by considering the effect of steel fibers. An iterative procedure is again applied to solve the problem, the concrete under compression is governed by a new constitutive law and the fibers crossing the crack bring a new tensile contribution to the dapped-end connection. These modifications are shown in orange in the flowchart.
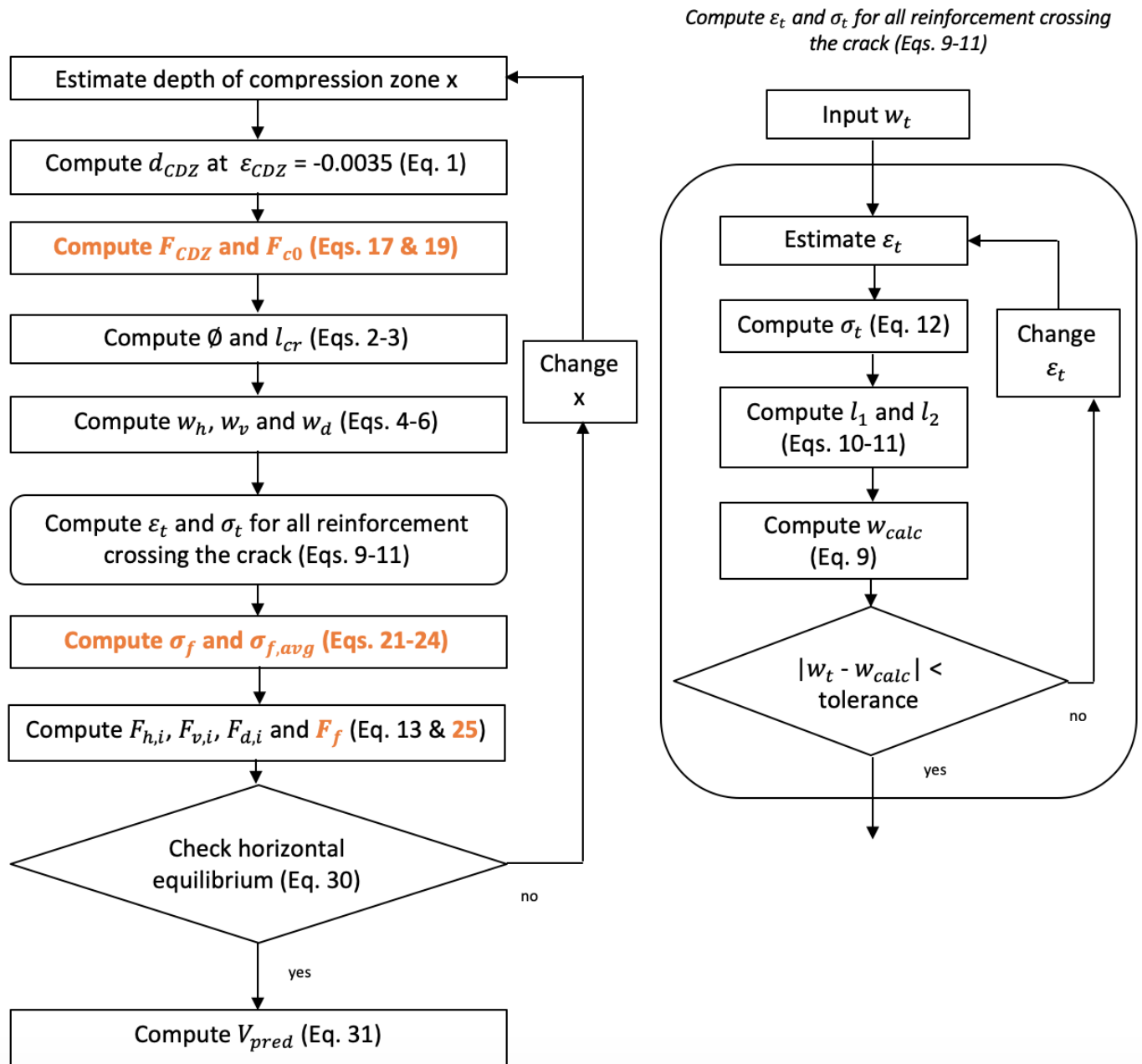
Figure 4.8: Simplified approach - Procedure of the kinematic model applied to FRC dapped-end connections

4.2 Complete behavior

Although the simplified approach presents promising results, it only consists in a prediction of the peak resistance of the dapped-end connection governed by flexural failure. Now, the study focuses on the complete behavior of the dapped-end whose peak resistance is not especially reached for a value of $\varepsilon_{top} = 0.0035$ corresponding to the strain assumed to reach the flexural capacity by concrete crushing. The complete behavior analysis studies the evolution of the crack width along the main inclined crack by varying the strain at the top surface of the concrete from zero to a certain value of the strain greater than 0.0035 (say until $\varepsilon_{top} = 0.0055$). There is no point in going too high in the strain values because this would never happen in reality, even if the model would propose a numerical response. In FIGURE 4.2, as the strain ε increases, the curve first increases up to a peak (assessed at $\varepsilon = \varepsilon_{c1}$) and then decreases slowly. In the simplified approach the flexural capacity is just predicted for a strain equals to 0.0035. However, the complete behavior studies the evolution of the strain and is divided in two sequences: before the formation of the CDZ ($\varepsilon_{top} \in [0; \varepsilon_{c1}]$) and after the formation of the CDZ ($\varepsilon_{top} > \varepsilon_{c1}$).

For each sequence, the geometrical and kinematic parameters of the dapped-end are re-evaluated. Some parameters are assumed constant while others are determined via models and relationships that differ according to the sequence. The first parameter to assess is the length of the compression undamage zone based on the length of the CDZ. Although the relative rotation ϕ is assessed by using only the length of the CDZ in the simplified approach, this relative rotation has to consider the impact of the compression undamage zone in order to be more realistic. It is necessary to know the length of this zone to determine the relative rotation of the two rigid blocks around the tip of the crack, see FIGURE 4.11. The length of the CDZ is evaluated by considering planes inclined of an angle α, see equation (2). In addition to the CDZ, this relative rotation should actually take into account the compression undamage zone that also has a deformation and therefore has an impact on the relative rotation. Based on the simplified approach for $\varepsilon_{top} = 0.0035$, the length of the compression undamage zone is assessed by solving the following system of equations according to the strain distribution along the compression zone:

$$\begin{cases} \phi x = l_{dmg} \cdot \varepsilon_{top} \\ \phi d_{undmg} = l_{undmg} \cdot \varepsilon_{c1} \end{cases} \tag{32}$$

$$\Longleftrightarrow \begin{cases} \phi = \frac{l_{dmg} \cdot \varepsilon_{top}}{x} \\ \frac{l_{dmg} \cdot \varepsilon_{max}}{x} d_{undmg} = l_{undmg} \cdot \varepsilon_{c1} \end{cases} \tag{33}$$

If the second equation is simplified, it comes:

$$\Longleftrightarrow l_{dmg} \cdot d_{undmg} = x \cdot \frac{\varepsilon_{c1}}{\varepsilon_{max}} \cdot l_{undmg}$$

$$l_{dmg} \cdot d_{undmg} = d_{undmg} \cdot l_{undmg}$$

$$l_{dmg} = l_{undmg} \tag{34}$$

The length of the compression undamage zone (l_{undmg}) is assumed equal to the length of the CDZ (l_{dmg}) for $\varepsilon_{top} = 0.0035$ and constant while the ε_{top} is varying. Consequently the contribution of l_{undmg} is neglected in the simplified approach because it is function of the opening angle of the crack ϕ which

should depend on the length of the undamage zone, so an initial value is taken based on l_{dmg}.

Knowing that $l_{undmg} = l_{dmg}$ for $\varepsilon_{top} = 0.0035$, l_{dmg} is first determined from equation (35):

$$l_{dmg} = \frac{d_{dmg}}{0.5 \tan \alpha} \tag{35}$$

where α is the angle between the inclined plane and the horizontal axis that bound the CDZ. Firstly assumed at 50° in the simplified approach, the angle α takes another value which will be explained subsequently.

The basic kinematic model used a bond stress between the rebar and the concrete from REFER-ENCE [16]. In order to study the complete behavior and to predict the crack width of the main crack, Mata Falcón suggests to divide the bond stress basically used by factor 2-2.5, see REFERENCE [15]. For a given half bond stress, the angle α has also to be lowered to model as well as possible the complete behavior of the dapped-end. Furthermore, it also will be seen that it is more realistic to decrease this angle. Consequently, it results in the following bond stresses:

$$\tau_{b1} = \frac{0.3 \left(f_c'\right)^{2/3}}{2} \tag{36}$$

$$\tau_{b2} = 2\tau_{b1} \tag{37}$$

where τ_{b1} and τ_{b2} are the bond stresses used for the straight part and the hooked-end part of the fiber respectively. These equations apply to ribbed rebars. In the case of smooth rebars, $\tau_{b1} = \tau_{b2}$.

The stress through each reinforcement is assessed in the same way as the method explained in the simplified approach for the relationship between crack width measured at a reinforcement and the corresponding stress, see equations (9) to (11).

In each phase of the dapped-end behavior, the calculation methods in the reinforcements do not vary, also the tensile stress in the fibers. However, the kinematic and geometrical parameters in the compression zone differ according to the strain at the top surface of the concrete. FIGURE 4.9 shows the evolution of the stress distribution according to the different phases of the dapped-end behavior.
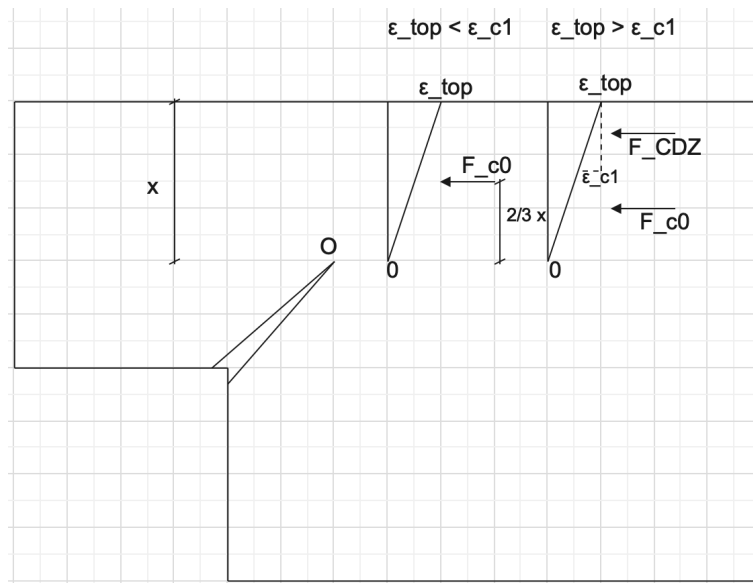
Figure 4.9: Strain distribution in the compression zone for each sequence of the complete behavior

4.2.1 Behavior of the dapped-end before formation of the CDZ

In this first phase of the behavior, the dapped-end is studied by varying the strain ε_{top} from 0 to the strain corresponding to the peak of the stress-strain curve, see FIGURE 4.2. As the curve only increases linearly with the strain, the concrete has not yet reached its compressive strength f'_c and therefore no compression damage zone has been formed yet. Consequently, the compression undamage zone corresponds to the whole compression zone:

$$d_{undmg} = x \tag{38}$$

Once l_{undmg} has been assessed for ε_{top} = 0.0035 with the simplified method as a constant value for the complete behavior and knowing that the strain is still inferior to the corresponding strain at peak ε_{c1}, the relative rotation ϕ of the two rigid blocks around the tip of the crack is evaluated from equation (39) according to FIGURE 4.10.

$$\phi = \frac{\varepsilon_{top} \cdot l_{undmg}}{2 \cdot d_{undmg}} \tag{39}$$
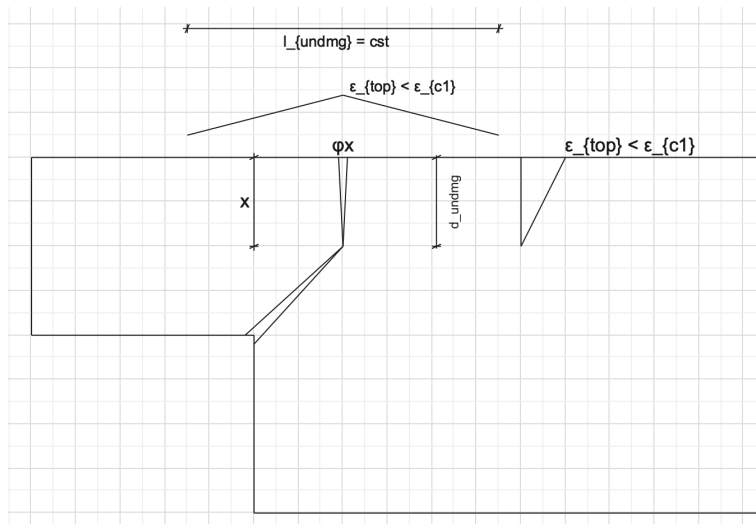
Figure 4.10: Kinematic parameters details in the compression for $\varepsilon \in [0; \varepsilon_{c1}]$

The stress in the compression zone is simply assessed from the constitutive law proposed by Ezeldin from equation (2.2). The resulting force in the compression zone F_{c0} is evaluated based on the stress-strain curve between 0 and ε_{top} by calculating the area under the curve and divide by ε_{top}. The level arm of this resulting force is positioned at 2/3 x (by assumption that the stress-stress curve increases linearly until the peak) to the tip of the crack in the conditions of a moment equilibrium around this point as in equation (40).

$$
\begin{aligned}
V_{\text{pred}} = \frac{1}{(a + l_{cr}\cos\theta)} \Big\{ & \sum F_{h,i} \left(h - x - c_{h,i} \right) \\
& + \sum F_{v,i} \left(l_{cr}\cos\theta - c_{v,i} \right) + \sum F_{d,i}\cos\beta\sin\theta \left(l_{cr} - c_{d,i} \right) \\
& + \sum F_{d,i}\sin\beta\cos\theta \left(l_{cr} - c_{d,i} \right) + F_{c0}\left(\frac{2x}{3} \right) \\
& - H \left(l_{cr}\sin\theta \right) + F_{rf,CZ}\left(x - c_{rf,CZ} \right) + F_f \times d \Big\}
\end{aligned}
\tag{40}
$$

4.2.2 Behavior of the dapped-end after formation of the CDZ

In this second phase, the behavior is studied for a strain at the top higher than ε_{c1}, ε_{c1} not included. In the compression zone, the strain along the depth of the compression zone varies linearly from 0 (at the tip of the crack) to ε_{top} (greater than ε_{c1}) at the top surface of the concrete, see FIGURE 4.11. The part between $\varepsilon = 0$ and ε_{c1} represents the compression undamage zone while the part above (from ε_{c1} to ε_{top}) corresponds to the CDZ. The depths of the compression damage and undamage zones are respectively defined as:

$$d_{dmg} = x \left(1 - \frac{\varepsilon_{c1}}{\varepsilon_{top}} \right) \tag{41}$$

$$d_{undmg} = x - d_{dmg} \tag{42}$$
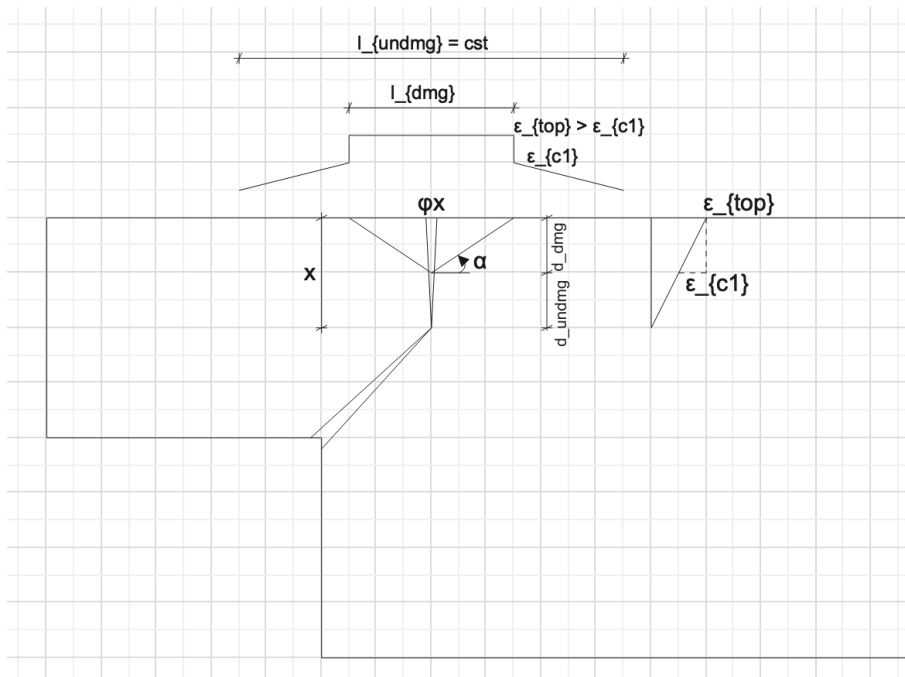
Figure 4.11: Kinematic parameters details in the compression zone for $\varepsilon \in \left]\varepsilon_{c1}; 0.0035\right[$

The length of the CDZ is obtained from equation (43) by using the depth of the CDZ and the two inclined planes of an angle α while the relative rotation ϕ from equation (44):

$$l_{dmg} = \frac{2 \cdot d_{dmg}}{\tan \alpha} \tag{43}$$

$$\phi = \frac{\varepsilon_{top} \cdot l_{dmg} + \varepsilon_{c1} \frac{\left(l_{undmg} - l_{dmg}\right)}{2}}{x} \tag{44}$$

where l_{undmg} is constant.

The resulting forces in the compression damage and undamage zones are respectively defined as:

$$F_{CDZ} = \sigma_{CDZ} d_{CDZ} b \tag{45}$$

$$F_{c0} = \sigma_{cf,avg}\left(x - d_{CDZ}\right) b \tag{46}$$

where $\sigma_{cf,avg}$ is assessed by equation (18) by assuming a parabolic stress-strain curve and σ_{CDZ} is the stress (assumed constant within the CDZ) obtained based on the constitutive law proposed by Ezeldin et al. Once the horizontal equilibrium is solved to determine the depth of the compression zone x, it results as the following moment equilibrium:

$$
\begin{aligned}
V_{\text{pred}} = \frac{1}{(a + l_{cr}\cos\theta)} \Big\{ &\sum F_{h,i}\left(h - x - c_{h,i}\right) \\
&+ \sum F_{v,i}\left(l_{cr}\cos\theta - c_{v,i}\right) + \sum F_{d,i}\cos\beta\sin\theta\left(l_{cr} - c_{d,i}\right) \\
&+ \sum F_{d,i}\sin\beta\cos\theta\left(l_{cr} - c_{d,i}\right) + F_{c0}\left(\frac{2\left(x - d_{CDZ}\right)}{3}\right) \\
&+ F_{CDZ}\left(x - 0.5 d_{CDZ}\right) - H\left(l_{cr}\sin\theta\right) \\
&+ F_{rf,CZ}\left(x - c_{rf,CZ}\right) + F_f \times d \Big\}
\end{aligned}
\tag{47}
$$

where a is the span of the dapped-end, $c_{h,i}$, $c_{v,i}$ and $c_{d,i}$ the distances from the re-entrant corner respectively to an horizontal, vertical and diagonal reinforcement i, $c_{rf,CZ}$ is the concrete cover of the reinforcement in the compression zone, β is the angle of inclination of the diagonal reinforcement with the horizontal axis, d is the distance between the tip of the crack and the resulting tensile force due to the fibers across the crack.

4.2.3 Flowchart of the solution procedure

The flowchart shown in FIGURE 4.12 presents the solution procedure to study the complete behavior of the dapped-end. Overall, the iterative procedure is similar to that of the simplified approach but the support reaction is calculated by varying the strain in the compression zone. The modifications made are shown in blue in the flowchart.
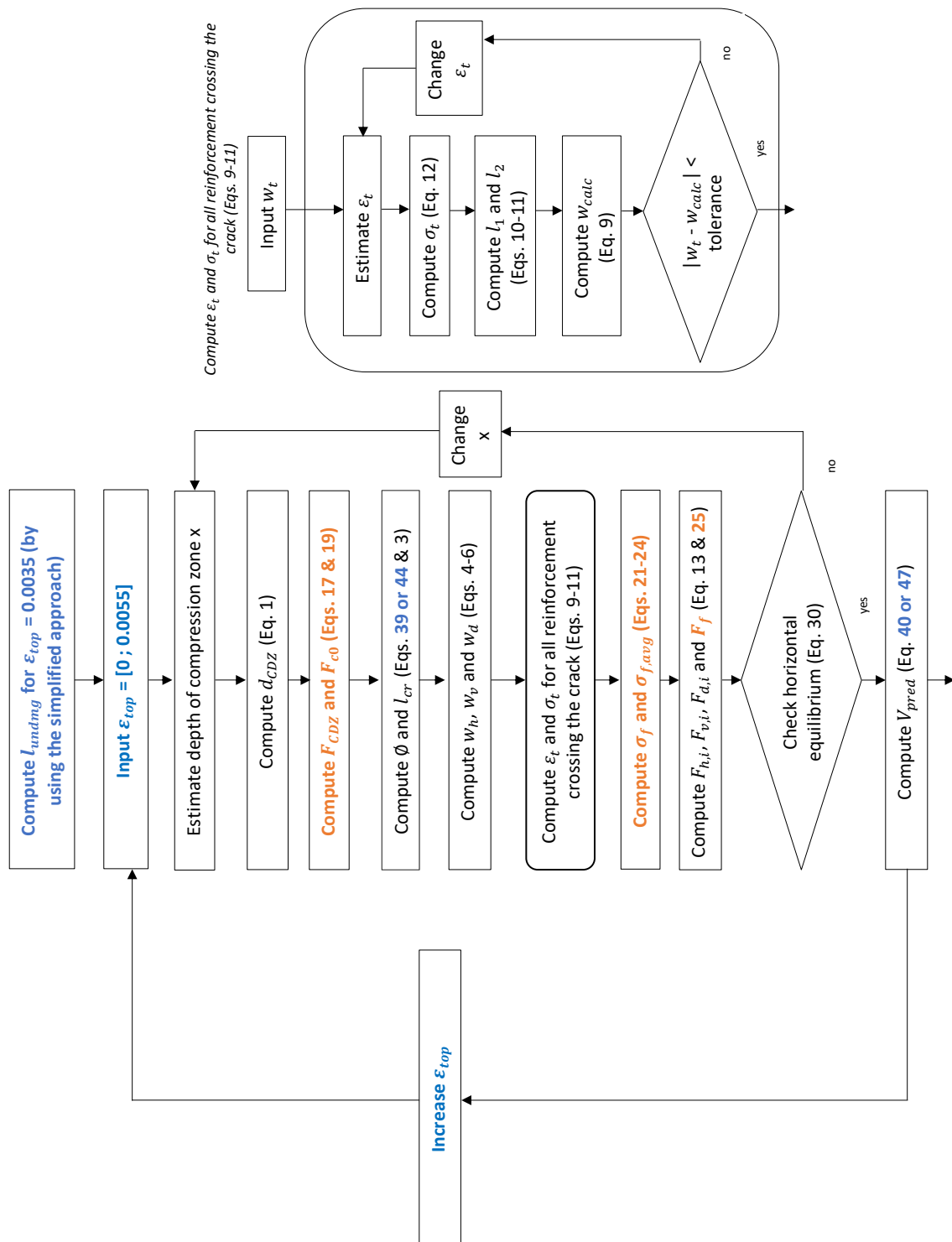
Figure 4.12: Complete behavior - Procedure of the kinematic model applied to FRC dapped-end connections

5 Comparisons with tests

The kinematic model predicts the flexural capacity of a dapped-end connection by using to the measured inclination of the crack from the re-entrant corner with the horizontal axis. The model is now compared to a set of experimental tests taken from 5 different papers, see the database in the appendix. Out of a total of 30 experimental tests performed with FRC, 17 of them present a flexural failure mode. 10 other ones do not give any information about the failure mode, a flexural failure is assumed. The data of each test are detailed in the database in the appendix and includes fiber volume ratio, the experimental support shear at failure, the predicted peak capacity via the model and the experimental-to-predicted ratio. The dapped-end depth d varies from 100 to 300 mm and the shear span-to-depth ratio a/d from 0.27 to 1.36 while the compressive strength of the concrete varies from 29 to 49 MPa.

The experimental results are compared according to the two different approaches modeled: the simplified approach considering a peak resistance for a compression concrete strain assumed at 0.0035 and the complete behavior by increasing the strain at the top surface of the dapped-end (located in the compression zone) from 0 to 0.0055. Some specimens still do not reach their peak resistance for a strain equals to 0.0055 but it is not realistic to go beyond this value.

5.1 Simplified approach for peak response

The simplified approach consists in predicting the peak resistance of the dapped-end by assuming a flexural failure reached for a strain ε_{top} in the compression damage zone equals to 0.0035. This method is aimed at assessing the flexural failure governed by an inclined crack from the re-entrant corner. The assessment is made by measuring the angle of inclination of the main crack on existing structures and using this value as an input, although it is sometimes hard to measure correctly this value.

At first, the model can be compared to the experimental capacities by defining the peak resistance experimental-to-predicted ratio $\frac{V_{exp}}{V_p}$. This ratio is aimed at reaching the unit which means that the model predicts perfectly the same peak resistance as the experimental results. If the ratio is higher than 1, the model is conservative. If the model predicts a higher value than what occurs in reality, it is then considered unconservative. The strength experimental-to-predicted ratio gives a result based on 27 tested specimens of an experimental value V_{exp} equals to a minimum value of 0.8 V_p and a maximum value of 1.25 V_p, which are values obtained according to the papers [13] and [24] in which a great number of assumptions have been made and which certainly induce errors. The coefficient of variation and the average equal to respectively 14.91% and 1.05 which is conservative.

FIGURE 5.1 represents the strength experimental-to-predicted ratio $\frac{V_{exp}}{V_p}$ according to the span-to-depth ratio a/d. The span-to-depth ratio varies between 0.27 and 1.36 according to the specimen considered. There is no apparent bias with respect to a/d ratio although a higher a/d ratio seems to give more conservative results.
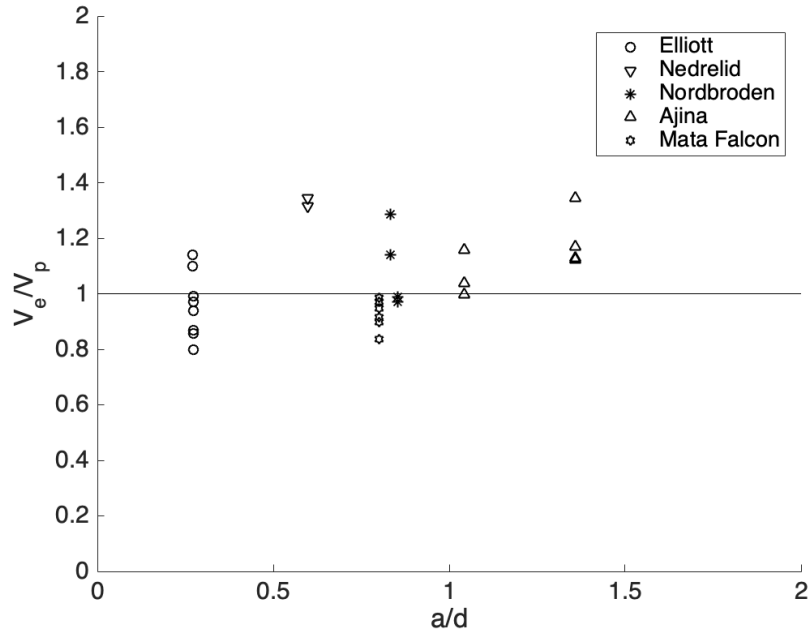
Figure 5.1: Experimental-to-predicted ratio according to the span-to-depth ratio a/d

The flexural capacity is calculated by solving a moment equilibrium, see equation (47). All the moment applied by the forces acting on the dapped-end and their level arm are divided by the level arm $a+l_{cr}\cos\theta$ of the support shear of the dapped-end around the tip of the crack. For a given specimen, as the distance from the support reaction to the full depth increases, the faster the peak resistance will be reached, see FIGURE 5.2. As well experimental results as predictions show this which means that the model follows the behavior of the experimental dapped-end.
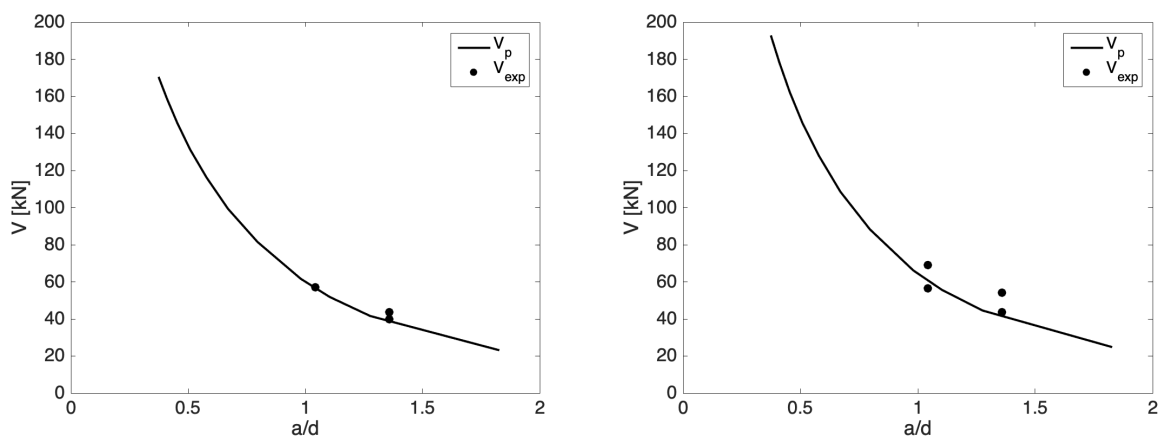
Figure 5.2: Flexural capacity (experimental and predicted) according to the span-to-depth ratio a/d for specimens from Ajina (respectively 0.8% and 1.2% by volume ratio)

FIGURE 5.3 shows that the inclined crack appears for a range angle between 30° and 62°. However, to measure the angle of the inclination of the crack from the re-entrant corner on existing structures is quite difficult. This model assumes a straight crack from the re-entrant corner to the tip of the crack but it never happens in reality. The crack usually propagates in a non-linear way and other micro-cracks appear in localized areas of the main crack. These changes in direction may be related

to the arrangement of the reinforcement, imperfections or other factors. Moreover, the angle of inclination of the main crack can be different from one side to another side of the dapped-end, of course not too different but enough to cast doubt. A crack may start with a small angle of inclination and then may straighten and change direction again. In this case, it is difficult to measure an exact angle and although the desire to be as objective and accurate as possible is present, an order of magnitude is usually used. On a set of 27 specimens tested, the angle of inclination of the crack is between 30° and 62°. Errors can be induced in the measurement of the angle or if a procedure of design and not of assessment of failure governed by a crack from the re-entrant corner is considered, it is interesting to study the angle that minimizes the error. In this case, an angle has to be chosen to predict correctly the results in best average peak resistance experimental-to-predicted ratio and least coefficient of variation between the model and the experimental results.
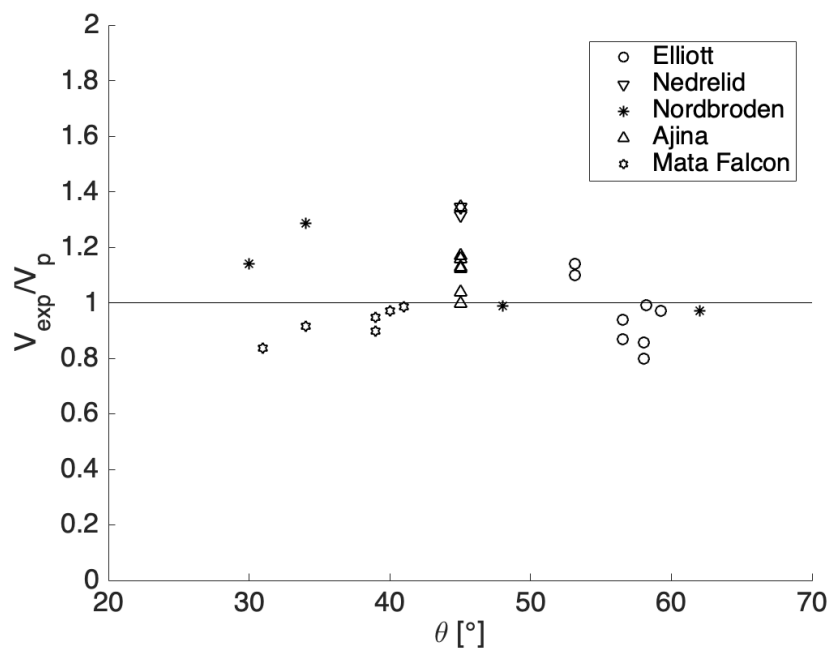
Figure 5.3: Experimental-to-predicted ratio according to the inclined angle θ of the crack

In FIGURE 5.4, four pictures of an experimental specimen are shown, three of them represent the crack at the peak resistance and the last of four the dapped-end at the ultimate load. On one side of the dapped-end to the other side, the crack looks to propagate on a different way. Moreover, the first picture (top left diagram) presents a crack which starts with a low angle of inclination, then the angle increases and two mains cracks appear. It is difficult to know which angle has to be taken into account, the first one or the second higher one and it might introduce errors to the model and results to a bad peak resistance. Consequently, the model will modify the level arm, the compression zone will be badly assessed, and the flexural capacity will be wrong.

Furthermore, FIGURE 5.3 shows that as the measured angle moves away from a median value (around 45°), the model becomes more unconservative. As Chathura et al. demonstrate in their paper, the model works well for an accurate measured angle but an angle of 45° has to be assumed once it is impossible to measure informations on existing structures, see REFERENCE [29]. In TABLE 5.1, the coefficients of variation and the average strength experimental-to-predicted ratio of the different tests and according to scientific papers found are given for an experimental measured inclination angle of the crack and an assumption for $\theta = 45°$. In most cases, the results show a slightly lower coefficient
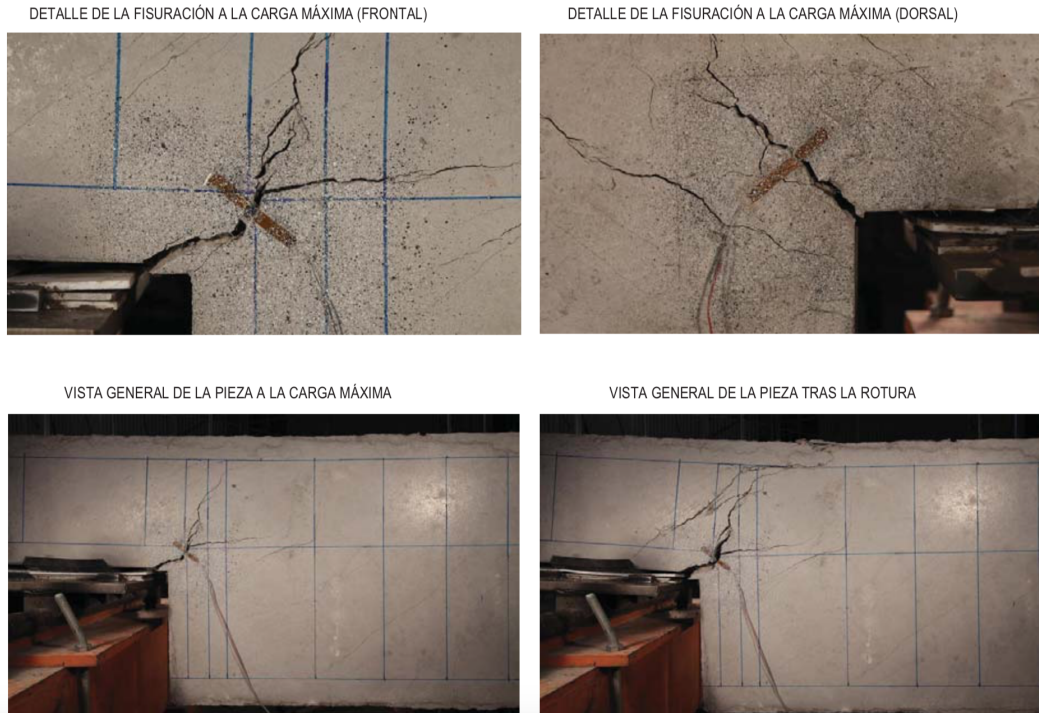
Figure 5.4: Crack patterns observed in specimen DEB-3.8-T2 [15]

of variation and a slightly higher average. Using a value of 45° for the angle of the inclination of the crack while trying to minimize the error or not knowing what angle to take is conservative. An angle of 45° will be used for each specimen in the following study.

TABLE 5.1 assesses the coefficient of variation and the average strength experimental-to-predicted ratio of the tests performed for each paper. The validity of each paper can be determined according to their results. It can be seen that as the number of assumptions had to be made, the predictions are far from experimental values and the coefficient of variation results to be bad. In contrast to that, the study done by Mata Falcón reports all the necessary input parameters for the kinematic model. Consequently the coefficient of variation is very good and the average very close to the unit which means that the tests from this paper are representative of the model. The dimensions of the specimens performed by Mata Falcón are large which reduces errors and the CoV = 2.71% proves it.

	θ_{exp}		$\theta = 45°$	
	CoV [%]	Avg	CoV [%]	Avg
All specimens (27 tests)	14.9	1.045	13.61	1.069
Nordbroden/Ajina/Mata Falcón (17 tests)	13.2	1.053	11.65	1.094
Ajina/Mata Falcón (13 tests)	13.41	1.039	10.29	1.07
Elliott (8 tests)	12.35	0.958	7.13	0.951
Nedrelid (2 tests)	1.557	1.33	1.557	1.33
Nordbroden (4 tests)	13.49	1.096	14.04	1.174
Ajina (7 tests)	9.77	1.137	9.77	1.137
Mata Falcón (6 tests)	5.87	0.925	2.71	0.992

Table 5.1: Comparison between the coefficient of variation and the average flexural capacity experimental-to-predicted ratio for an inclination angle θ_{exp} measured on existing structures and θ assumed at 45°

In addition to the impact of the span on the flexural capacity of the dapped-end, the peak response can be studied according to the fiber volume ratio, see FIGURE 5.5. The plots below represent the evolution of the support reaction with the fiber volume ratio. Concrete usually has a bad tensile strength whereas fiber-reinforced concrete enhances its tensile behavior. Fibers within the concrete along the main inclined crack contribute in a resulting tensile force. This force acting on the crack is based on equation (21) whose tensile strength of the fibers is the contributions of the straight and hooked-end parts of the fiber. Each contribution depends on the fiber volume ratio ρ_f within the concrete. Therefore, as the fiber volume ratio increases, the force due to the fibers will be greater and the flexural capacity will be greater. As shown in FIGURE 5.5 below, for the same specimen where simply the amount of fibers is increased, the peak strength will be directly increased. This is illustrated for both experimental and predicted values.
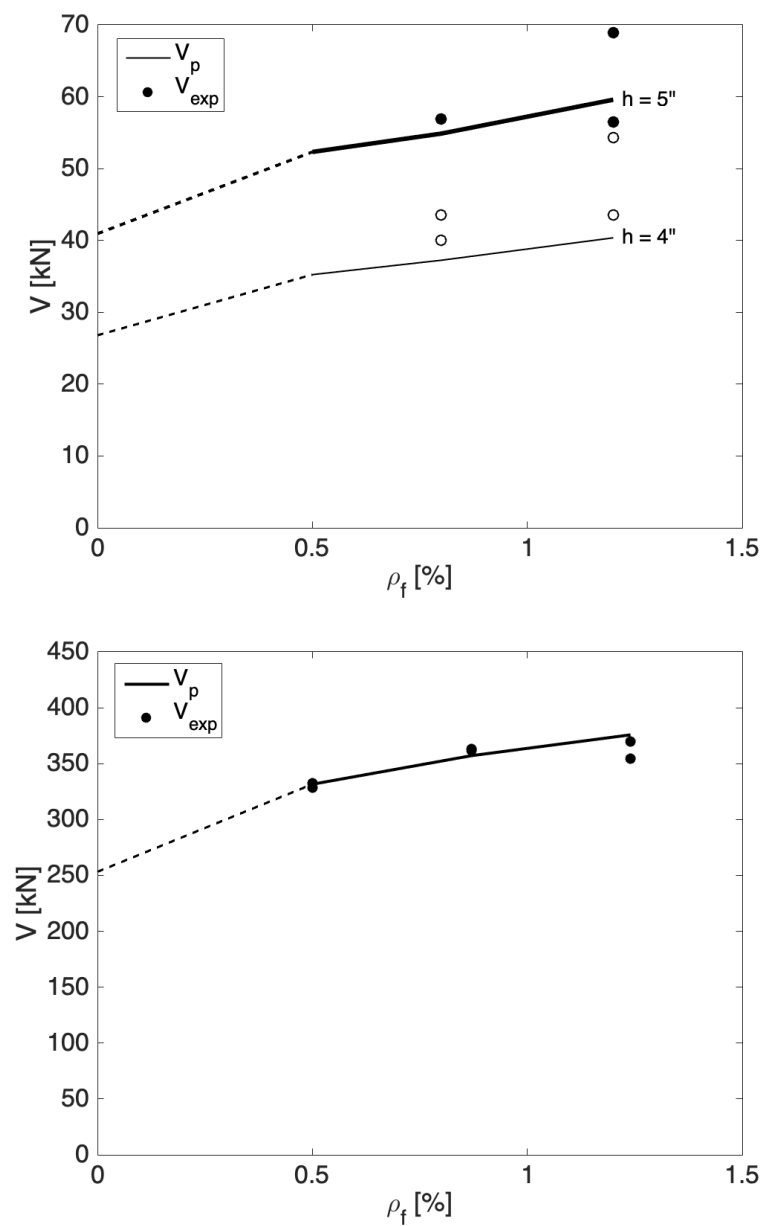
Figure 5.5: Flexural capacity (experimental and predicted) according to the fiber volume ratio for specimens from Ajina and Mata Falcón respectively

FIGURE 5.6 shows the contribution of each element of the dapped-end while the amount of fibers is increasing. The contribution of each element are quite similar as the amount of fibers increases. However, there is a discontinuity for $\rho_f = 0.5\%$. At first, an important discontinuity appears for a small amount of fibers. On simply RC structures, the tensile force of the concrete is neglected but when fibers are added, the model considers a new contribution which is directly important to the flexural capacity. The contribution of the reinforcement decreases slowly. In order to be realistic, the contribution of the steel reinforcement should be constant with the fiber volume ratio. However, the kinematic model uses a horizontal equilibrium to define the depth of the compression zone, so the level arms of the resulting forces acting on the dapped-end are modified and the contribution is a bit modified. The capacity due to the concrete under compression especially located in the CDZ increases due to the better post-peak behavior of FRC. If the evolution of the peak resistance according to the fiber volume ratio is studied only with FRC, the diagram illustrates the contribution of each element almost as a constant. The contribution of the reinforcement in compression is included in the contribution of the compression zone V_c. Furthermore, the contribution of the fibers naturally increases on a linear way with the fiber volume ratio.
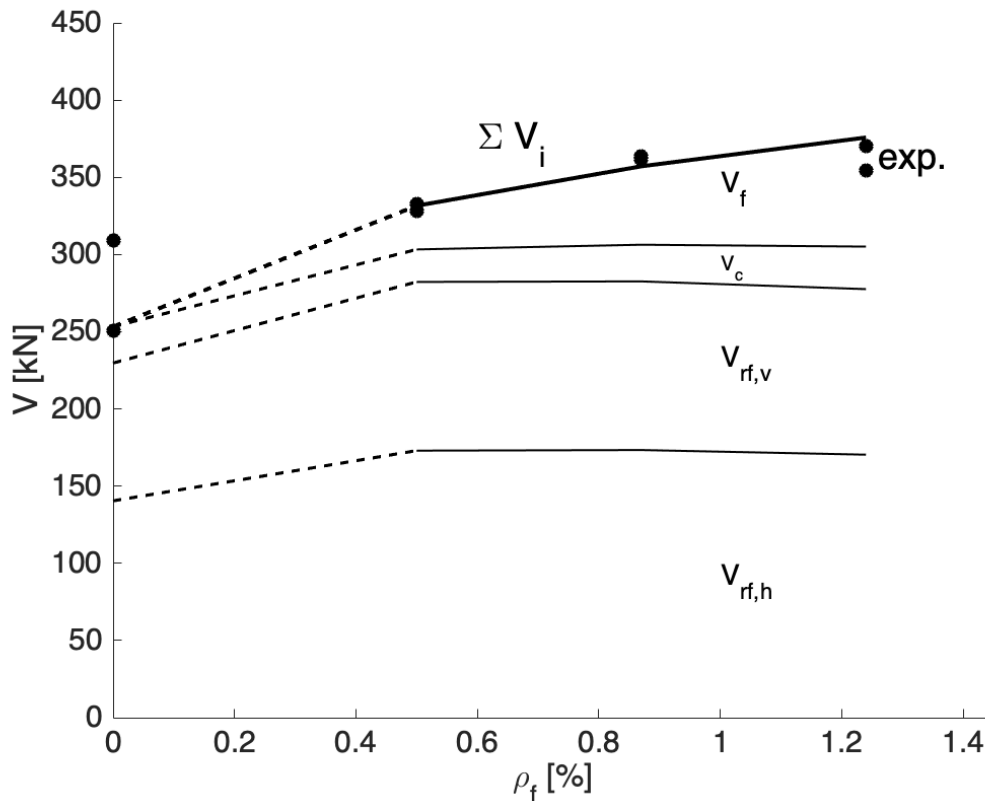
Figure 5.6: Contribution of each element according to the fiber volume ratio for specimens from Mata Falcón

FIGURE 5.6 shows a significant impact of the addition of fibers in the concrete on the flexural capacity of the dapped-end. For a small fiber volume ratio, the flexural capacity increases very quickly. This considerable increase is due to the experimental data. Indeed, the compressive concrete strengths used to compare experimental results are really different from an experimental test with fibers or without, from 31.1 MPa to around 46 MPa (45.5, 48.8 & 48.4) corresponding respectively to simply RC or FRC. The different concrete mix proportions explain why the capacity increases more slowly as the

fiber volume ratio continues to increase. The kinematic model predicts an increase of more than 30% for a fiber volume ratio of only 0.5% while when 0.37% of additional fiber volume ratio is added, the flexural capacity increases by only 7.8% and the capacity tends to a linear way. The experimental results agree with this analysis: a low fiber volume ratio increases the flexural capacity rapidly while the flexural capacities for 0.87% and 1.24% fiber volume ratios are almost similar.

The fiber aspect ratio $\frac{l_f}{d_f}$ is an important factor that impacts the tensile stress in the fibers. There is a large choice of fibers in the world, of different shape, length, diameter, if they are smooth or ribbed, in steel or polymer,... A fiber is usually defined as X/Y, where X represents the fiber aspect ratio and Y the length of the fiber. Comparing different types of *Dramix* hooked-end fibers from the BEKAERT company (see REFERENCES [6], [7], [8], [9] & [10]), FIGURE 5.7 shows the impact of the fiber geometry on the flexural capacity of a dapped-end. Directly, it comes that the more the fiber aspect ratio increases, the more the flexural strength increases. The stress in the fibers are proportional to the aspect ratio $\frac{l_f}{d_f}$. As the length of the fiber increases, the bond stress will be greater and will have a direct impact to the peak strength. On the other hand, for the same fiber length, the smaller the fiber diameter, the smaller the circumference and the smaller the bond stress, see RELATIONSHIP 48. In reality, for a given fiber volume ratio ρ_f, the more the fiber diameter decreases and the more the number of fibers increases, which results in a higher specific surface of fibers and consequently a higher flexural strength of the dapped-end. In technical files from the fibers DRAMIX 55/60 and 80/60 (same fiber length, different diameter), there are respectively 2392 fibers/kg and 4690 fibers/kg.

$$\begin{cases} \text{fiber volume} \sim d_f^2 \\ \text{fiber surface} \sim d_f \end{cases} \tag{48}$$
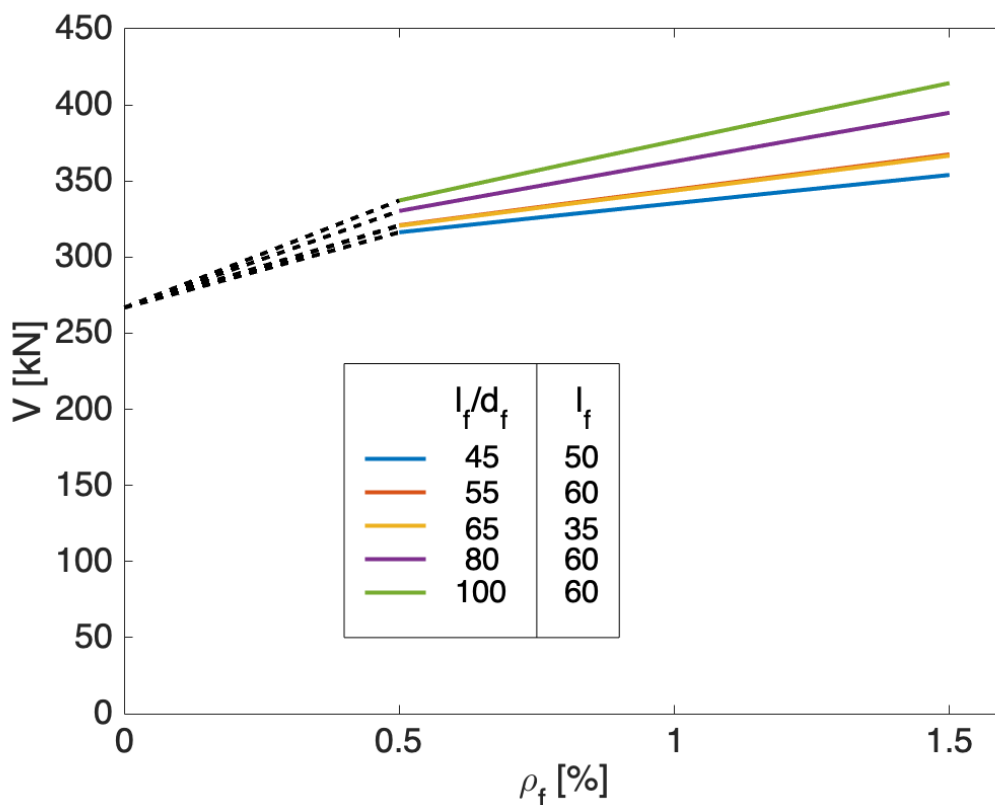
Figure 5.7: Impact of the fibers according to the aspect ratio

The attached database in the appendix shows the flexural capacity of each specimen and evaluates the experimental-to-predicted ratio. The coefficient of variation is also indicated and a coefficient of variation is more favorable assuming $\theta = 45°$. However, some values are shown in parentheses, which means that the failure mode does not apply to the model developed in this study. According to the pictures provided by Ajina, some failure modes are obtained by shear failure while other pictures do not allow to identify the failure mode (noted by "DK" in the database). Considering all the specimens tested by Ajina, the CoV and average are 9.19% and 1.11 respectively while considering only the specimens whose failure mode is a flexural failure, they were respectively 9.76% and 1.13. The simplified approach presents similar results whatever the failure mode and this model would be conservative whatever the failure mode.

5.2 Complete behavior

Failure does not necessarily occur for a compressive strain value $\varepsilon_{top} = 0.0035$ to reach concrete crushing, the strain usually exceeds this value in reality. A range of strain varying from 0 to 0.0055 is applied to the kinematic model to study the complete behavior. This allows to observe the support shear curve by increasing the strain at the top of the compression zone. Then, a peak resistance is reached for a certain strain corresponding to the flexural capacity of the dapped-end.

In parallel to the simplified approach, it is very complicated on some existing structures to measure the angle of inclination of the crack θ. While some cracks propagate almost straight, others change direction roughly as their crack width is increasing. For this purpose, the coefficients of variation and the averages of the strength experimental-to-predicted failure respectively for an angle θ measured on the specimens and another assumed at 45° are compared. The angle $\theta = 45°$ will be used for the comparative studies to minimize errors and inaccuracies, which is in line with the analysis of Rajapakse et al. In addition, it decreases the coefficient of variation and slightly increases the average closer to unity, see TABLE 5.2.

	θ_{exp}		$\theta = 45°$	
	CoV [%]	Avg	CoV [%]	Avg
All specimens (27 tests)	13.25	0.957	11.13	0.975
Nordbroden/Ajina/Mata Falcón (17 tests)	13.12	0.933	12.18	0.957
Ajina/Mata Falcón (13 tests)	7.99	0.925	7.17	0.938
Elliott (8 tests)	12.96	0.963	7.44	0.975
Nedrelid (2 tests)	0.284	1.128	0.284	1.128
Nordbroden (4 tests)	24.8	0.961	21.4	1.019
Ajina (7 tests)	9.60	0.949	9.60	0.949
Mata Falcón (6 tests)	4.22	0.897	2.62	0.926

Table 5.2: Comparison between the coefficient of variation and the average flexural capacity experimental-to-predicted ratio for an inclination angle θ_{exp} measured on existing structures and θ assumed at 45°

In the simplified approach, the bond stress between the reinforcement and the concrete was assumed for a value taken from REFERENCE [16] and the model gives good results. The complete behavior is aimed at studying the evolution of the crack width. Mata Falcón suggests to take a bond stress divided by 2-2.5 to be more realistic. Once a half bond stress is fixed, another parameter which had to be assumed is α the angle to determine the CDZ. This one is assumed at 50° in the RC kinematic model by optimizing the results in terms of experimental-to-predicted ratio and the coefficient of variation. Furthermore, the simplified FRC kinematic model used also $\alpha = 50°$ and the results were still promising. FIGURE 5.8 shows the experimental crack width (at the re-entrant corner) measured on different specimens and their comparison with the predicted crack width for different α. The prediction does not follow exactly the experimental but it can be seen that as α is lowered, the crack width increases more rapidly. For a given strain, the support reaction is smaller as α is high but the curves for different values of α follow the same way. It means that if the strain tends to infinity the flexural capacity is the same whatever the angle α. However, the complete behavior is studied up to $\varepsilon_{top} = 0.0055$, it is difficult to know if the compression strain on existing structures goes up to more than 0.0055 or less than this value, so the model assumes $\varepsilon_{top} = 0.0055$ as the maximum value. In terms of predicted crack width, an $\alpha = 20$-25° looks to predict well the ultimate crack width and
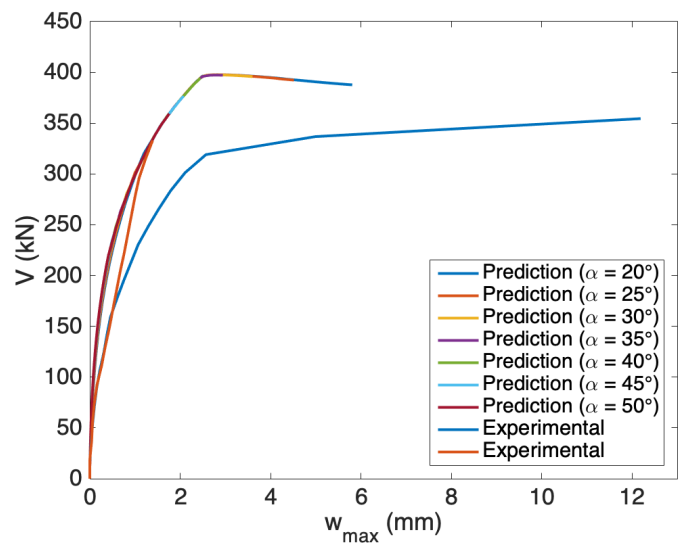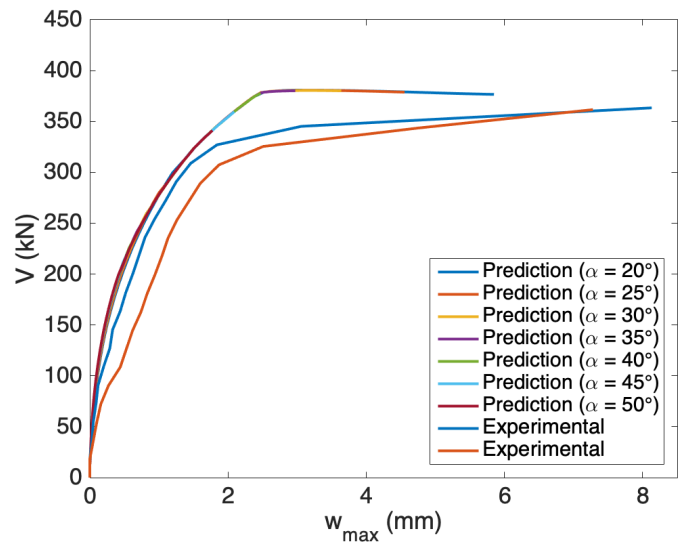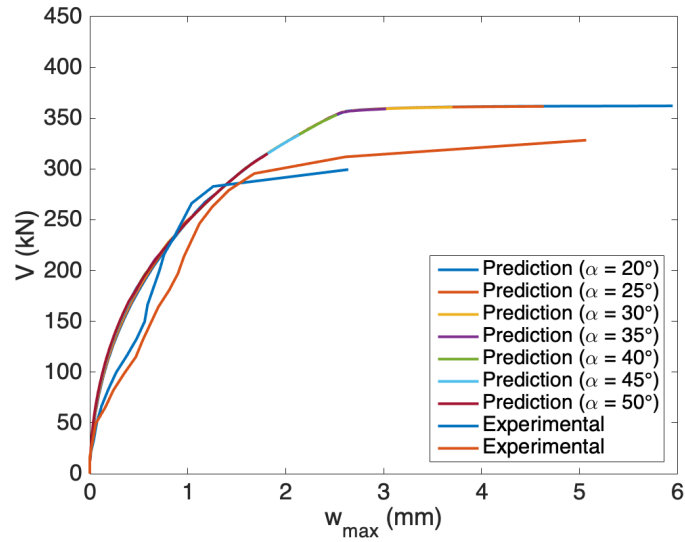
Figure 5.8: Comparison between experimental results and predicted values for different α (Mata Falcón)

presents a more ductile behavior but the predicted peak strength is reached for an $\alpha = 30\text{-}35°$. The crack width does not import once the peak capacity is reached. Also, only six experimental specimens have been compared to predicted crack widths, it is not representative enough. More and more experimental tests have to be performed and compared to predictions to choose the best value for α. In order to get predicted results as similar as possible to the experimental ones, a calibrating $\alpha = 30°$ looks to be the best compromise. The peak response is reached for this value and the crack width is conservative because for a given crack width, the model predicts higher support reaction and the peak resistance of the dapped-end is reached sooner. Although α is not defined in the literature, different papers use to take a dilatation angle of concrete damaged plasticity around 30° which is linked to what just has been said, see REFERENCES [12] & [25].

The FIGURE 5.9 below studies the average and the coefficient of variation by increasing the angle α of the CDZ. The angle varies from 20° to 50° with a step of 5°. It can be seen that the average is not so much sensitive to α. Moreover, the coefficient of variation does not change a lot from 12% for $\alpha = 20°$ to 10% for $\alpha = 30°$. Using $\alpha = 30°$ to assess the geometry of the compression damage zone gives good results regarding to the average and the CoV and makes sense with what is generally used in literature. This parameter is not fixed and depends on different factors (mix proportions of the concrete, imperfections, compressive concrete strength,...) but a value taken as 30° is realistic.
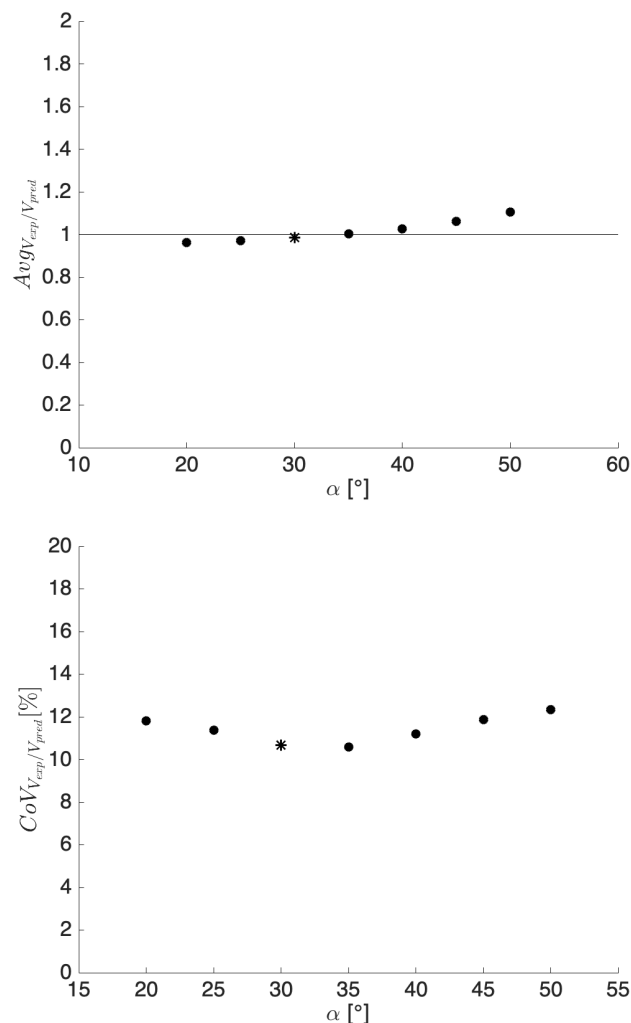
Figure 5.9: Analysis of the average and the coefficient of variation with the variation of α

FIGURE 5.10 presents the flexural capacity experimental-to-predicted ratio according to the depth of the nib of the dapped-end. It can be seen that the majority of specimens have a nib smaller than 200 mm, which is very small and only a few (`Elliott` and `Mata Falcón`) have a nib of more than 200 mm. The larger the dimensions of the structures, the more the errors are minimized. Mata Falcón specimens have a very low coefficient of variation. Elliott's specimens are less representative because of the large number of assumptions that had to be made. According to this diagram, the depth of the nib does not have a strong impact on the results although it does might the quality of the results.
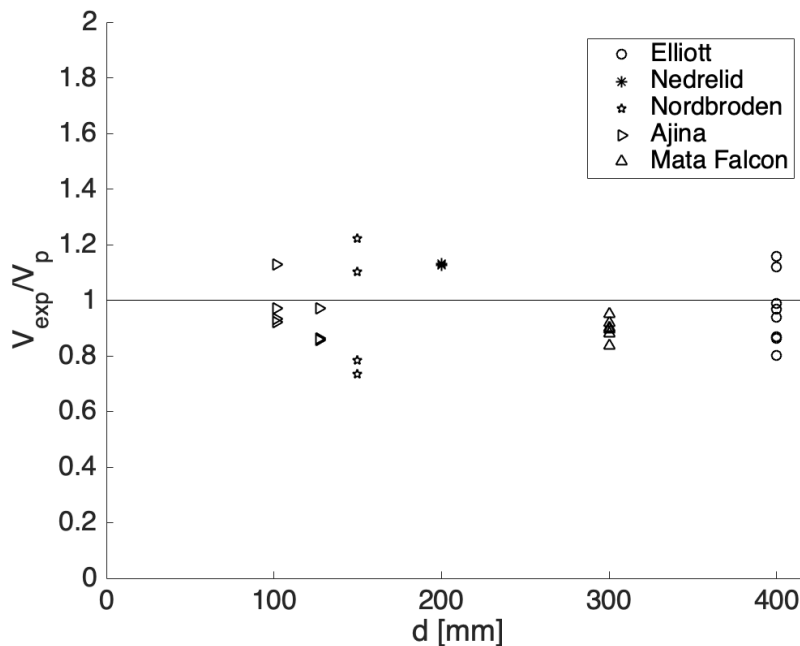
Figure 5.10: Strength experimental-to-predicted ratio according to the height of the nib

FIGURES 5.11, 5.12 and 5.13 study the evolution of the support reaction with the increase of the strain at the top of the compression zone ε_{top}. This represents the evolution of the flexural capacity V as the structure is loaded. In the simplified approach, the peak flexural capacity was calculated for a maximum strain value of $\varepsilon_{top} = 0.0035$. However, the peak resistance can occur further. Theoretically, the flexural capacity will increase with the strain until it reaches a plateau. The curves show each time a discontinuity around $\varepsilon_{top} = 2.1$ because the level arm of the force in the compression undamage zone is calculated by 2/3 x, see equation (40). The stress-strain curve idealizes the pre-peak behavior as a straight line although around the peak, the curve is not straight at all. In a post-peak behavior, the level arm is obtained by using a moment equilibrium to know the application point of the resulting force. This has no consequences on the final results except the slight discontinuity occurred for $\varepsilon = 2.1$.

FIGURE 5.11 presents three plots based on specimens performed by Mata Falcón by increasing the amount of fibers. First of all the main contribution to the flexural capacity is from the steel reinforcement. Then, a short contribution is due to the compressive strength of the concrete and the contribution of the fibers increases with the fiber volume ratio. Regarding to those specimens, the FRC kinematic model is unconservative and predicts higher capacity than the experimental one. However, the flexural capacity for a strain assumed at 3.5 x 10^{-3} is really similar to the experimental peak capacity. Also, the contribution of the fibers decreases from a certain value of ε because the more the dapped-end is loaded, the more the main crack from the re-entrant corner will open. At

the level of the re-entrant corner where the crack width is larger, the fibers will reach their maximum strength and will rupture. As a result, there will be a loss of strength in the fibers and the contribution from the fibers will decrease.
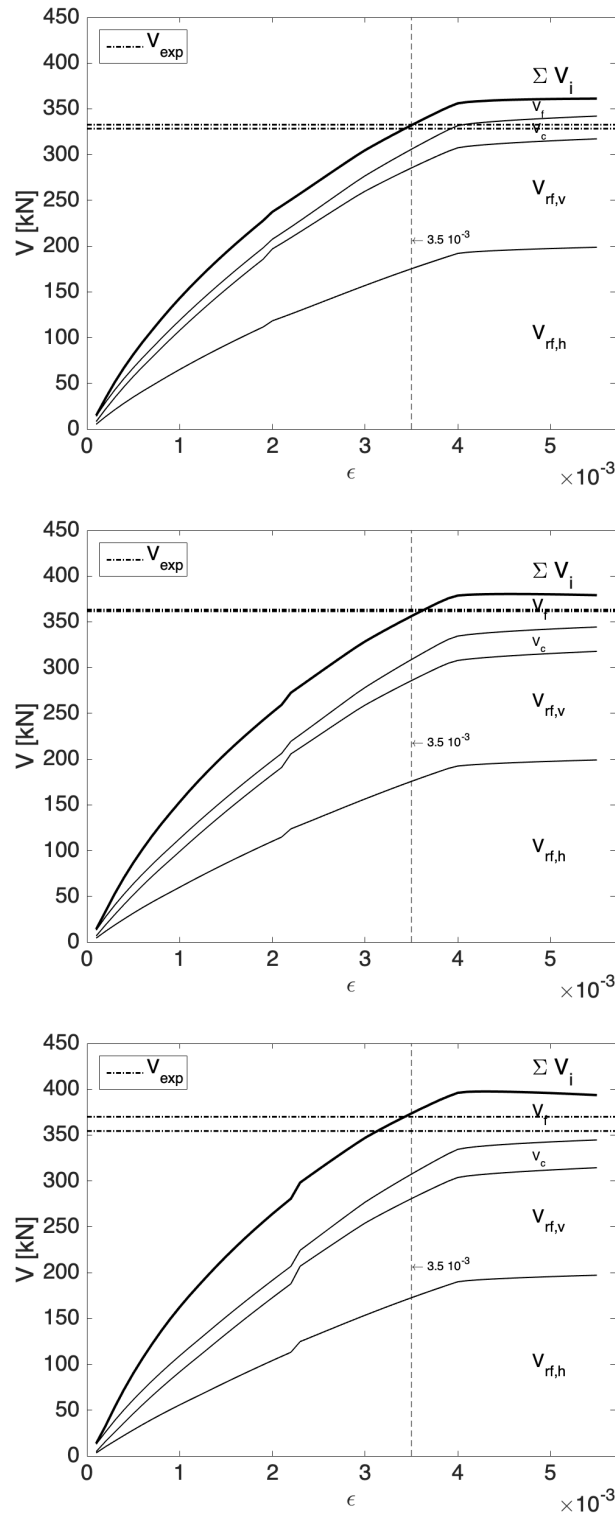
Figure 5.11: Contribution of each element according to the strain at the top of the concrete and comparison with tests (0.5, 0.87 & 1.24% of fiber volume ratio) from Mata Falcón

FIGURES 5.12 and 5.13 present the contribution of each element of the dapped-end as the strain increases for specimens from Ajina respectively for a different height of the nib and for different amount of fibers. The plateau would be reached for a bigger strain than 0.0055. However, the model assumes that the concrete never presents a higher compression strain. On a way to be the most realistic, the peak flexural capacity is used for $\varepsilon_{top} = 0.0055$. Again, the flexural capacity assessed for an $\varepsilon = 0.0035$ predicts more conservative results.
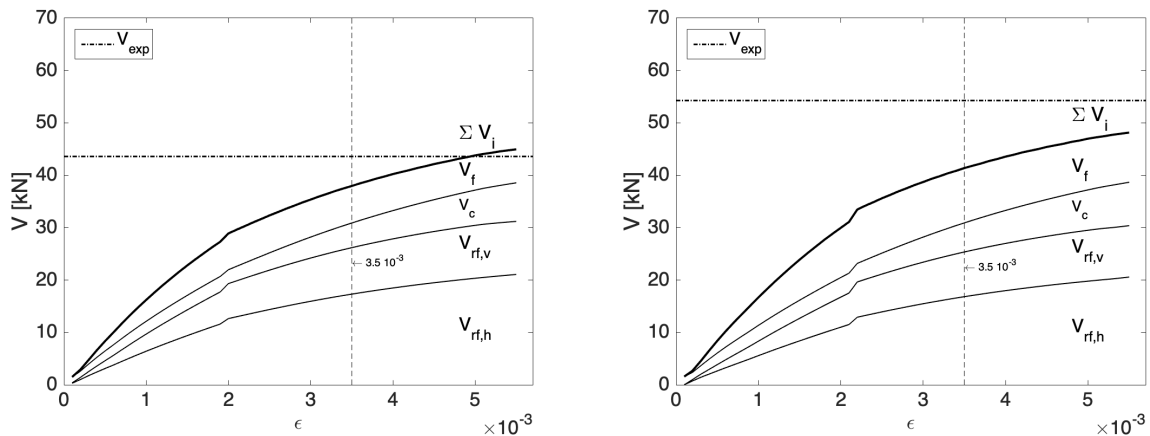
Figure 5.12: Contribution of each element according to the strain at the top of the concrete and comparison with tests (0.8 & 1.2% of fiber volume ratio) from Ajina for h=4"
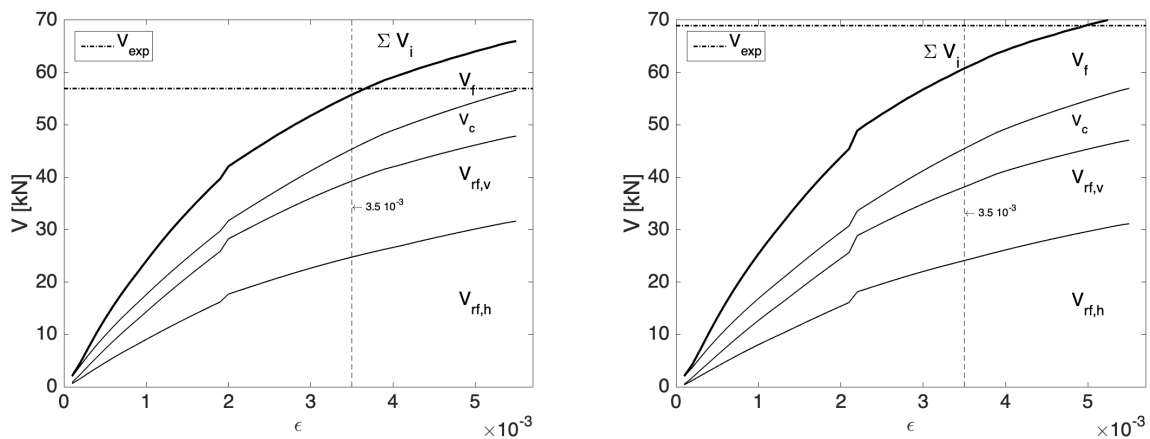
Figure 5.13: Contribution of each element according to the strain at the top of the concrete and comparison with tests (0.8 & 1.2% of fiber volume ratio) from Ajina for h=5"

While the load on the dapped-end increases, the crack opens and the crack width at the re-entrant corner increases. The crack width can be linked to the strength of the dapped-end and the kinematic model is aimed at assessing the flexural capacity by measuring the inclination angle of the crack from the re-entrant corner on existing structures. By analyzing the complete behavior, the crack width can also be used as a data and an input to the model to assess the support reaction. FIGURE 5.14 presents the evolution of the support reaction according to the increase of the crack width plotted from the kinematic model and compared with the experimental crack widths. Those diagrams predict the peak flexural capacity for a certain crack width at the re-entrant corner. By measuring the crack width at the re-entrant corner at a certain moment on existing structures, the support reaction can be predicted by analyzing those diagrams below. The model is conservative in the sense that it predicts failure

for a smaller crack width than that observed in experimental tests. If the second diagram of FIGURE 5.14 is analyzed, a flexural capacity is predicted via the kinematic model for a crack width at the re-entrant corner of 3.18 mm. By measuring the crack width on existing structure, the measured value can be reported on this diagram and this returns an indicator that determines the support reaction with respect to the predicted flexural capacity. For example, for a value measured in situ $w_{max} = 2$ mm, the support reaction is 354 kN and although the crack width at failure is 3.18 mm, the support reaction will have reached 354/380 = 93% of its peak capacity. This analysis could allow a confident statement of the existing structure by developing different V-w curves with a measurement of the crack width at different level of the crack, for example at each reinforcement. It would be enough to measure different crack widths on an existing structure and compare the different curves obtained to have the most realistic assessment possible. The crack will not be straight and errors can be induced. By comparing different measurements, it would minimize the error.
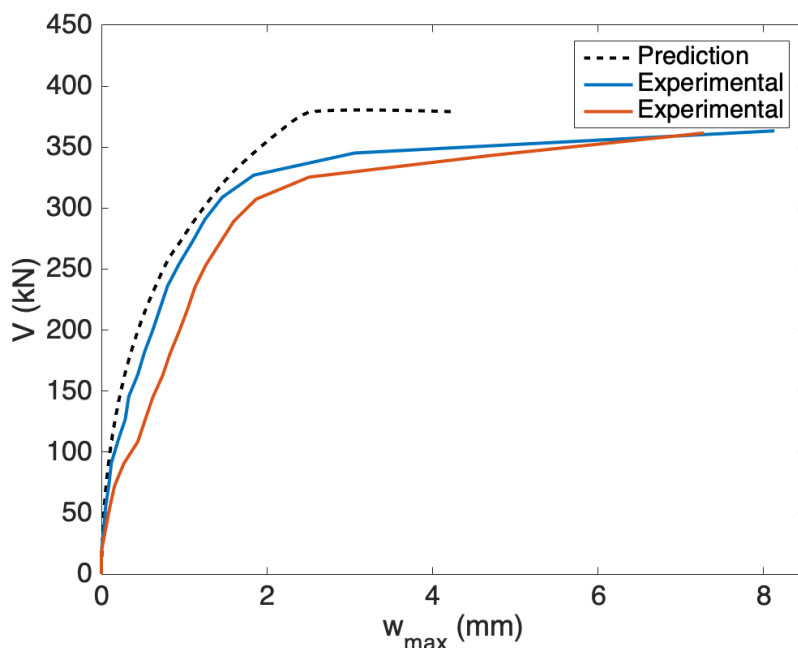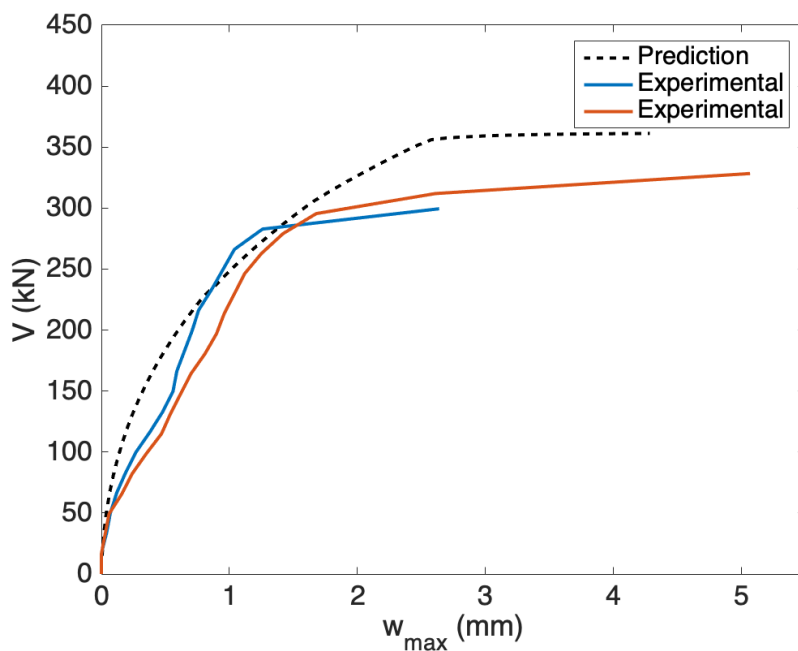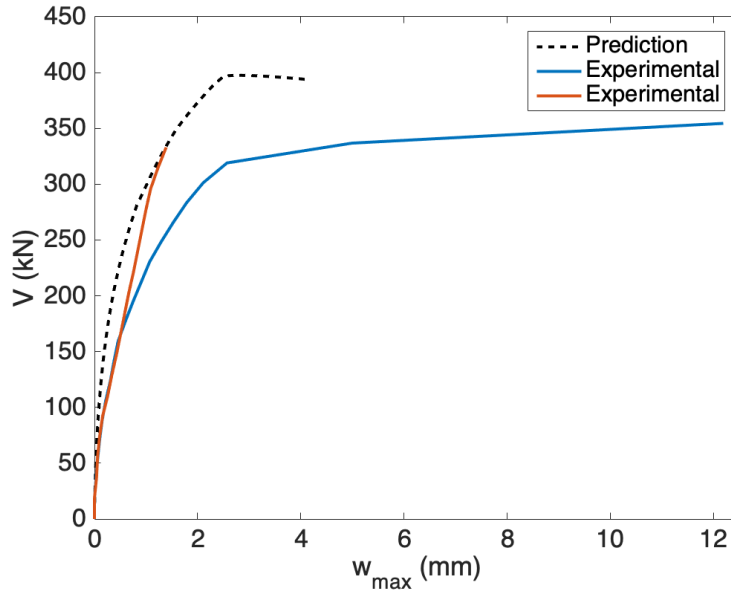
Figure 5.14: Contribution of each element according to the strain at the top of the concrete and comparison with tests (0.5, 0.87 & 1.24% of fiber volume ratio) from Mata Falcón

In addition to predict the support reaction for a given measured crack width, it can be seen in FIGURE 5.15 that while the amount of fibers increases, not only is the peak capacity higher but also the crack width decreases for a same loading condition. The crack opens due to a tensile stress along the crack and by adding fibers into the concrete, the tensile force can be taken up by the fibers, not only by the steel reinforcement. For a given support reaction equals to 250 kN, the crack width at the re-entrant corner is approximately 1.98 mm without FRC. By increasing the fiber volume ratio to 0.5, 0.87 and 1.24%, the crack width decreases considerably to 1.02, 0.75 and 0.61 mm respectively. If the crack width decreases while the fiber volume ratio increases, water will enter less easily in the crack, decreasing the velocity of corrosion and external agents will attack less the element which increases its durability.
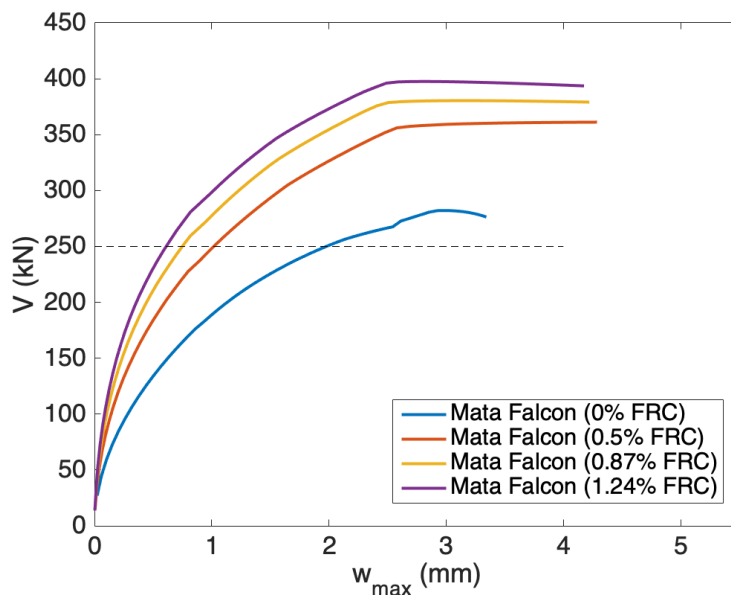
Figure 5.15: Impact of the fibers on the crack width

6 Conclusions

The use of fiber-reinforced concrete in dapped-end connections is very promising for the future. Indeed, these elements are especially subjected to high stress concentrations due to their abrupt reduction in cross-section. Traditionally designed with conventional concrete, dapped-end connections are susceptible to brittle behavior and unexpected failure. This is dangerous for bridge users (car drivers or pedestrians) or the road system because it does not prevent sudden collapse. FRC structures not only allow for a more ductile behavior of the material due to the higher compressive strength of the concrete in its post-peak behavior but also the fibers make an important contribution to the peak strength of the dapped-end.

The fibers provide better crack control, reduce cracking for the same loading condition and the flexural capacity of the element increases with the fiber volume ratio. This higher resistance and especially the reduction of cracks allow less recurrent monitoring of the structure, the maintenance will be lower and the durability of the dapped-end will be significantly increased.

The kinematic model developed in this study applies to fiber-reinforced concrete dapped-end connections whose failure mode is a flexural failure governed by the opening of the inclined crack from the re-entrant corner. At first, a simplified approach was developed to predict the peak capacity of a dapped-end by measuring the inclination angle of the main crack and using this data as input to the model. The simplified approach assumes that the element reaches its peak flexural response when the compression damage zone reaches a strain $\varepsilon = 0.0035$ at its top fiber. Then, the model was established in order to study the complete behavior of a dapped-end and to predict its real peak capacity. Moreover, the complete behavior allows to model the evolution of the crack during loading. This would allow to compare the theoretical curves obtained with the state of cracking of an existing structure and to deduce the service conditions and the possible maintenance, renovation or repair steps to be undertaken.

After collecting a set of data from 5 different scientific papers and assembling them in the most meticulous way possible, the theoretical results predicted by the kinematic model are in agreement with the experimental data according to the simplified approach with an average of the experimental-to-predicted ratios of 1.07 which is conservative and a coefficient of variation of 13.6%. According to the complete approach, the average experimental-to-predicted ratio is 0.97 while the coefficient of variation is 11.13%. In terms of predicted flexural capacity, both approaches show excellent results. The complete approach predicts relatively well and safely the evolution of the crack although few data could be compared to the model and more data would allow to know if the model is sufficiently representative of the reality.

Unlike many design models such as the strut-and-tie model which is used in design flexural calculations at ultimate limit state, the kinematic model takes into account the kinematics of the dapped-end and its conditions in service. This model would allow a better follow-up of existing structures and the results presented in this study are very promising. Moreover, the kinematic model could be further developed by simulating the way the dapped-end evolves with time. As the crack evolves over time, water or other external agents could infiltrate the cracks and further damage the structure. The kinematic model would be able to take these elements into account, to evaluate the reduction of section by corrosion of the reinforcements, the modification of the bond stress as well as the impact that these agents would have on the fibers. This would allow a complete representation of the lifespan of a dapped-end, to prevent problems and solve them before they occur.

7 Appendix

Paper 1: "Effect of steel fibers on precast dapped-end beam connections"

This document, recognized in the literature, is extracted from a thesis written by *Jamal M. AJINA* in 1986 as part of a Master degree at South Dakota State University, see REFERENCE [1]. The units used are expressed in American units (psi as unit of pressure and inch as unit of length, respectively converted to MPa and mm). Two types of specimens were studied, see FIGURE 7.1 and 7.2. They differ by the height of the dapped-end (4" or 5") while the height of the full beam is 10". The inclined angle of the crack θ is measured on the basis of the experimental specimens. Cracks occurred when angle θ was between 44 and 46°. Therefore, $\theta = 45°$ is used as an input to predict the flexural capacity. The common characteristics of the different specimens are listed below:

- H = 10" = 254 mm

- b = 5" = 127 mm

- a = 4.5" = 114.3 mm

- f'_c = 4195 psi = 29 MPa (for $\rho_f = 0\%$)

- f'_c = 4420 psi = 30.47 MPa (for $\rho_f = 0.8\%$)

- f'_c = 4540 psi = 31.3 MPa (for $\rho_f = 1.2\%$)

- Hooked-end fibers

- l_f = 2" = 50.8 mm

- l_i = 40.8 mm (assumption)

- d_f = 0.02" = 0.508 mm

- $\frac{l_f}{d_f}$ = 100

	$f_{y,s}$, ksi (MPa)	$f_{u,s}$, ksi (MPa)
#2	62.2 (456)	98.1 (676)
#3	71.3 (491)	111.2 (767)
#4	67.3 (464)	110.6 (763)
#5	67.5 (465)	110.5 (762)

Table 7.1: Yield and ultimate strengths of the reinforcement according to the rebars used in the dapped-end
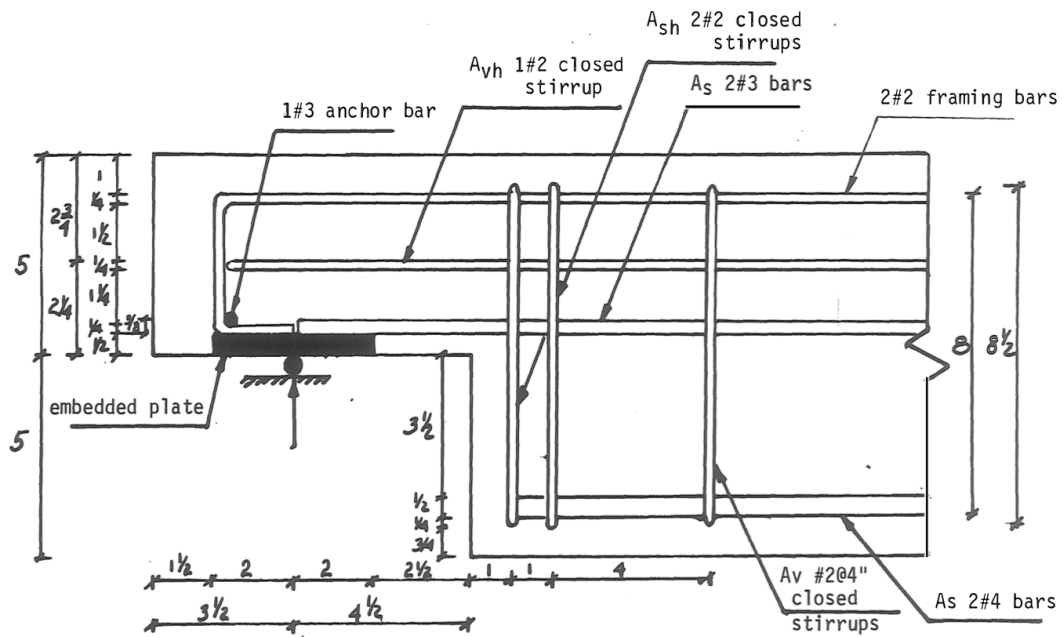
Figure 7.1: Specimen details for h = 5" = 127 mm [1]
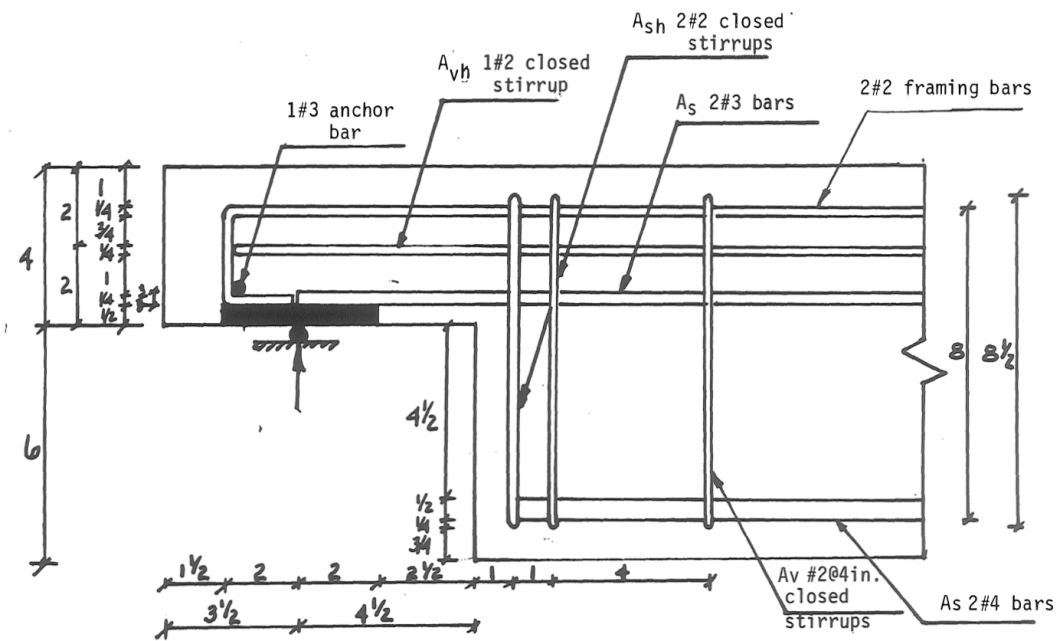
Figure 7.2: Specimen details for h = 4" = 101.6 mm [1]

Group No.	Beam No.	% of Steel Fibers (P_5)	Depth above the Dap (h) inches	Load Location (X) inches	Dapped End Reinforcement A_s(in^2)	A_{sh}(in^2)	A_{vh}(in^2)	Main Beam Reinforcement As	Av
G1	B1	0.0				2 #2	1 #2		12 #2
	B7	0.8	5	11.5	2 #3	closed	closed	2 #4	closed
	B14	1.2			bars	ties	tie	bars	stirrups at 4.0"
G2	B2	0.0				2 #2			12 #2
	B9	0.8	5	11.5	2 #3	closed	None	2 #4	closed
	B16	1.2			bars	ties		bars	stirrups at 4.0"
G3	B5	0.0				2 #2	1 #2		12 #2
	B11	0.8	4	10.5	2 #3	closed	closed	2 #4	closed
	B15	1.2			bars	ties	tie	bars	stirrups at 4.0"
G4	B6	0.0				2 #2			12 #2
	B13	0.8	4	10.5	2 #3	closed	None	2 #4	closed
	B18	1.2			bars	ties		bars	stirrups at 4.0"
G5	B3	0.0				2 #2	1 #2		12 #2
	B10	0.8	5	16.5	2 #3	closed	closed	2 #5	closed
	B17	1.2			bars	ties	tie	bars	stirrups at 4.0"
G6	B4	0.0							
	B8	0.8	5	11.5	None	None	None	None	None
	B12	1.2							

Figure 7.3: Dapped-end beam arrangement [1]

Paper 2: "Estudio del comportamiento en servicio y rotura de los apoyos a media madera"

Also named "Serviceability and Ultimate Behaviour of Dapped-end Beams" in English, this paper was written by *Jaime Mata Falcón* and published as his doctoral thesis at Polytechnic University of Valence, see REFERENCE [15]. All the design and reinforcement details are shown in FIGURE 7.4. This paper is very interesting in that the similarly designed specimens were simply tested with a different amount of fibers (from 0 to 1.24% by volume). The below TABLE contains the yield and ultimate strengths of the reinforcement:

	f_{ys}, MPa	f_{us}, MPa
$\phi 8$	509.3	659.9
$\phi 10$	542.4	645.4
$\phi 12$	551.7	651.8
$\phi 15$	983.2	1184
$\phi 16$	529.7	637.6
$\phi 25$	540.9	649.8

Table 7.2: Yield and ultimate strengths of the reinforcement according to the rebars used in the dapped-end

The common characteristics are described as following:

- b = 250 mm

- $f_c' = 31.1$ MPa (for $\rho_f = 0\%$)

- $f_c' = 45.5$ MPa (for $\rho_f = 0.5\%$)

- $f_c' = 48.8$ MPa (for $\rho_f = 0.87\%$)

- f'_c = 48.4 MPa (for ρ_f = 1.24%)

- The type of hooked-end fibers is DRAMIX RC-65/35-BN

- d_f = 0.55 mm

- l_f = 35 mm and l_i = 25 mm (assumed to be 10 mm less than l_f)
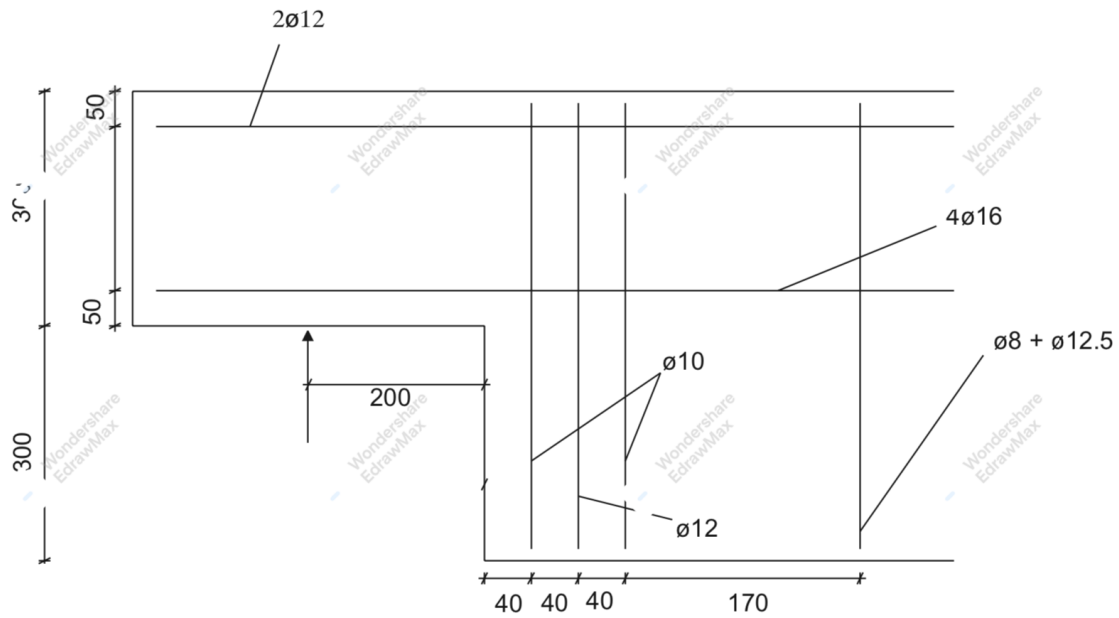
Figure 7.4: Specimen details, all specimens from Mata Falcón

Paper 3: "Shear strength of short recess precast dapped-end beams made of fibers self-compacting concrete"

This paper was written in the context of a conference given in 2008 by *R. N. Mohamed* and *K. S. Elliott* (University of Nottingham, United Kingdom), see REFERENCE [13]. It does not contain many details on the design of the dapped-end and many assumptions had to be made. Nevertheless, the angle of inclination θ crack is measured with such a high precision that these measurements cast some doubts. Indeed, when the crack is analyzed on an existing structure, it is never straight and therefore the angle must be estimated to be consistent with the crack inclination. Based on the diagram and measuring with the highest possible accuracy FIGURE 7.5, the details of each specimen are represented in FIGURES 7.6 to 7.8.

Specimen	Concrete strength	Vf	av / d	Reinforcing details				Anchorage type
				Vertical		Horizontal		
				Bars	As	Bars	As	
	Mpa	(%)			mm^2		mm^2	
SR 1	45.0	0.0	1.35	4 T12 @ 2 legs	904	2 T20	628	Welded to bar
SR 2	46.5	1.0	1.35	4 T12 @ 2 legs	904	2 T20	628	Welded to bar
SR 3	47.5	1.0	1.35	2 T12 @ 2 legs	452	2 T20	628	Welded to bar
SR 4	42.0	1.0	1.35	4 T12 @ 2 legs	904	3 T12	339	Welded to bar
SR 5	49.0	1.0	1.35	4 T12 @ 2 legs	904	2 T20	628	Welded to plate
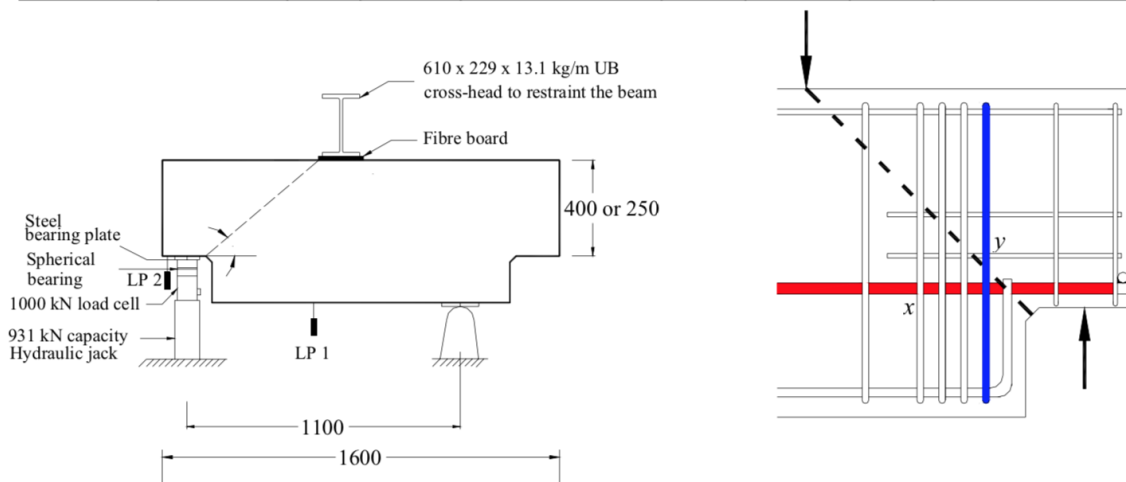
Figure 7.5: Information from the paper [13]

Information needed to predict the flexural capacity are listed as follows:

- b = 300 mm

- The type of hooked-end fibers is DRAMIX RC-65/35-BN

- l_f = 35 mm and l_i = 25 mm (assumed to be 10 mm less than l_f)

- ρ_f = 0% for specimen SR1

- ρ_f = 1% for specimens SR2 to SR5

- f_{yk} = 530 MPa (assumption)

- f_{uk} = 1.08·530 MPa (assumption)

- Each distance reported on the specimen details is reported by measuring the diagram in FIGURE 7.5 (assumed to be to scale).
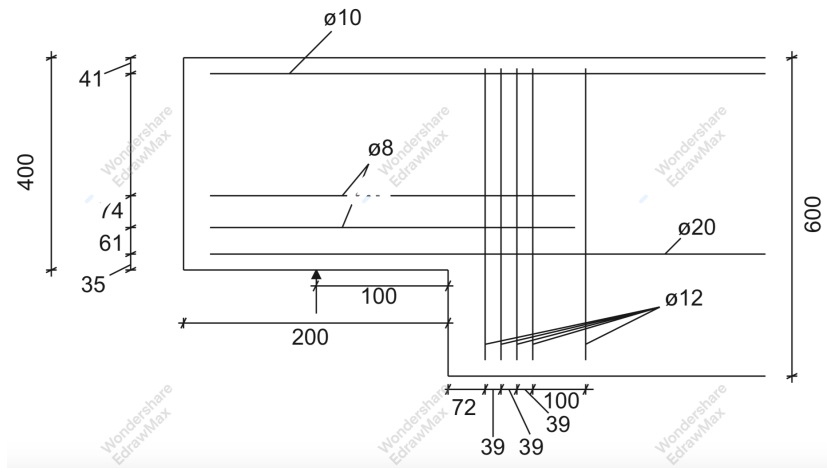
Figure 7.6: Specimen details, beam 1,2 & 5
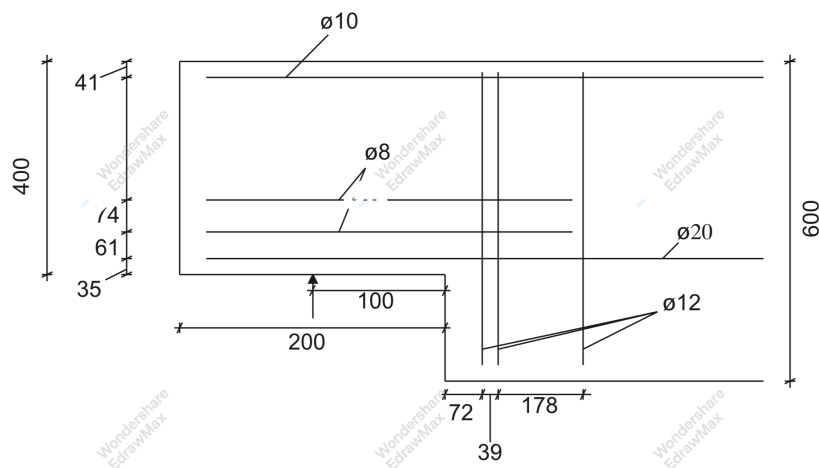
Figure 7.7: Specimen details, beam 3
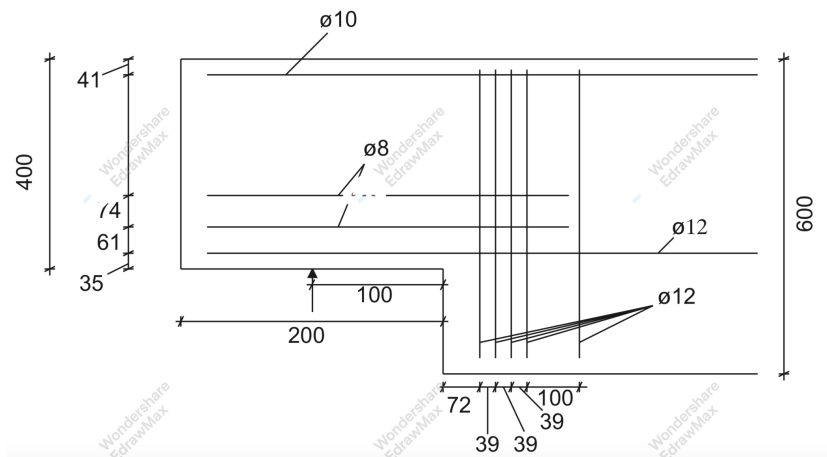
Figure 7.8: Specimen details, beam 4

Paper 4: "Structural FRC – Design approach and experimental results"

This paper was written at NTNU University in 2015 by *Håvard Nedrelid* and published in COIN Project report n°66, see REFERENCE [24]. A COIN design approach is proposed and compared to experimental results with 2 types of fibers, one type of hooked-end steel fibers and one type of mixed fibers (synthetic and steel fibers). Only the first type is of interest for the present study and the experimental tests are reported in the database. The weakness of this paper is the amount of data that had to be assumed. Even the detail of the reinforcement is not indicated and the reinforcement arrangement had to be measured on the diagrams considered to scale. The geometric and reinforcement details of the different specimens are shown in FIGURES 7.9 to 7.11. Here are the common data between the specimens:

- f'_c = 43.2 MPa (for C40/50)

- f'_c = 63.6 MPa (for SFRC)

- f_{yk} = 530 MPa (assumption)

- f_{uk} = 1.08·530 MPa (assumption)

- θ = 45° (assumption)

- ρ_f = 0% for C40/50 (specimen A and B)

- ρ_f = 1% for SFRC (specimen B and D)

- The type of fibers is DRAMIX 65/60

- l_f = 60 mm and l_i = 50 mm (assumed to be 10 mm less than l_f)

- d_f = 0.9 mm
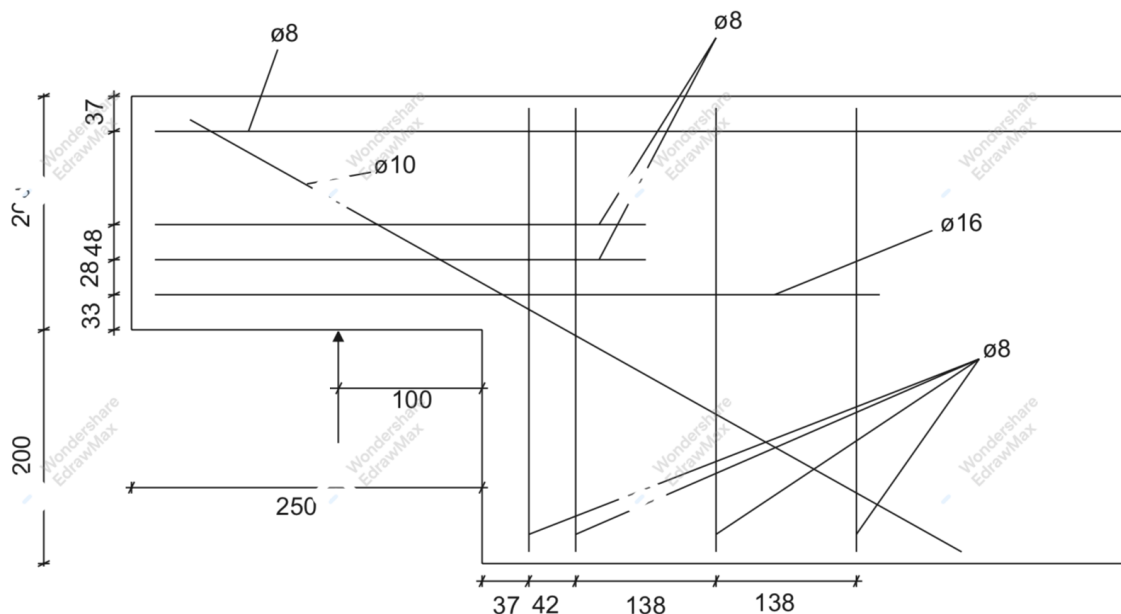
Figure 7.9: Specimen details, beam A
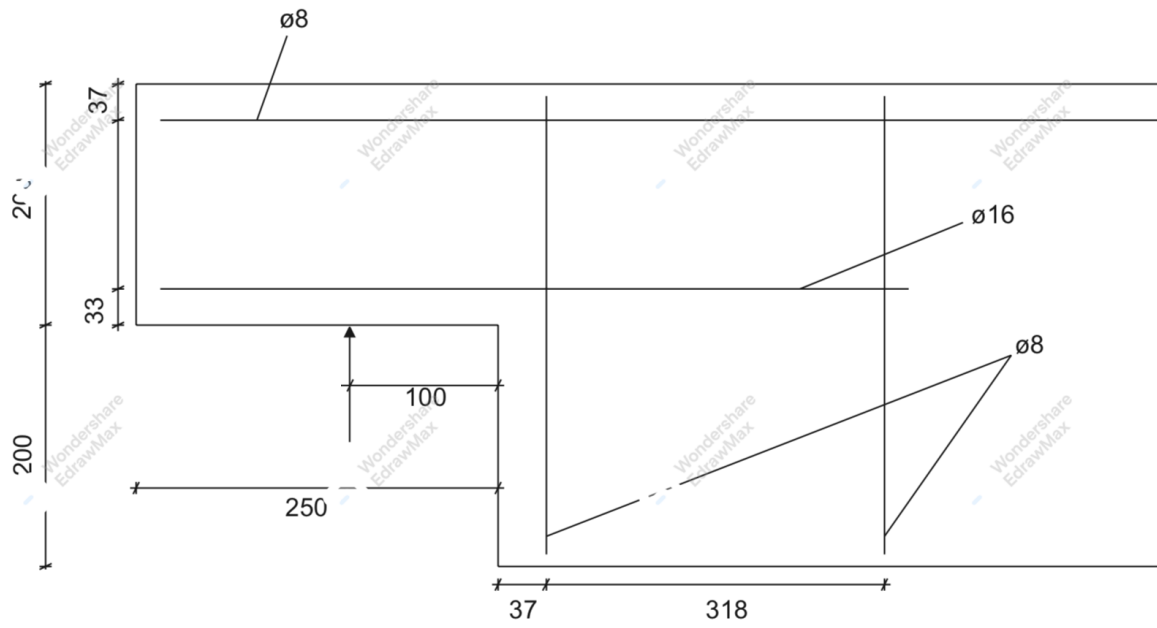
Figure 7.10: Specimen details, beam B
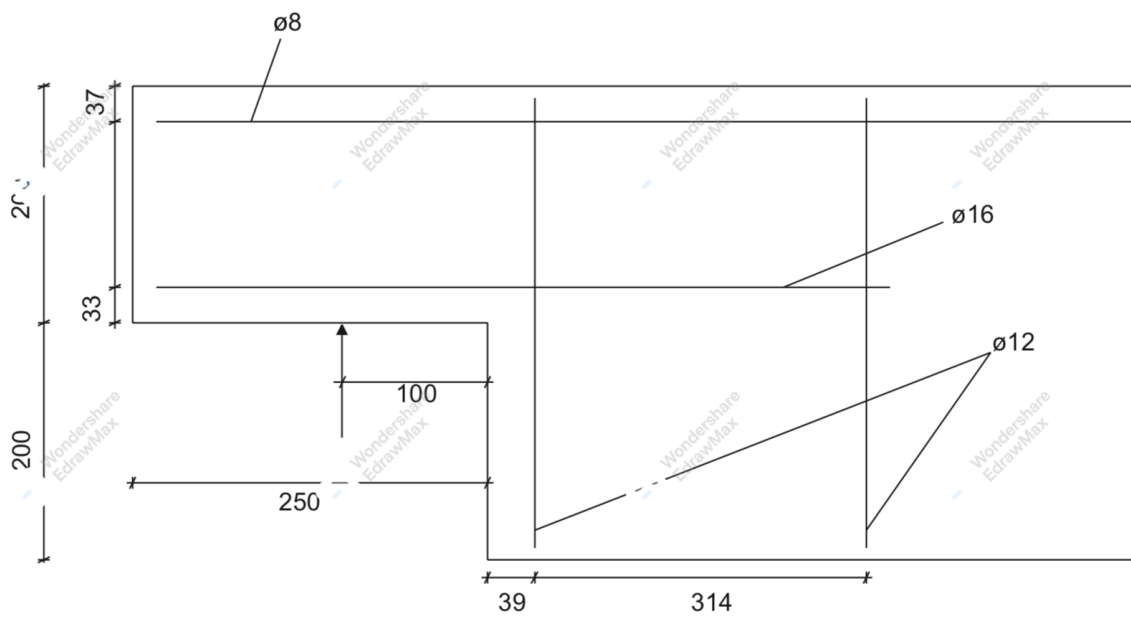
Figure 7.11: Specimen details, beam D

Paper 5: "Testing of Fibre Reinforced Concrete Structures"

Also written at NTNU but as a master thesis written by *Hanna Haugen Nordbrøden* and *Siri Hansen Weydahl* in 2012, this paper is aimed at studying the use of fibers in concrete on shear capacity of corbel-end beams, see REFERENCE [26]. A first theoretical approach is studied by using different models and then compared to experimental tests performed. Although the specimens are small (only 150 mm height for the dapped-end), the details and the number of data are of high quality and few assumptions had to be made. The precise details of the reinforcement are shown in FIGURES 7.12 to 7.15, the remaining data are listed below:

- $\rho_f = 0\%$ for specimen A and B

- $\rho_f = 1\%$ for specimen C and D

- $f_{yk} = 500$ MPa (value used in the teorical calculations in the paper)

- $f_{uk} = 1.08 \cdot 500$ MPa (assumption)

- $\theta = 45°$ (assumption)

- The type of fibers is DRAMIX 65/60

- $l_f = 60$ mm and $l_i = 50$ mm (assumed to be 10 mm less than l_f)

- $d_f = 0.9$ mm
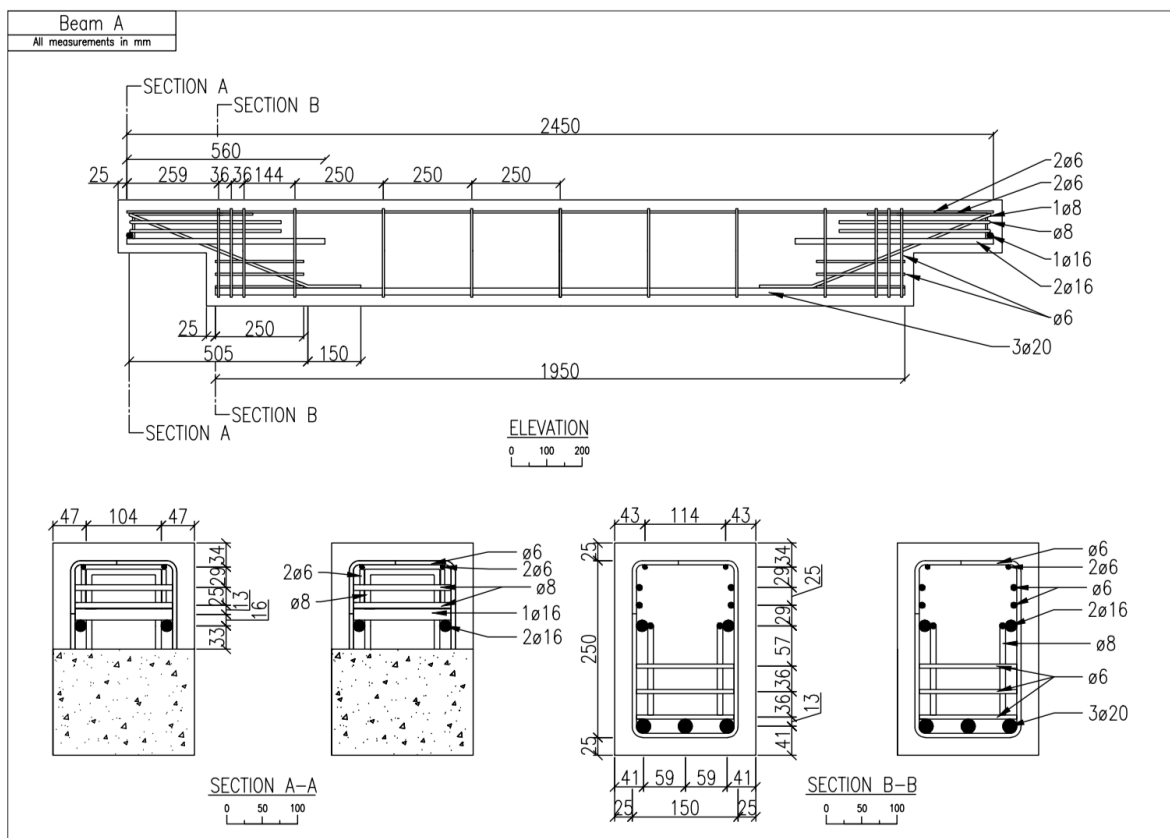
Figure 7.12: Specimen details, beam A [26]
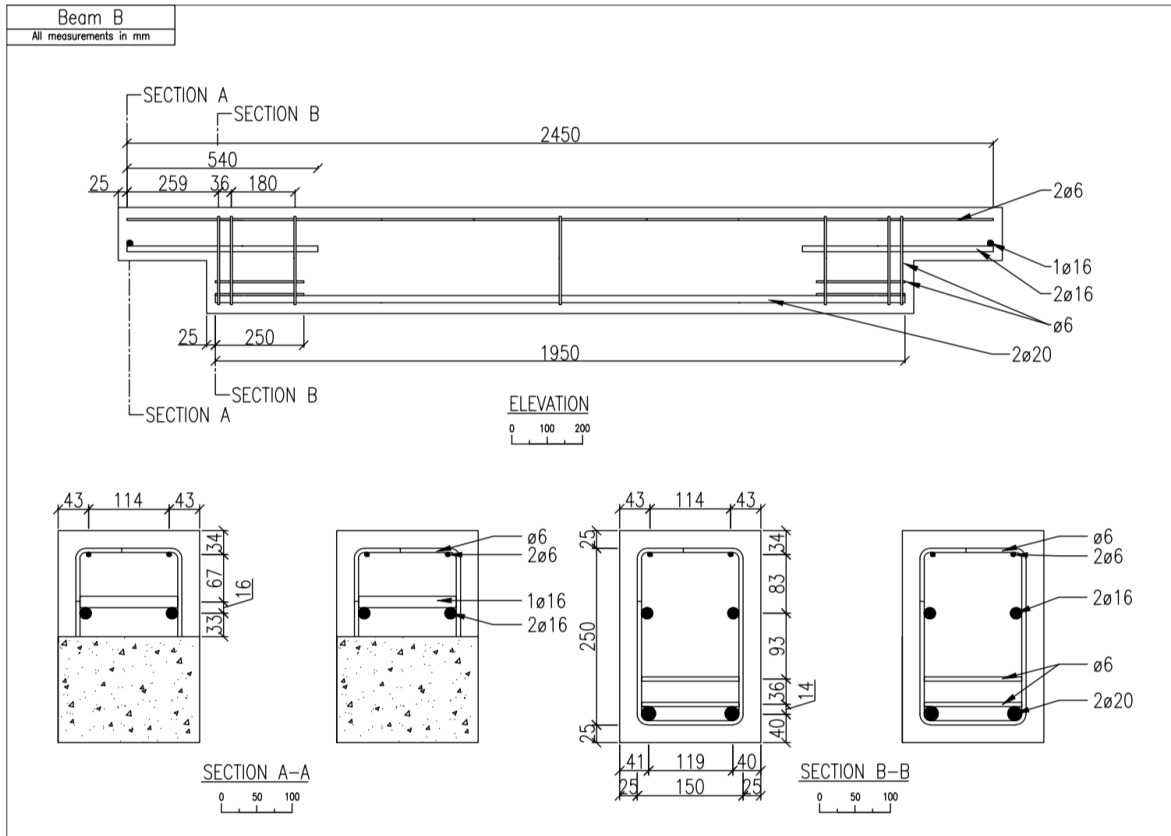
Figure 7.13: Specimen details, beam B [26]
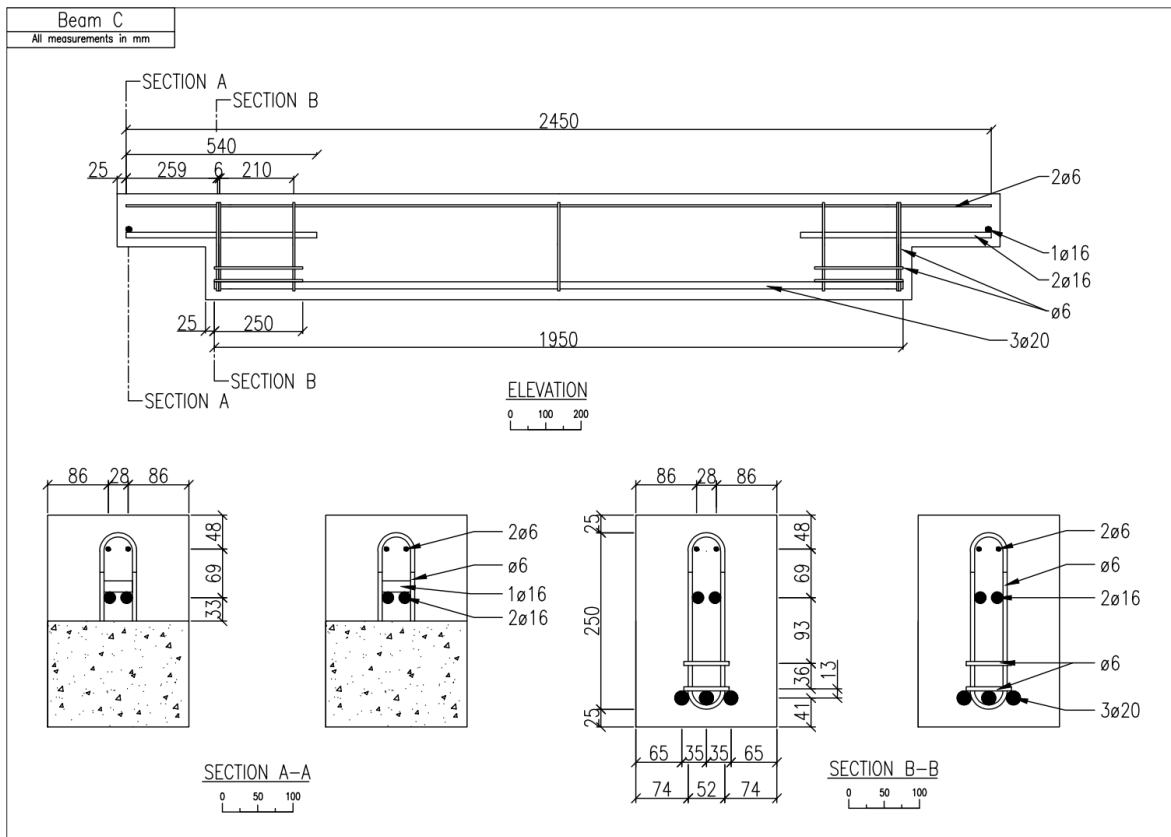
Figure 7.14: Specimen details, beam C [26]
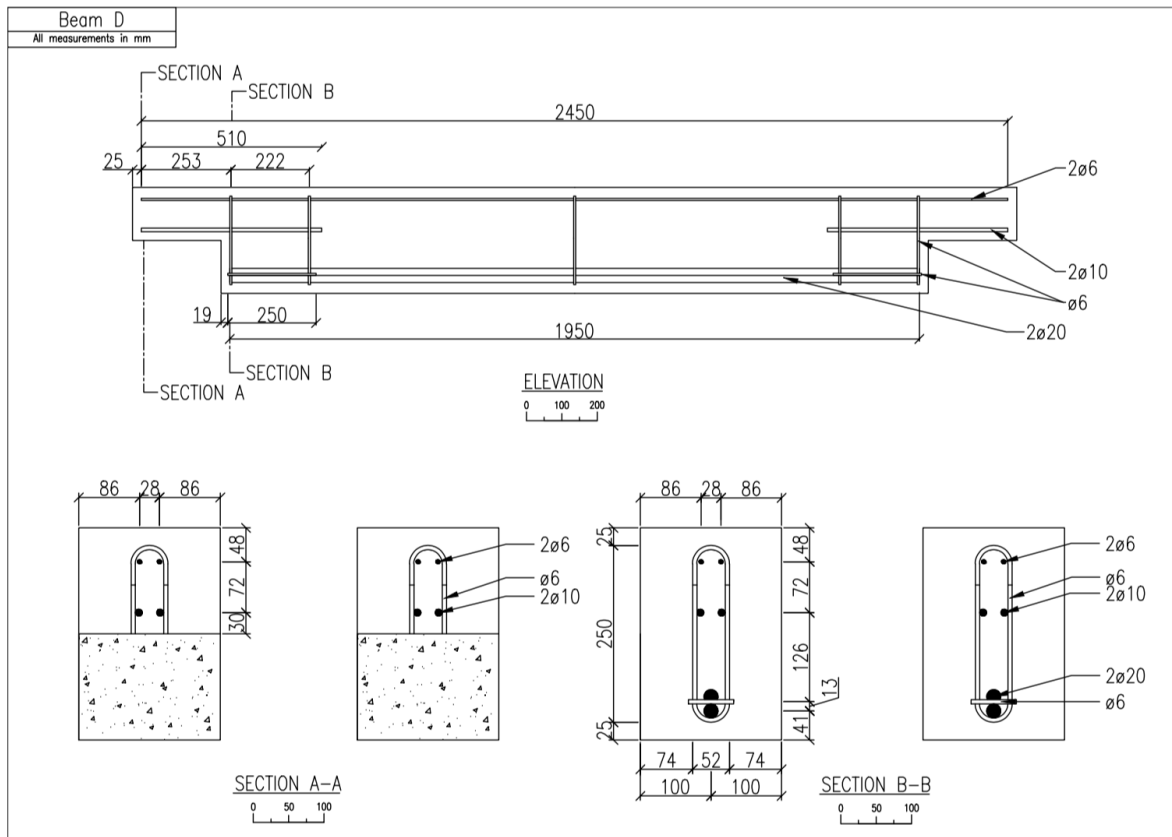
Figure 7.15: Specimen details, beam D [26]

Database

No.	Ref.	Beam name	a/d	a (mm)	d (mm)	h (mm)	b (mm)	Horizontal reinforcement								
								Layer 1			Layer 2			Layer 3		
								diameter	fyh (MPa)	Ash (mm^2)	diameter	fyh (MPa)	Ash (mm^2)	diameter	fyh (MPa)	Ash (mm^2)
1	[1]	B1	1.04	114.3	109.5	127	127	Φ9.53	491	142.5	Φ6.35	456	63.3	-	-	-
2		B7	1.04	114.3	109.5	127	127	Φ9.53	491	142.5	Φ6.35	456	63.3	-	-	-
3		B14	1.04	114.3	109.5	127	127	Φ9.53	491	142.5	Φ6.35	456	63.3	-	-	-
4		B2	1.04	114.3	109.5	127	127	Φ9.53	491	142.5	Φ6.35	456	63.3	-	-	-
5		B9	1.04	114.3	109.5	127	127	Φ9.53	491	142.5	Φ6.35	456	63.3	-	-	-
6		B16	1.04	114.3	109.5	127	127	Φ9.53	491	142.5	Φ6.35	456	63.3	-	-	-
7		B5	1.36	114.3	84.1	101.6	127	Φ9.53	491	142.5	Φ6.35	456	63.3	-	-	-
8		B11	1.36	114.3	84.1	101.6	127	Φ9.53	491	142.5	Φ6.35	456	63.3	-	-	-
9		B15	1.36	114.3	84.1	101.6	127	Φ9.53	491	142.5	Φ6.35	456	63.3	-	-	-
10		B6	1.36	114.3	84.1	101.6	127	Φ9.53	491	142.5	Φ6.35	456	63.3	-	-	-
11		B13	1.36	114.3	84.1	101.6	127	Φ9.53	491	142.5	Φ6.35	456	63.3	-	-	-
12		B18	1.36	114.3	84.1	101.6	127	Φ9.53	491	142.5	Φ6.35	456	63.3	-	-	-
13		B3	1.04	114.3	109.5	127	127	Φ9.53	491	142.5	Φ6.35	456	63.3	-	-	-
14		B10	1.04	114.3	109.5	127	127	Φ9.53	491	142.5	Φ6.35	456	63.3	-	-	-
15		B17	1.04	114.3	109.5	127	127	Φ9.53	491	142.5	Φ6.35	456	63.3	-	-	-
16	[15]	DEB-1.6-T1	0.8	200	250	300	250	Φ16	530	804	-	-	-	-	-	-
17		DEB-1.6-T2	0.8	200	250	300	250	Φ16	530	804	-	-	-	-	-	-
18		DEB-3.7-T1	0.8	200	250	300	250	Φ16	530	804	-	-	-	-	-	-
19		DEB-3.7-T2	0.8	200	250	300	250	Φ16	530	804	-	-	-	-	-	-
20		DEB-3.8-T1	0.8	200	250	300	250	Φ16	530	804	-	-	-	-	-	-
21		DEB-3.8-T2	0.8	200	250	300	250	Φ16	530	804	-	-	-	-	-	-
22		DEB-3.9-T1	0.8	200	250	300	250	Φ16	530	804	-	-	-	-	-	-
23		DEB-3.9-T2	0.8	200	250	300	250	Φ16	530	804	-	-	-	-	-	-
24	[13]	SR1-T1	0.27	100	365	400	300	Φ20	530	628	Φ8	530	100.5	Φ8	530	100.5
25		SR1-T2	0.27	100	365	400	300	Φ20	530	628	Φ8	530	100.5	Φ8	530	100.5
26		SR2-T1	0.27	100	365	400	300	Φ20	530	628	Φ8	530	100.5	Φ8	530	100.5
27		SR2-T2	0.27	100	365	400	300	Φ20	530	628	Φ8	530	100.5	Φ8	530	100.5
28		SR3-T1	0.27	100	365	400	300	Φ20	530	628	Φ8	530	100.5	Φ8	530	100.5
29		SR3-T2	0.27	100	365	400	300	Φ20	530	628	Φ8	530	100.5	Φ8	530	100.5
30		SR4-T1	0.27	100	369	400	300	Φ12	530	339	Φ8	530	100.5	Φ8	530	100.5
31		SR4-T2	0.27	100	369	400	300	Φ12	530	339	Φ8	530	100.5	Φ8	530	100.5
32		SR5-T1	0.27	100	365	400	300	Φ20	530	628	Φ8	530	100.5	Φ8	530	100.5
33		SR5-T2	0.27	100	365	400	300	Φ20	530	628	Φ8	530	100.5	Φ8	530	100.5
34	[24]	C40/50-A	0.6	100	167	200	200	Φ16	530	402	Φ8	530	100.5	Φ8	530	100.5
35		C40/50-B	0.6	100	167	200	200	Φ16	530	402	-	-	-	-	-	-
36		SFRC-B	0.6	100	167	200	200	Φ16	530	402	-	-	-	-	-	-
37		SFRC-D	0.6	100	167	200	200	Φ16	530	402	-	-	-	-	-	-
38	[26]	A1	0.85	100	117	150	200	Φ16	500	402	Φ8	500	100.5	Φ8	500	100.5
39		A2	0.85	100	117	150	200	Φ16	500	402	Φ8	500	100.5	Φ8	500	100.5
40		B1	0.85	100	117	150	200	Φ16	500	402	-	-	-	-	-	-
41		B2	0.85	100	117	150	200	Φ16	500	402	-	-	-	-	-	-
42		C1	0.85	100	117	150	200	Φ16	500	402	-	-	-	-	-	-
43		C2	0.85	100	117	150	200	Φ16	500	402	-	-	-	-	-	-
44		D1	0.83	100	120	150	200	Φ10	500	157	-	-	-	-	-	-
45		D2	0.83	100	120	150	200	Φ10	500	157	-	-	-	-	-	-

Table 7.3: Database (1)

Table 7.4: Database (2)

No.	Ref.	Beam name	Layer 1			Layer 2			Layer 3			Layer 4			Layer 5		
			diameter	fyv (MPa)	Asv (mm^2)	diameter	fyv (MPa)	Asv (mm^2)	diameter	fyv (MPa)	Asv (mm^2)	diameter	fyv (MPa)	Asv (mm^2)	diameter	fyv (MPa)	Asv (mm^2)
1	[1]	B1	Φ6.35	456	63.3	Φ6.35	456	63.3	Φ6.35	456	63.3	-	-	-	-	-	-
2		B7	Φ6.35	456	63.3	Φ6.35	456	63.3	Φ6.35	456	63.3	-	-	-	-	-	-
3		B14	Φ6.35	456	63.3	Φ6.35	456	63.3	Φ6.35	456	63.3	-	-	-	-	-	-
4		B2	Φ6.35	456	63.3	Φ6.35	456	63.3	Φ6.35	456	63.3	-	-	-	-	-	-
5		B9	Φ6.35	456	63.3	Φ6.35	456	63.3	Φ6.35	456	63.3	-	-	-	-	-	-
6		B16	Φ6.35	456	63.3	Φ6.35	456	63.3	Φ6.35	456	63.3	-	-	-	-	-	-
7		B5	Φ6.35	456	63.3	Φ6.35	456	63.3	Φ6.35	456	63.3	-	-	-	-	-	-
8		B11	Φ6.35	456	63.3	Φ6.35	456	63.3	Φ6.35	456	63.3	-	-	-	-	-	-
9		B15	Φ6.35	456	63.3	Φ6.35	456	63.3	Φ6.35	456	63.3	-	-	-	-	-	-
10		B6	Φ6.35	456	63.3	Φ6.35	456	63.3	Φ6.35	456	63.3	-	-	-	-	-	-
11		B13	Φ6.35	456	63.3	Φ6.35	456	63.3	Φ6.35	456	63.3	-	-	-	-	-	-
12		B18	Φ6.35	456	63.3	Φ6.35	456	63.3	Φ6.35	456	63.3	-	-	-	-	-	-
13		B3	Φ6.35	456	63.3	Φ6.35	456	63.3	Φ6.35	456	63.3	-	-	-	-	-	-
14		B10	Φ6.35	456	63.3	Φ6.35	456	63.3	Φ6.35	456	63.3	-	-	-	-	-	-
15		B17	Φ6.35	456	63.3	Φ6.35	456	63.3	Φ6.35	456	63.3	-	-	-	-	-	-
16	[15]	DEB-1.6-T1	Φ10	542	157	Φ12	552	226	Φ10	542	157	Φ10	542	314	-	-	-
17		DEB-1.6-T2	Φ10	542	157	Φ12	552	226	Φ10	542	157	Φ10	542	314	-	-	-
18		DEB-3.7-T1	Φ10	542	157	Φ12	552	226	Φ10	542	157	Φ10	542	314	-	-	-
19		DEB-3.7-T2	Φ10	542	157	Φ12	552	226	Φ10	542	157	Φ10	542	314	-	-	-
20		DEB-3.8-T1	Φ10	542	157	Φ12	552	226	Φ10	542	157	Φ10	542	314	-	-	-
21		DEB-3.8-T2	Φ10	542	157	Φ12	552	226	Φ10	542	157	Φ10	542	314	-	-	-
22		DEB-3.9-T1	Φ10	542	157	Φ12	552	226	Φ10	542	157	Φ10	542	314	-	-	-
23		DEB-3.9-T2	Φ10	542	157	Φ12	552	226	Φ10	542	157	-	-	-	-	-	-
24	[13]	SR1-T1	Φ12	530	226	Φ12	530	226	Φ12	530	226	Φ12	530	226	Φ12	530	226
25		SR1-T2	Φ12	530	226	Φ12	530	226	Φ12	530	226	Φ12	530	226	Φ12	530	226
26		SR2-T1	Φ12	530	226	Φ12	530	226	Φ12	530	226	Φ12	530	226	Φ12	530	226
27		SR2-T2	Φ12	530	226	Φ12	530	226	Φ12	530	226	Φ12	530	226	Φ12	530	226
28		SR3-T1	Φ12	530	226	Φ12	530	226	Φ12	530	226	-	-	-	-	-	-
29		SR3-T2	Φ12	530	226	Φ12	530	226	Φ12	530	226	Φ12	530	226	-	-	-
30		SR4-T1	Φ12	530	226	Φ12	530	226	Φ12	530	226	Φ12	530	226	Φ12	530	226
31		SR4-T2	Φ12	530	226	Φ12	530	226	Φ12	530	226	Φ12	530	226	Φ12	530	226
32		SR5-T1	Φ12	530	226	Φ12	530	226	Φ12	530	226	Φ12	530	226	Φ12	530	226
33		SR5-T2	Φ12	530	226	Φ12	530	226	Φ12	530	226	Φ12	530	226	Φ12	530	226
34	[24]	C40/50-A	Φ8	530	100.5	Φ8	530	100.5	Φ8	530	100.5	Φ8	530	100.5	-	-	-
35		C40/50-B	Φ8	530	100.5	Φ8	530	100.5	-	-	-	-	-	-	-	-	-
36		SFRC-B	Φ8	530	100.5	Φ8	530	100.5	-	-	-	-	-	-	-	-	-
37		SFRC-D	Φ12	530	226	Φ12	530	226	-	-	-	-	-	-	-	-	-
38	[26]	A1	Φ6	500	56.6	Φ6	500	56.6	Φ6	500	56.6	Φ6	500	56.6	-	-	-
39		A2	Φ6	500	56.6	Φ6	500	56.6	Φ6	500	56.6	Φ6	500	56.6	-	-	-
40		B1	Φ6	500	56.6	Φ6	500	56.6	Φ6	500	56.6	-	-	-	-	-	-
41		B2	Φ6	500	56.6	Φ6	500	56.6	Φ6	500	56.6	-	-	-	-	-	-
42		C1	Φ6	500	56.6	Φ6	500	56.6	-	-	-	-	-	-	-	-	-
43		C2	Φ6	500	56.6	Φ6	500	56.6	-	-	-	-	-	-	-	-	-
44		D1	Φ6	500	56.6	Φ6	500	56.6	-	-	-	-	-	-	-	-	-
45		D2	Φ6	500	56.6	Φ6	500	56.6	-	-	-	-	-	-	-	-	-

Table 7.5: Database (3)

| No. | Ref. | Beam name | Diagonal reinforcement | | | | f'c | theta (deg) | H (kN) | ρ_f (%) | L/D | L (mm) | D (mm) | Type of fiber | f_f (MPa) |
			diameter	fyd (MPa)	Asd (mm^2)	beta (°)									
1	[1]	B1	-	-	-	-	29	45	-	0	-	-	-	-	-
2		B7	-	-	-	-	30.5	45	-	0.8	100	50.8	0.508	hooked-end	1160
3		B14	-	-	-	-	31.3	45	-	1.2	100	50.8	0.508	hooked-end	1160
4		B2	-	-	-	-	29	45	-	0	-	-	-	-	-
5		B9	-	-	-	-	30.5	45	-	0.8	100	50.8	0.508	hooked-end	1160
6		B16	-	-	-	-	31.3	45	-	1.2	100	50.8	0.508	hooked-end	1160
7		B5	-	-	-	-	29	45	-	0	-	-	-	-	-
8		B11	-	-	-	-	30.5	45	-	0.8	100	50.8	0.508	hooked-end	1160
9		B15	-	-	-	-	31.3	45	-	1.2	100	50.8	0.508	hooked-end	1160
10		B6	-	-	-	-	29	45	-	0	-	-	-	-	-
11		B13	-	-	-	-	30.5	45	-	0.8	100	50.8	0.508	hooked-end	1160
12		B18	-	-	-	-	31.3	45	-	1.2	100	50.8	0.508	hooked-end	1160
13		B3	-	-	-	-	29	45	-	0	-	-	-	-	-
14		B10	-	-	-	-	30.5	45	-	0.8	100	50.8	0.508	hooked-end	1160
15		B17	-	-	-	-	31.3	45	-	1.2	100	50.8	0.508	hooked-end	1160
16	[15]	DEB-1.6-T1	-	-	-	-	31.1	58	-	0	-	-	-	-	-
17		DEB-1.6-T2	-	-	-	-	31.1	38	-	0	-	-	-	-	-
18		DEB-3.7-T1	-	-	-	-	45.5	40	-	0.5	65	35	0.55	hooked-end	1100
19		DEB-3.7-T2	-	-	-	-	45.5	39	-	0.5	65	35	0.55	hooked-end	1100
20		DEB-3.8-T1	-	-	-	-	48.8	34	-	0.87	65	35	0.55	hooked-end	1100
21		DEB-3.8-T2	-	-	-	-	48.8	41	-	0.87	65	35	0.55	hooked-end	1100
22		DEB-3.9-T1	-	-	-	-	48.4	39	-	1.24	65	35	0.55	hooked-end	1100
23		DEB-3.9-T2	-	-	-	-	48.4	31	-	1.24	65	35	0.55	hooked-end	1100
24	[13]	SR1-T1	-	-	-	-	45	54.7	-	0	-	-	-	-	-
25		SR1-T2	-	-	-	-	45	54.7	-	0	-	-	-	-	-
26		SR2-T1	-	-	-	-	46.5	59.3	-	1	65	35	0.55	hooked-end	1345
27		SR2-T2	-	-	-	-	46.5	58.2	-	1	65	35	0.55	hooked-end	1345
28		SR3-T1	-	-	-	-	47.5	58.1	-	1	65	35	0.55	hooked-end	1345
29		SR3-T2	-	-	-	-	47.5	58.1	-	1	65	35	0.55	hooked-end	1345
30		SR4-T1	-	-	-	-	42	53.1	-	1	65	35	0.55	hooked-end	1345
31		SR4-T2	-	-	-	-	42	53.1	-	1	65	35	0.55	hooked-end	1345
32		SR5-T1	-	-	-	-	49	56.5	-	1	65	35	0.55	hooked-end	1345
33		SR5-T2	-	-	-	-	49	56.5	-	1	65	35	0.55	hooked-end	1345
34	[24]	C40/50-A	Φ10	530	157	33.1	43.2	45	-	0	-	-	-	-	-
35		C40/50-B	-	-	-	-	43.2	45	-	0	-	-	-	-	-
36		SFRC-B	-	-	-	-	63.6	45	-	1	65	60	0.9	hooked-end	1345
37		SFRC-D	-	-	-	-	62.4	45	-	1	65	60	0.9	hooked-end	1345
38	[26]	A1	-	-	-	-	40.5	45	-	0	-	-	-	-	-
39		A2	-	-	-	-	40.5	37	-	0	-	-	-	-	-
40		B1	-	-	-	-	40.5	32	-	0	-	-	-	-	-
41		B2	-	-	-	-	40.5	31	-	0	-	-	-	-	-
42		C1	-	-	-	-	52.3	62	-	1	65	60	0.9	hooked-end	1345
43		C2	-	-	-	-	52.3	48	-	1	65	60	0.9	hooked-end	1345
44		D1	-	-	-	-	52.3	34	-	1	65	60	0.9	hooked-end	1345
45		D2	-	-	-	-	52.3	30	-	1	65	60	0.9	hooked-end	1345

Table 7.6: Database (4)

No.	Ref.	Beam name	Flexural failure	Vexp (kN)	θ = θexp Simplified approach Vpred (kN)	Vexp/Vp	θ = θexp Complete behavior Vpred (kN)	Vexp/Vp	θ = 45° Simplified approach Vpred (kN)	Vexp/Vp	θ = 45° Complete behavior Vpred (kN)	Vexp/Vp
1	[1]	B1	no	44	(40.2)	(1.1)	(45.8)	(0.96)	(40.2)	(1.1)	(45.8)	(0.96)
2		B7	DK	61.8	(54.9)	(1.13)	(66.0)	(0.94)	(54.9)	(1.13)	(66.0)	(0.94)
3		B14	yes	69	59.6	1.16	71	0.97	59.6	1.16	71	0.97
4		B2	no	48	(37.8)	(1.27)	(42.4)	(1.13)	(37.8)	(1.27)	(42.4)	(1.13)
5		B9	DK	52.5	(51.6)	(1.02)	(60.9)	(0.86)	(51.6)	(1.02)	(60.9)	(0.86)
6		B16	yes	56.5	56.6	1.00	66	0.86	56.6	1.00	66	0.86
7		B5	DK	32.9	(26.4)	(1.25)	(27.2)	(1.21)	(26.4)	(1.25)	(27.2)	(1.21)
8		B11	yes	43.6	37.2	1.17	44.9	0.97	37.2	1.17	44.9	0.97
9		B15	yes	54.3	40.4	1.34	48.2	1.13	40.4	1.34	48.2	1.13
10		B6	no	28	(25.7)	(1.09)	(27.1)	(1.03)	(25.7)	(1.09)	(27.1)	(1.03)
11		B13	yes	40	35.5	1.13	43.4	0.92	35.5	1.13	43.4	0.92
12		B18	yes	43.6	38.8	1.13	46.7	0.93	38.8	1.13	46.7	0.93
13		B3	no	48.9	(40.2)	(1.22)	(45.8)	(1.07)	(40.2)	(1.22)	(45.8)	(1.07)
14		B10	yes	56.9	54.9	1.04	66.0	0.86	54.9	1.04	66.0	0.86
15		B17	no	61.4	(59.6)	(1.02)	(71.0)	(0.86)	(59.6)	(1.02)	(71.0)	(0.86)
16	[15]	DEB-1.6-T1	yes	309	239	1.29	271	1.14	253	1.22	282	1.10
17		DEB-1.6-T2	yes	251	269	0.93	291	0.86	253	0.99	282	0.89
18		DEB-3.7-T1	yes	333	343	0.97	362	0.92	332	1.00	361	0.92
19		DEB-3.7-T2	yes	328	346	0.95	364	0.90	332	0.99	361	0.91
20		DEB-3.8-T1	yes	363	397	0.91	406	0.90	357	1.02	380	0.96
21		DEB-3.8-T2	yes	362	367	0.98	381	0.95	357	1.01	380	0.95
22		DEB-3.9-T1	yes	354	394	0.9	403	0.88	376	0.94	398	0.89
23		DEB-3.9-T2	yes	370	442	0.84	442	0.84	376	0.98	398	0.93
24	[13]	SR1-T1	yes (assumption)	459	516	0.89	538	0.85	536	0.86	547	0.84
25		SR1-T2	yes (assumption)	434	516	0.84	538	0.81	536	0.81	547	0.80
26		SR2-T1	yes (assumption)	670	691	0.97	692	0.97	697	0.96	684	0.98
27		SR2-T2	yes (assumption)	681	687	0.99	689	0.99	697	0.98	684	1.00
28		SR3-T1	yes (assumption)	574	669	0.86	666	0.86	606	0.95	590	0.97
29		SR3-T2	yes (assumption)	534	669	0.8	666	0.80	606	0.88	590	0.91
30		SR4-T1	yes (assumption)	600	546	1.1	537	1.12	589	1.02	571	1.05
31		SR4-T2	yes (assumption)	622	546	1.14	537	1.16	589	1.06	571	1.09
32		SR5-T1	yes (assumption)	649	691	0.94	691	0.94	705	0.92	690	0.94
33		SR5-T2	yes (assumption)	599	691	0.88	691	0.87	705	0.85	690	0.87
34	[24]	C40/50-A	yes (assumption)	262	190	1.38	195.6	1.34	190	1.38	196	1.34
35		C40/50-B	yes (assumption)	145	108	1.34	123.4	1.17	108	1.34	123	1.17
36		SFRC-B	yes (assumption)	223	169.5	1.32	198	1.13	169.5	1.32	198	1.13
37		SFRC-D	yes (assumption)	260	193.4	1.35	230	1.13	193.4	1.35	230	1.13
38	[26]	A1	no	117	-	-	-	-	-	-	-	-
39		A2	no	127	-	-	-	-	-	-	-	-
40		B1	DK	86.3	-	-	-	-	-	-	-	-
41		B2	DK	92.7	-	-	-	-	-	-	-	-
42		C1	yes	111.7	114.98	0.97	152.3	0.73	104.1	1.07	129.5	0.86
43		C2	yes	104.3	105.54	0.99	132.9	0.78	104.1	1.00	129.5	0.81
44		D1	yes	105.5	81.95	1.29	86.3	1.22	77.6	1.36	84.3	1.25
45		D2	yes	97.6	85.67	1.14	88.7	1.10	77.6	1.26	84.3	1.16
					Avg. CoV	14.91 % 1.05	Avg. CoV	13.25% 0.96	Avg. CoV	13.61% 1.07	Avg. CoV	11.13% 0.97

NB: Avg. & CoV only applied to FRC specimens with flexural failure mode

Notation of the database: a/d = span-to-depth ratio; a = distance from the support reaction to the face of the full-depth section; d = effective depth of the dapped-end; h = total depth of the dapped-end; b = width of the section; diameter = diameter of the layer considered; fyh = yield strength of the considered layer of dapped-end horizontal reinforcement; Ash = total area of dapped-end horizontal reinforcement; fyv = yield strength of the considered layer of dapped-end vertical reinforcement; Asv = total area of dapped-end vertical reinforcement; fyd = yield strength of the considered layer of dapped-end diagonal reinforcement; Asd = total area of dapped-end diagonal reinforcement; β = angle of inclination of the diagonal reinforcement with the horizontal axis; f'_c = concrete cylinder strength; θ = measured angle of inclination of the crack at the re-entrant corner (extracted from existing structures); H = external force applied to the support reaction; ρ_f = fiber volume ratio; l/d = fiber aspect ratio; l = fiber length; d = fiber diameter; f_f = fiber tensile strength; DK = do not know; V_{exp} = experimental strength of the dapped-end; V_{pred} = predicted strength of the dapped-end; Avg = average experimental-to-predicted ratio; CoV = coefficient of variation.

References

[1] Ajina. "Effect of Steel Fibers on Precast Dapped-end Beam Connections". MA thesis. South Dakota State University, 1986.

[2] Di Prisco et al. "The technical causes of the collapse of Annone overpass on SS". In: *Italian Concrete Days 2018, Lecco, Italy* 36 (2018), pp. 1–16.

[3] Moccia et al. "Concrete compressive strength: From material characterization to a structural value". In: *Structural Concrete* (2020).

[4] Wy et al. "Behaviour of reinforced concrete dapped-end beams". In: *Mag. Concr. Res* 9.64 (2012), pp. 793–805.

[5] Wy et al. "Shear strength of high-strength concrete dapped-end beams". In: *J. Chin. Inst. Eng, Transactions of the Chinese Institute of Engineers* 5.26 (2003), pp. 671–680.

[6] Beakart. *Product Datasheet: Dramix 3D-100/60-BG*.

[7] Beakart. *Product Datasheet: Dramix 3D-45/50-BL*.

[8] Beakart. *Product Datasheet: Dramix 3D-55/60-BL*.

[9] Beakart. *Product Datasheet: Dramix 3D-65/60-BG*.

[10] Beakart. *Product Datasheet: Dramix 3D-80/60-BG*.

[11] Collins. "Towards a rational theory for RC members in shear". In: *J. Struct. Division.* 4.104 (1978).

[12] Dere. "Assessing a retrofitting method for existing RC buildings with low seismic capacity in Turkey". In: *The name of the journal* 31.2 (Apr. 2017), pp. 201–213. DOI: `https://doi.org/10.1061/(ASCE)CF.1943-5509.0000969`.

[13] Elliott and Mohamed. "Shear strength of short recess precast dapped-end Beams made of steem fibre self-compacting concrete". In: Our world in concrete structures. Singapore: CI-Premier PTE LTD, Aug. 2008.

[14] Ezeldin and Balaguru. "Normal-and High-Strength Fiber-Reinforced Concrete under Compression". In: *Journal of Materials in Civil Engineering* 4.2 (Nov. 1992). DOI: `https://doi.org/10.1061/(ASCE)0899-1561(1992)4:4(415`.

[15] Mata Falcón. "Estudio del comportamiento en servicio y rotura de los apoyos a media madera (Spanish) [Serviceability and Ultimate Behaviour of Dapped-end Beams]". PhD thesis. Universitat Politècnica De València, June 2015.

[16] FIB. "Bond of reinforcement in concrete". In: *Bulletin d'Information de la Federation Internationale du Beton* 10 (2000), pp. 3–7.

[17] Herzinger and Elbadry. "Alternative reinforcing details in dapped ends of precast concrete bridge girders: experimental investigation". In: *Transportation Research Record: Journal of the Transportation Research Board* 2028.1 (Dec. 2007), pp. 111–121.

[18] Johnson, Couture, and Nicolet. "Commission of inquiry into the collapse of a portion of the de la Concorde overpass". In: *Library and National Archives of Quebec* (Dec. 2007).

[19] Kanellopoulos. "Zum unelastischen Verhalten und Bruch von Stahlbeton". PhD thesis. Institut für Baustatik und Konstruktion, ETH, Zürich, 1986, p. 33.

[20] Lee, Cho, and Vecchio. "Simplified diverse embedment model for steel fibre-reinforced concrete elements in tension". In: *ACI Materials Journal* 4.110 (2013), pp. 403–412.

[21] Lee, Oh, and Cho. "Compressive behaviour of fibre-reinforced concrete with end-hooked steel fibres". In: *Mater* 8.4 (2015), pp. 1442–1458.

[22] Löfgren. "Fibre-reinforced Concrete for Industrial Construction – a fracture mechanics approach to material testing and structural analysis". PhD thesis. Chalmers University of Technology, Göteborg, Sweden, 2005.

[23] Mihaylov, Liu, and Tvrznikova. "Two-parameter kinematic approach for complete shear behavior of deep FRC beams". In: *International Federation for Structural Concrete* 1.1 (2020), pp. 362–375. DOI: https://doi.org/10.1002/suco.201800199.

[24] Håvard Nedrelid. *Structural FRC – Design approach and experimental results*. Vol. 66. SINTEF Building and Infrastructure, 2015. ISBN: 978-82-536-1466-3.

[25] Nielsen and Hoang. *Limit Analysis and Concrete Plasticity*. 3. Taylor Francis Group, 2011. ISBN: 978-1-4398-0396-7.

[26] Nordbrøden and Weydahl. "Testing of Fibre Reinforced Concrete Structures". MA thesis. Department of Structural Engineering: Norwegian University of Science and Technology, June 2012.

[27] Özkılı, Aksoylu, and Arslan. "Experimental and numerical investigations of steel fiber reinforced concrete dapped-end purlins". In: *Journal of Building Engineering* 36 (Apr. 2021). DOI: https://doi.org/10.1016/j.jobe.2020.102119.

[28] Popovics. "A numerical approach to the complete stress-strain curve of concrete". In: *Cem. Concr. Res* 5.3 (1973), pp. 583–599.

[29] Rajapakse, Degée, and Mihaylov. "Assessment of Failure along Re-Entrant Corner Cracks in Existing RC Dapped-End Connections". In: *Structural Engineering International* 31.2 (2021), pp. 216–226. DOI: https://doi.org/10.1080/10168664.2021.1878975.

[30] Schlaich and Schafer. "Design and detailing of structural concrete using strut-and-tie models". In: *Struct. Eng* 6.69 (1991), pp. 113–125.

[31] Schlaich, Schäfer, and Jennewein. "Toward a consistent design of structural concrete". In: *PCI J* 3.32 (1987), pp. 74–150.

[32] Sigrist. "Zum Verformungsvermögen von Stahlbetonträgern [On the Deformation Capacity of Structural Concrete Girders]". In: (1995), pp. 11–121.

[33] Su, Chandler, and Wong PC. "Design of non-flexural components using strut and tie models". In: *HKIE Trans* 1.10 (2003), pp. 31–37.

[34] Thomas and Ramaswamy. "Mechanical Properties of Steel Fiber-Reinforced Concrete". In: *Journal of Materials in Civil Engineering* 19.5 (May 2007). DOI: 10.1061/(ASCE)899-1561(2007)19:5(385).

[35] Weiss, Guler, and Shah. "Localization and size-dependent response of reinforced concrete beams". In: *Struct. J* 5.98 (2001), pp. 686–695.

[36] Zhou, Wu, and Feng. "Analytical model for rotation response of singly reinforced flexural members". In: *ACI Struct. J* 3.115 (2018), pp. 711–789.